Missouri S&T Library and Learning Resources

Scholars' Mine

Doctoral Dissertations | Student Theses and Dissertations

Fall 2017

Pillar design for St. Peter sandstone formation

Francis Anohomah Arthur

Follow this and additional works at: https://scholarsmine.mst.edu/doctoral_dissertations

 Part of the Mining Engineering Commons

Department: Mining and Nuclear Engineering

Recommended Citation

Arthur, Francis Anohomah, "Pillar design for St. Peter sandstone formation" (2017). *Doctoral Dissertations*. 2618.
https://scholarsmine.mst.edu/doctoral_dissertations/2618

This thesis is brought to you by Scholars' Mine, a service of the Missouri S&T Library and Learning Resources. This work is protected by U. S. Copyright Law. Unauthorized use including reproduction for redistribution requires the permission of the copyright holder. For more information, please contact scholarsmine@mst.edu.

PILLAR DESIGN METHOD FOR ST. PETER SANDSTONE FORMATION

by

FRANCIS ANOHOMAH ARTHUR

A DISSERTATION

Presented to the Faculty of the Graduate School of the

MISSOURI UNIVERSITY OF SCIENCE AND TECHNOLOGY

In Partial Fulfillment of the Requirements for the Degree

DOCTOR OF PHILOSOPHY

in

MINING ENGINEERING

2017

Approved by:
Kwame Awuah-Offei, Advisor
Andreas Eckert, Co-Advisor
Samuel Frimpong
Grzegorz Galecki
Nassib Aouad

© 2017
Francis Anohomah Arthur
All Rights Reserved

ABSTRACT

Silica sands produced primarily from St. Peter Sandstone are used for hydraulic fracturing in the petroleum industry, glassmaking, chemicals, ceramics, filtration and the foundry industry in the US. The recent high demand for silica sands for hydraulic fracturing has triggered increased production and commissioning of new silica sand mines to support natural gas production from shale and tight gas deposits in the US. Most mines use surface mining methods to extract St. Peter Sandstone. The room and pillar mining method has been successfully used for St. Peter Sandstone mining in a few US locations, however, no one has proposed a rigorous pillar design method. The goal of this research is to: (1) elucidate factors contributing to ground control problems in St. Peter Sandstone mines; (2) derive a pillar design method for St. Peter Sandstone using numerical modeling; and (3) investigate the mechanics of "pinch out" failure in St. Peter Sandstone. The study found that the factors contributing to ground control problems in St. Peter Sandstone mines are: water in roofs, friability of the St. Peter Sandstone, strength variability, and reinforcement techniques. The study proposed the following pillar strength criteria for St Peter Sandstone:

$$S_P = 14.360 + 11.720C - 0.903h\left[0.28 + 0.53(w/h)\right] \quad (67)$$

Where, C is the cohesion of the pillar rock in MPa, h is the pillar height in meters and w/h is the dimensionless pillar width to height ratio.

The study also found that pinch out failure is influenced by the contrast in rock properties at the pillar-roof interface and shape of the mine opening.

ACKNOWLEDGMENTS

I am thankful to Jehovah for life, good health, and wisdom throughout this journey. I would like to express my sincere gratitude to my advisors, Dr. Kwame Awuah-Offei and Dr. Andreas Eckert, for his enlightening guidance, inspiring instructions, supports, critiques, advice, and improving my writing abilities. Your guidance and inputs in writing this dissertation are highly appreciated. I thank you for giving me the opportunity to work with you when Dr. Maochen Ge retired. I also thank Dr. Maochen Ge for the opportunities to conduct practical research in rock mechanics and ground control, teaching and funding this study.

I am appreciative of the valuable comments and suggestions from my committee members, Dr. Samuel Frimpong, Dr. Grzegorz Galecki, and Dr. Nassib Aouad.

I am highly indebted to Dr. Raymond Suglo and his family for their unconditional love, kindness, financial supports, encouragements, and recommendations throughout the years. I also appreciate the encouragements from my colleagues particularly, Dr. Amirhosein Bagherieh, Dr. Eric Gbadam, and others. I am thankful for the prayer supports from Mr. Mckeowe Amoako.

I am grateful to Zhao Chen of Itasca Consulting Group Incorporated, for his support in my numerical model development. I am thankful for an additional FLAC3D software through the Itasca Education Partnership (IEP) program.

I am indebted to my loving wife, Albertina Arthur, for her patience, unconditional love, supports, prayers, and encouragement throughout this journey. To our child, Roselyn Arthur, I say your understanding and cooperation were very motivating. To my parents and brothers, I say thank you for the prayers and encouragement. Thank you all for the sacrifices you made for us to complete this milestone successfully. God bless you all.

TABLE OF CONTENTS

LIST OF ILLUSTRATIONS

Page

LIST OF TABLES

Page

1. INTRODUCTION

This Section presents the background information of this research, research objectives, research methodology, scientific and industrial contributions of the research and organizational structure of this research.

1.1. BACKGROUND OF THE RESEARCH PROBLEM

The United States (US) is a major producer and consumer of silica sand in the World. In the US, silica sands are used for hydraulic fracturing in the petroleum industry, glassmaking, chemicals, ceramics, filtration and the foundry industry. While the consumption of silica sands for glassmaking have remained fairly constant, in recent years, the demand for silica sand for hydraulic fracturing has increased significantly (Figure 1.1). For example, in 2014, silica sand produced for hydraulic fracturing was about 24 times that consumed in 2004. Although the consumption of hydraulic fracturing sand has declined from 2014 to 2016, it remains at historically high levels in US (USGS, 2016). This is due to high production of natural gas from unconventional reservoirs that require hydraulic fracturing to stimulate production. In 2015, for example, 67% of US natural gas was produced using hydraulic fracturing combined with horizontal drilling technologies especially in shale and tight gas (US Energy Information Administration, 2016), and the trend is expected to increase (Figure 1.2). Thus, the demand for silica sands for hydraulic fracturing will continue to require increased production capacities and new silica sand mines will be commissioned to support the production of natural gas from shale and tight gas deposits in the US.

Silica sand is primarily produced from St. Peter Sandstone in North America. The St. Peter Sandstone formation covers about 576,000 km^2 in North America (Dittes and Labuz, 2002). The surge of silica sand demand has led to increased production from US mines exploiting the St. Peter Sandstone formation. In most cases, mines use surface mining methods (mainly open pit and dredging) in situations where the cost of removing the overburden material is not prohibitive. However, surface mining techniques can become less sustainable due to environmental concerns in some mining communities (e.g. Winona County, MN banned silica mining due to environmental concerns).

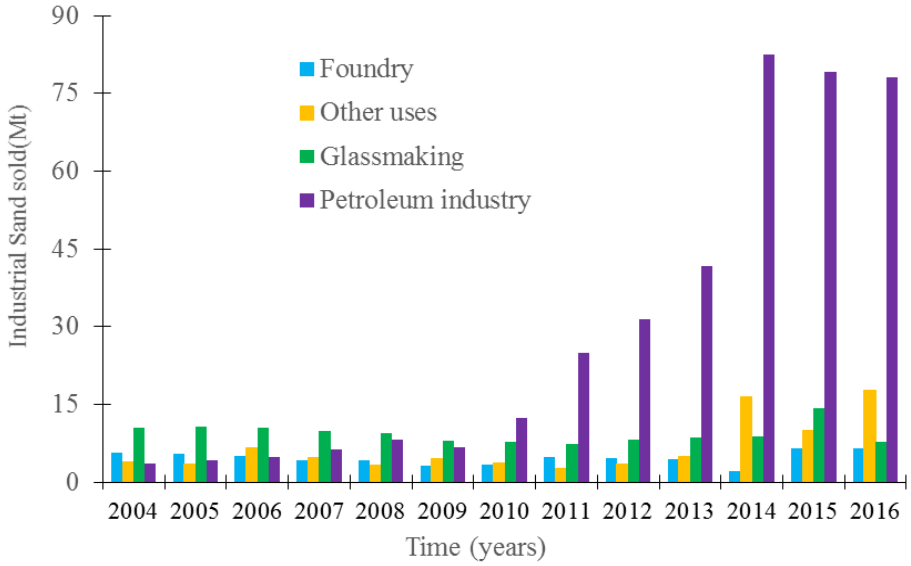

Figure 1.1. Industrial sand consumed by various industries over time

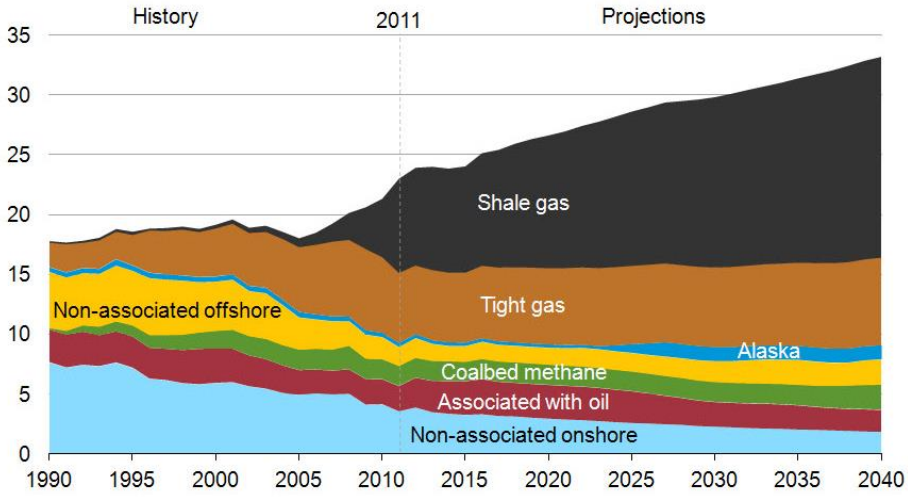

Figure 1.2. US natural gas production (EIA, 2016)

The room and pillar underground mining method has been used where the cost of removing the overburden materials is too expensive.

In a room and pillar mining environment, pillars are left in-situ to provide support of the overburden strata. The room and pillar underground mining method has been used to exploit St. Peter Sandstone formation in Clayton, Iowa, Crystal City, Missouri, Guion, Arkansas, Pacific, Missouri, and St. Paul-Minneapolis, Minnesota. Even though the room

and pillar mining method has been successfully used in these locations, no rigorous pillar design method has been proposed for St. Peter Sandstone. Available pillar design methods have proven to be inadequate owing to lack of adequate room and pillar case histories (for empirical design criteria) and rock strength variability, and unique strength properties (Petersen, 1978; Bagherieh, 2015). Pillar design involves selecting an appropriate pillar size that satisfies safety and economic constraints by estimating the stress imposed on and the maximum load-bearing capacity of the pillar. The design of pillars is crucial to provide support of the overlying strata and provide safe working conditions in room and pillar mines. This research initiative is aimed at developing a rigorous pillar design method for St. Peter Sandstone room and pillar mines.

Pillar design involves selecting an appropriate pillar size that satisfy safety and economic constraints by estimating the stress imposed on and the maximum load-bearing capacity of the pillar. The design of pillars is crucial to provide support of the overlying strata and provide safe working conditions in room and pillar mines. This research initiative is aimed at developing a rigorous pillar design method for St. Peter Sandstone room and pillar mines.

1.2. STATEMENT OF THE PROBLEM

The St. Peter Sandstone is a unique formation different from other geomaterials that have been studied extensively in rock mechanics. It has almost zero cohesion and high friction angle of about 57^{o}-70^{o}, which is almost 15-20˚ higher than the highest friction angle ever reported for the geotechnical materials as reported by (Watson, 1938; Means and Parcher, 1963; Dusseault and Morgenstern, 1979; Labuz et al., 1998; Dittes and Labuz, 2002; Bagherieh, 2015). It has been described as a soft rock that could be cut with a knife according to Captain Carver in 1766-1768. Also, in 1891, Sardeson described it as a whitish-yellowish material that could be called a sand rather than sandstone. With average uniaxial compressive strength of about 4.5 MPa, it can be classified as a weak rock (IAEG, 1979, British Geological Society, 1970), very weak rock (Coates, 1964, ISRM, 1979), low strength rock (Broch and Franklin, 1972) or very low strength rock (Deere and Miller, 1966, Bieniawski, 1973). The candidate could not

find any work in the literature that addresses pillar design methods for geological material with extremely weak to very weak rock strength.

Designing pillars require one to estimate pillar strength -and stress and determine an appropriate pillar size that satisfies economic and safety constraints (Esterhuizen, 2007). Pillar stress can be estimated using the tributary area method, assuming the overburden weight is equally distributed (Brady and Brown, 1985). The limitations of the tributary area method are that, it ignores, pillar stress distribution, deformation and failure characteristics of the roof-pillar strata, and the interaction between the roof and pillar strata (Jeremic, 1985). For this reason, the tributary area method predicts the upper limit of the average pillar stress (Esterhuizen et. al., 2011). Mark (1987) used finite element modeling to demonstrate that, changes in rock properties, horizontal stresses, and unequal sized pillars have little effect on pillar stress. Thus for practical design purposes, the tributary area method can be used to estimate the pillar stress. Pillar strength, on the other hand, can be estimated using empirical, analytical and numerical methods.

Empirical pillar strength methods can be developed by extrapolating the results of laboratory tests on rock specimens to full-sized pillars used in mines. This approach has been used to derive empirical pillar strength equations for coal (Holland and Gaddy, 1957; Obert and Duval, 1967). Empirical pillar strength formulas can also be derived using the back-calculation technique. In this approach, observed failed and stable pillar cases are collected and a pillar strength curve is fitted to the data. This approach has been used to investigate the stability of coal (Salamon and Munro, 1967; Mark, 1999) and hard rock pillars (Hedley and Grant, 1972; Pritchard and Hedley, 1993; Mark, 1999). Another empirical approach is to establish pillar strength equations from large-scale in-situ pillar strength test. Although this approach is expensive and cumbersome, it has been used to derive empirical pillar strength equation for coal (Bieniawski, 1968; Bieniawski, 1970; Wagner, 1974; Van Heerdan, 1975; Sheorey, 2000, and Malecki, 1992).

The previous attempt to estimate pillar strength for St. Peter Sandstone pillars using the empirical method was very limited, due to the limited room and pillar underground developments were in the area. Even the excavations that existed were generally developed in a haphazard unplanned manner (Peterson, 1978). As a result, there was no local experience from which the most elementary design technique could be built

(Petersen, 1978). Presently, there are numerous room and pillar case histories available, however, empirical pillar strength based on the back-calculation approach has proved inadequate as no one has reported pillar failure in St. Peter Sandstone mines. Notwithstanding that, the most challenging issue for the application of empirical design for St. Peter Sandstone is, it is difficult to scale-up laboratory and in-situ strength values due to material variability, effects during sampling, specimen preparation and testing, size and shape effect (Payne, 1967; Yardley, (1977), Petersen, 1978; Sterling (1978) Baghereih, 2015; Dittes, 2015). All these issues may be related to inhomogeneity of the St. Peter Sandstone structure (Baghereih, 2015).

Analytical methods (such as Wilson theory (Wilson,1972)) for predicting pillar strength show promise, but their assumptions about pillar behavior and the mechanism of pillar failure have not been confirmed by extensive field measurements (Mark, 1987). Hence while such methods have furthered our understanding of pillar failure mechanics (Esterhuizen, 2007), they fall short when it comes to elucidating the effect of friction angle and cohesion, during pillar loading condition, on: (i) the buildup of confining pressure, (ii) pillar shape distribution profiles, (iii) extent of the yield zone and (iv) growth of the pillar core. Moreover, Wilson's theory hinges on assumptions that do not apply to St. Peter Sandstone pillars. As a result, estimates of St. Peter Sandstone pillar strength using Wilson's theory seem unrealistically low.

Various researchers have employed numerical methods to estimate pillar strength for hard rocks (Lunder and Pakalnis, 1997; Esterhuizen, 2007; Arthur et. al., 2016), and coal (Jaiswal et al., 2009; Mohan and Sheorey, 2001). Despite the numerous application of numerical models in pillar design, however, numerical models have previously never been used to predict pillar strength of St. Peter Sandstone.

The lack of adequate pillar design method for St. Peter Sandstone poses safety and economic consequences for the mining industry. For instance, at the Pattison Sand Mine (an active room and pillar St. Peter Sandstone mine location in Clayton, Iowa), the United States Mine Health and Safety Administration (MSHA) wrongly interpreted the occurrence of "pinch out" failures (which is a gradual erosion at the roof-pillar intersection observed in small and large size pillars) as a direct evidence that, the pillars were overstressed. Therefore, MSHA recommended that pillar sizes be increased by 150

to 250%. If these recommendations were implemented, it would have eventually closed the mine as the mine would no longer be economically viable. From MSHA perspective, “pinch out” failure was seen as a pillar failure problem, a conclusion which ultimately led to the shutdown of Pattison Sand Mine in 2010. Thus the need to develop a pillar design method for St. Peter Sandstone is vital for the mining industry in terms of safety, economics, and productivity.

1.3. RESEARCH OBJECTIVES

Overall, this research seeks to provide further understanding of the factors affecting pillar strength and a means to design safe and economic pillars in St. Peter Sandstone. The primary objectives of this research are:

1. To elucidate factors contributing to ground control problems in St. Peter Sandstone mines;
2. To derive a pillar design method for St. Peter Sandstone using numerical modeling;
3. To investigate the mechanics of “pinch out” failure in St. Peter Sandstone.

1.4. RESEARCH METHODOLOGY

To accomplish objective 1, an extensive literature review will be conducted to establish factors that contribute to ground control problems in mines. This research will use laboratory testing and investigation to establish the physical and mechanical properties of St. Peter Sandstone, Shale, and limestone. Additionally, the research will use field instrumentation to measure the stress and deformation characteristics of the pillar and roof rock materials. In particular, stressmeters and extensometers will be installed in St. Peter Sandstone pillars and roof to measure stress change and roof deformation respectively, during mine development. Moreover, the research will use field investigations to: (i) evaluate the condition of pillars that have worked successfully and unsuccessfully in room and pillar St. Peter Sandstone mines; and (ii) document typical ground control practices and challenges in St. Peter Sandstone mines. Empirical studies will involve extensive collection and creation of a database of case histories from field observations and field experience on existing St. Peter Sandstone room and pillar mines. Empirical modeling will entail scientific and engineering representation of actual mining experiences of St. Peter Sandstone based on the empirical studies.

To achieve objective 2, this research will develop three-dimensional (3D) finite difference numerical models of mine pillars. The researcher will then calibrate and validate the models with field stress change measurements obtained through field instrumentation and monitoring exercise. The validated numerical model will be used to estimate pillar strength for St. Peter Sandstone. The study will propose a pillar strength equation for St. Peter Sandstone based on the numerical simulation results to achieve objective 2. The work will include sensitivity analysis of the results.

To accomplish objective 3, the research will investigate possible causes of pinch out failure in St. Peter Sandstone. Specifically, the research will explore three possible hypotheses. First, the candidate will use particle size analysis to investigate whether or not pinch out failure is primarily controlled by variation in grain size distribution within the St. Peter Sandstone. Second, the researcher will use the validated numerical model to investigate whether or not pinch out failure is related to changes in the immediate roof rock properties. Finally, the researcher will use numerical modeling to ascertain whether the shape of mine openings influence the occurrence of pinch out failure.

1.5. SCIENTIFIC AND INDUSTRIAL CONTRIBUTIONS

Presently, no research has been done to develop valid, scientific, and engineering solutions to the pillar design problem for St. Peter Sandstone. This fundamental research study is a pioneering effort towards developing such a criteria, which will be useful for the St. Peter Sandstone room and pillar mining industry in the United States. The pillar design method developed in this research will be useful for underground mining of similar geomaterials (e.g. Jordan Sandstone, Oil Creek Sandstone, Hickory Sandstone, Swam River Sandstone, and Athabasca Oil Sands) that have low cohesion and high friction angles. Also, the researcher is not aware of any research that has methodologically calibrated numerical models with field stress change measurements. The field monitoring and instrumentation also allow this research to test whether classical beam theory applies to St. Peter Sandstone and the mining conditions. In addition, this study will reveal possible causes of pinch out failure at St. Peter Sandstone mines. Investigating the causes of pinch out failure is critical for mine health and safety, productivity and economics.

This study is intended to advance the research frontiers on pillar design in rock mechanics. Specifically, this study will contribute to the body of knowledge on pillar design that will guide federal, state, and local mine health and safety officials to make effective decisions to improve the health and safety of personnel and equipment. This work will also provide a tool for economic and technical evaluation of St. Peter Sandstone deposits where the room and pillar mining method is to be utilized for mining. Additionally, the study will reveal critical factors that affect the stability of St. Peter Sandstone pillars and make appropriate recommendations to solve these ground control problems. The outcomes of this research are expected to assist engineers in effective mine planning and design while improving the productivity of personnel and equipment at St. Peter Sandstone room and pillar mines. Facilitating optimum pillar design for St. Peter Sandstone will boost hydraulic fracturing sand production using room and pillar underground mining and, thus, enable the production of gas and oil from unconventional reservoirs in the United States. Hydraulic fracturing is expected to contribute to the US energy independence and make it the world's largest producer of natural gas. Natural gas production is needed to generate electricity, heat buildings, fuel vehicles, and for domestic and industrial purposes.

1.6. STRUCTURE OF DISSERTATION

This dissertation will be outlined in six Sections (Table 1.1).

Section 2 presents a comprehensive review of all relevant literature. This section provides detailed literature survey on (i) the geology of St. Peter Sandstone, (ii) properties of locked sands, (iii) pillar design methods, and (iv) numerical methods in pillar design. Section 3 presents field studies and monitoring. This Section will contain: (i) study sites, (ii) field investigations, (iii) ground control challenges at St. Peter Sandstone mines, (iv) stress change monitoring, (v) roof displacement monitoring and particle size analysis. Section 4 contains detailed numerical modeling. Key topical outlined in this section includes (i) numerical calibration and validation; (ii) pillar stress modeling; (iii) pillar strength modeling; and (iv) sensitivity analysis. The mechanics of pinch out failure is presented in Section 5.

The Section will evaluate three hypotheses including the geometry of mine opening, roof rock properties, and particle size analysis. Conclusions and recommendations for future work are discussed in Section 6.

Table 1.1. Research task adopted

Section 2	**Literature Review**	
	Geology of St. Peter Sandstone	
	Properties of locked Sands	
	Experimental test on St. Peter Sandstone	
	Pillar design methods	
Section 3	**Field Studies and Monitoring**	**Objective 1**
	Study sites	
	Field investigation	
	Ground control challenges	
	Stress change monitoring	
	Roof displacement monitoring	
Section 4	**Numerical Modeling**	**Objective 2**
	Numerical calibration	
	Numerical validation	
	Pillar stress modeling	
	Pillar strength modeling	
	Sensitivity analysis	
	Safety factor and extraction ratio analysis	
Section 5	**Causes of Pinch out Failure**	**Objective 3**
	Pillar geometry hypothesis	
	Roof rock properties hypothesis	
	Particle size analysis hypothesis	

2. LITERATURE REVIEW

Section 2 presents a comprehensive review of all relevant literature. It covers: (i) the geology of St. Peter Sandstone, (ii) properties of locked sands, (iii) experimental tests on St. Peter Sandstones, and (iv) pillar design methods, with special emphasis on those that are applicable to St. Peter Sandstone.

2.1. GEOLOGY OF ST. PETER SANDSTONE

The name St. Peter's was obtained from St. Peter's River (formerly called the Minnesota River). Sardeson (1896) amended the St. Peter's Sandstone to St. Peter Sandstone. The St. Peter Sandstone formation was known as Key Sandstone, Burgen Sandstone and First Sandstone in Arkansas, Oklahoma, and Missouri, respectively (Giles, 1930). Captain Jonathan Carver in 1766-1768, was the first to describe the St. Peter Sandstone while mapping and exploring along the Mississippi River (Dittes and Labuz, 2002; Mossler, 2008). In 1847, Owen was the first to discover St. Peter Sandstone exposure along the Minnesota River (Giles, 1930). Owen (1947), described the St. Peter Sandstone as an extremely weak rock that could be cut with a knife. In 1817, Long described it as a whitish or yellowish rock material that could be called sand instead of sandstone. In 1824, Dr. Keating described it as a friable sandstone (Dittes, 2015).

The St. Peter Sandstone is a homogenous stratified arenaceous clastic sedimentary rock of middle Ordovician age. The formation covers more than 576,000 km^2 of middle North America (Dittes and Labuz, 2002). It was initially recognized along the Upper Mississippi Valley regions (Missouri, Iowa, Minnesota, and Illinois). However, it is now widespread in areal extent in Arkansas, southern Wisconsin, Kansas, Indiana, Tennessee, Kentucky, Arkansas, Oklahoma, South Dakota, Nebraska, Michigan, and Ohio (Giles, 1930, Dittes and Labuz, 2002; Dapples, 1955; Cole, 1975; Mai and Dott, 1985; Davis 2011; Suhm and Ethington, 1975; Jones 2009; Dake, 1921). The St. Peter Sandstone is deposited near-surface in western, southern and south-central Wisconsin, southern Minnesota, northeastern Iowa, northern Illinois, southern and central Missouri, and northern Arkansas (Mai and Dott, 1985; Harris, 1997; Davis 2011; Davis, 2014; Glick and Frezon, 1953). On the contrary, the St. Peter Sandstone outcrop is buried deep in

eastern Wisconsin, Michigan, eastern Indiana, Ohio, Kentucky, Tennessee, and eastern Kansas (Mai and Dott, 1985; Leatherock, 1945; Dapples, 1955; Barnes et al., 1996; and Dake, 1921).

The stratigraphic units of St. Peter Sandstone and adjacent formations are equivalent in Missouri, Iowa, Minnesota, Illinois, Arkansas, and other Mississippi Valley states (Giles, 1930; Dappe, 1955). The Platteville formation unconformably overlies the St. Peter Sandstone in Iowa, Missouri, and Illinois. The Shakopee uncomfortably underlies the St. Peter Sandstone in Missouri, Iowa, Wisconsin, Arkansas, Illinois, Northwest Oklahoma, and southern Minnesota (Dittes, 2015; Mossler, 2008). In Missouri and Arkansas, the Joachim formation unconformably overlies the St. Peter Sandstone. Except in Calhoun County, the Joachim formation overlies the St. Peter Sandstone in Illinois (Giles, 1930). However, in other locations, the Platteville limestone or Glenwood shale, overlies the St. Peter Sandstone formation. The Platteville is deposited on top of the St. Peter Sandstone in Iowa and Wisconsin. After a noticeable stratigraphic anomaly, the Shakopee formation underlies the St. Peter Sandstone formation in Iowa and Illinois (Giles, 1930). The St. Peter Sandstone underlies the Everton in Missouri.

The thickness of St Peter Sandstone is not uniformly distributed and differs from place to place. The thickness of St. Peter Sandstone is: 24 -30 m in Missouri (Missouri Department of Natural Resources, 2014); 25 m in northern Wisconsin (Mudrey et al., 1987); 0 to 43 meters in Indiana with the highest reaching 18 to 102 m in Jasper County, Indiana (Indiana Geological Survey, 2017); 30 to 60 m in northern Illinois, with the maximum thickness being 120 to 180 m northwards of the Sandwich fault zone (Visocky et al., 1985); and 366 m at the Michigan Basin (Catacosinos et al., 2001). The thickness of St. Peter Sandstone in Clayton County, Iowa, is typically 12.19 – 15.24 meters (Geological Society of Iowa, 2000). In Clayton County, IA, the full thickness of St. Peter sandstone is seen at Pike Peak State Park, where it ranges from 27 to 68 m. Olcott (1992) found that the thicknesses of St. Peter Sandstone varied significantly in Michigan, Iowa, Minnesota, and Wisconsin. Viscocky et al. (1985) reported that the variability of the thickness of St. Peter Sandstone is due to erosional channels and karstic terrains underlying carbonate rocks.

The St. Peter Sandstone comprises of two members (Tonti and Starved) based on the grain size, the type and sequence of sedimentary structures (Fraser, 1976). The Tonti Member is finer of the two members and displays a change in character from north to south. In north-central Illinois, it has characteristics similar to sublittoral sheets sandstones as described by (Goldring, 1966, Goldring and Bridges, 1973). It is thin-bedded, has wavy bedding planes, and a few silty laminae. It displays extensive burrowing that are filled with coarse-grained sands (Goldring, 1966). In south-central Wisconsin, it is more coarse-grained compared to that present in north-central Illinois and contains tabular and concave upwards cross strata as much as 15 m thick (Fraser, 1976). The upper part of the Tonti Member in southwestern Wisconsin and south eastern Minnesota, contains small-and large-scale trough cross strata, suggesting sediments transport to the west (Fraser, 1976). Dapples (1955) reported that these sands are deposited by longshore currents oriented along the northeast and southwest. Elsewhere in Minneapolis, the Tonti Member exhibits small and large-scale trough cross-strata and low angle planar cross-strata, signifying that it was deposited on the shores (Fraser, 1976).

The Starved member of the St. Peter Sandstone is medium to coarse-grained. It is divided into five structural zones based on the characteristic sequence of bedding structures. These structural zone from base upwards are: (i) small-scale trough and tabular cross beds; (ii) large-scale tabular to convex upward cross beds (iii) large-scale trough cross beds; (iv) alternating beds of low angle, small-scale trough cross beds and beds of irregular horizontal laminae; and (v) apparent massive beds. Fraser (1976) compared the structures and textures of the Starved Member of the St. Peter Sandstone and concluded that, it is not of tidal, eolian dune, fluvial or deltaic origin. Swett et al. (1971) also found that tidal sand bodies are not present in the Starved Member. Furthermore, McKee (1961) found that structures which suggest eolian dunes are missing in the Starved Member. On the contrary, Folk (1968) revealed that bimodal textures is a feature of interdune eolian areas. While Fraser (1976) reported that the texture of the Starved Member is associated with burrowing activity. This burrowing could be as a result of microorganism action (Fraser, 1976). Fraser, (1976) found that the Starved Member is considered an offshore shoal because: (i) it is an elongated sand body parallel to the shoreline basin in which it was deposited; (ii) it separates laterally equivalent

formations of different rock-types; (iii) it was deposited in progressively shallower water upward in the section; and (iv) it overlies deeper water deposits, and deeper water deposits also occur southeast and northwest in the upper part of the Tonti Member. The Starved Member is identical in shape and contains several structures indicative of fluvial deposits (Allen, 1965; Potter, 1967; Visher, 1972). The dip and dip direction of the Starved Rock Member is at right angle to the trend to the structural sequence. Flood-plain deposits are not present in this member (Fraser, 1976).

There is controversy over the origin of the strata of St. Peter Sandstone. Some researchers believe its deposition is characteristic of eolian origin (Mazzullo and Ehrlich, 1983) while others believe it is of marine origin (Mazzullo and Ehrlich, 1983; Dake, 1921; Devan, 1926; Lamar, 1927; Elder, 1936). The study confirmed that the St. Peter Sandstone in Clayton Iowa is deposited by marine origin (Bagherieh, 2015).

2.2. CHARACTERISTICS OF LOCKED SANDS

Dusseault and Morgenstern (1979) introduced the term locked sands and distinguished it from dense sand and sandstone. They characterized locked sands as an engineering material having no cohesion, highly quartzose mineralogy, high strength, steeply curved failure envelopes, low porosity, considerable age, lack of interstitial cement, brittle behavior, residual shear strengths of 30-35^{o}, and extremely large dilation rates at failure. These characteristics are distinct from those of dense sand or sandstone. For example, the strength of dense sand is a function of relative density, while the strength of sandstone is a function of the amount of interstitial cementation (Abdelaziz et al., 2008). Very few investigations have been conducted on locked sands at different locations (Dusseault and Morgenstern, 1979; Barton et al., 1986; Richards and Barton, 1999; Dittes and Labuz, 2002; Creswell and Barton, 2003; Creswell and Powrie, 2004; Abdelaziz et al., 2008; Dittes, 2015; Bagherieh, 2015). These investigations have revealed that Ottawa sand, St. Peter Sandstone, Athabasca Oil Sand, Swam River Sandstone, and Lower Cretaceous McMurray Sand, are considered locked sands. The basic criteria these investigators (Dusseault and Morgenstern, 1979; Barton et al., 1986; Richards and Barton, 1999; Dittes and Labuz, 2002; Creswell and Barton, 2003; Creswell and Powrie, 2004; Abdelaziz et al., 2008; Dittes, 2015; Bagherieh, 2015) used to

characterize locked sands are: visual inspection, mineralogy, macro fabric, porosity, relative densities, and shear strength. This Section describes four key properties of locked sands, namely: porosity, relative density, fabric and grain surface characteristics, and strength of locked sands.

2.2.1. Relative Density of Locked Sands. Relative density defines the state of compaction of granular materials. Thus, relative density can indicate the in-situ looseness or denseness of a granular material. Relative density (D_r) is defined in Equation (1):

$$D_r = \frac{e_{max} - e}{e_{max} - e_{min}} \quad (1)$$

where: e is the in-situ void ratio of the soil; e_{min} is the void ratio of the soil in the densest state, and e_{max} is the void ratio of the soil in the loosest state. In general, a D_r of 0% means that the soil is very loose whilst a D_r of 100% indicates that the soil is very dense. Thus, engineers can qualitatively use the values of D_r to describe granular soils. Table 2.1 shows the qualitative descriptions of soils based on its relative densities.

Table 2.1. Qualitative description of soil based on relative density (Holtz et. al., 1981)

Relative density (%)	Description of soil
0-15	Very loose
15-50	Loose
50-70	Medium
70-85	Dense
85-100	Very dense

Relative densities of locked sands have been reported by several researchers (Dusseault and Morgenstern, 1979; Abdelaziz et al., 2008; Celauro et al., 2014). As shown in Table 2.2, the relative density of locked sands ranges from 100 to 135%. Soils with a relative density of 100 to 135% are very dense sand. Dusseault and Morgenstern, (1979) credited the high relative density of locked sand to its unusual fabric.

Table 2.2. Relative densities of locked sands

Locked sands	Relative density (%)	Authors
Ottawa sand C-109	100	Dusseault and Morgenstern, (1979)
Ottawa sand 20-30 mesh	100	Dusseault and Morgenstern, (1979)
Oil sand shearbox series C	>100-120	Dusseault and Morgenstern, (1979)
All oil sand specimens	100-135	Dusseault and Morgenstern, (1979)
St. Peter Sandstone	100-135	Dusseault and Morgenstern, (1979)
Swan River Sandstone	100-125	Dusseault and Morgenstern, (1979)
McMurray sand	125	Abdelaziz et al., (2008)

Holtz et al. (1981) reported that the relative density of granular soils depends on grain size, grain shape, nature of the grain size distribution curve, fine content and the fabric of the soil. Particle size analysis reveals the grain sizes, nature of the grain-size distribution, and the amount of fine or coarse content. Thin section petrographic analysis and scan electron microscope techniques are used to characterize the fabric of granular soils or rock.

Various researchers have conducted particle size analysis on locked sands. For instance, Thiel (1935), Bagherieh (2015) and Dittes (2015) conducted particle size analysis on St. Peter Sandstone. Wigham et al., (1989) and Prowse, (1983) conducted particle size analysis for oil sands while Mavis and Wilsey (1936), Alostaz, et al. (2008), Erdoğan et al. (2017) conducted particle size analysis for Ottawa sand.

Thiel (1935) and Bagherieh (2015) described the particle sizes of St. Peter Sandstone based on the textural characteristics of the samples without quantifying the fraction of fine and coarse grains. Dittes (2015) attempted to classify the particle sizes of St. Peter Sandstone in Minnesota according to the Massachusetts Institute of Technology (MIT) engineering classification system. Like, Bagherieh (2015), Dittes's particle size analysis was limited to only two samples.

Till date, no research has been conducted to quantify the fraction of fines, medium or coarse sands using the textural and engineering soil classification systems.

2.2.2. Porosity of Locked Sands. Porosity is the proportion of soil or rock that have voids. Thus, porosity is the ratio of the volume of voids to the total volume. In general, metamorphic and igneous rock have low porosities unless they are fissured. Sedimentary rocks have relatively high porosity compared with igneous and metamorphic rocks. Barrell, (1914) reported the average porosity of sedimentary rocks to be: 8.2% for shale; 14.8% for sandstone; 5.3% for limestone; 8.5% for all sedimentary rocks. The porosity of locked sands ranges from 19.1 to 34%. Table 2.3 shows the porosity of locked sands determined by several researchers. From Table 2.3, it can be deduced that the porosity of locked sands is about 2 to 4 times that for all sedimentary rocks, although locked sands are sedimentary rocks.

Table 2.3. Porosities of locked sands

Locked sands	Porosity (%)	Authors
Ottawa sand C-109	31.3	Dusseault and Morgenstern (1979)
Ottawa sand 20-30 mesh	34.0	Dusseault and Morgenstern, (1979)
Oil sand shearbox series C	33.9	Dusseault and Morgenstern, (1979)
All oil sand specimens	31.3	Dusseault and Morgenstern, (1979)
St. Peter Sandstone	27.0	Dusseault and Morgenstern, (1979)
Swan River Sandstone	34.0	Dusseault and Morgenstern, (1979)
McMurray sand	34.0	Abdelaziz et al. (2008)
St. Peter Sandstone	19.1	Manger (1963)
St. Peter Sandstone	28.3	Thiel (1935)
St. Peter Sandstone	27.5	Schwartz (1963)
St. Peter Sandstone	28.3	Payne (1939)
St. Peter Sandstone	28.3	Dusseault (1977)
St. Peter Sandstone	24.3	Bagherieh (2015)
St. Peter Sandstone	30.5	Bagherieh (2015)
St. Peter Sandstone	26.3	Dittes (2015)
Ottawa sand	35.9-41.2	Mavis and Wilsey (1936)

2.2.3. Fabric and Grain Surface Characteristics of Locked Sands. The fabric of rock defines all the textural and structural features (Whitten and Brooks, 1972). Siever (1959) classified the fabrics of intergranular material based on the grain contacts as floating, tangential, straight, concavo-convex or interpenetrative, and sutured (Figure 2.1). Dittes (2015) found that the types of grain contacts depend on the variability of solubility resulting from impurities and changes in radii of curvature. Floating grains have no grain contacts; tangential contacts have low contact area and high porosity; straight contacts have low to medium contact area and medium to high porosity; concave-convex or interpenetrative contacts have medium contact area and medium porosity; and sutured contacts have medium to high contact area and have low to medium porosity.

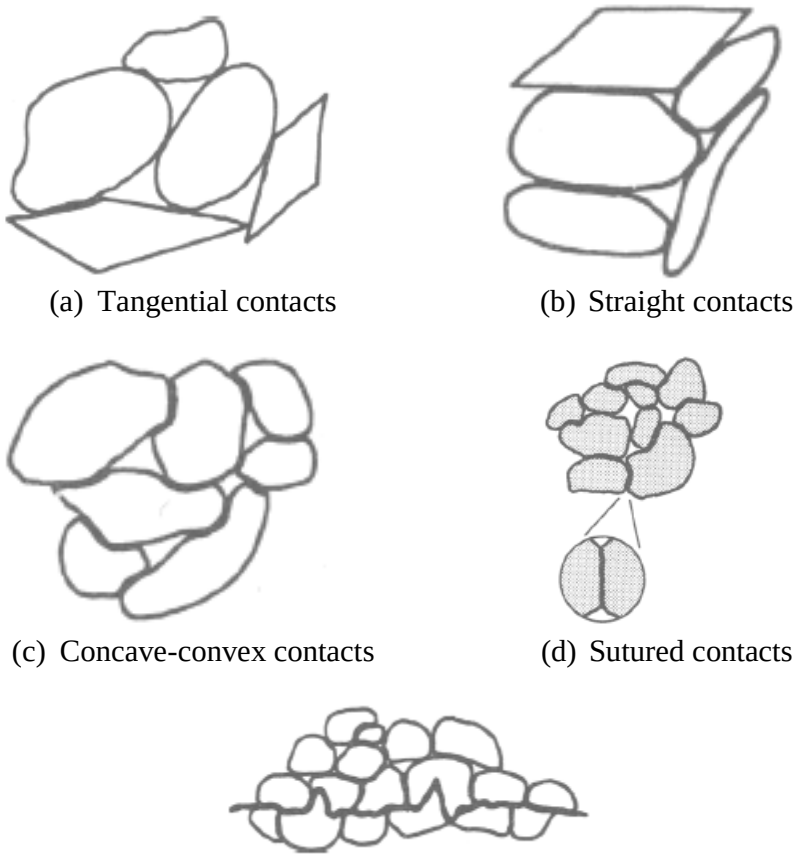

(a) Tangential contacts (b) Straight contacts

(c) Concave-convex contacts (d) Sutured contacts

(e) Carbonate type stylolite

Figure 2.1. Intergranular fabric classification (After Siever, 1959)

Bagherieh (2015) revealed that the intergranular fabric classification is useful for assessing stress condition. He revealed that sutured contacts are as a result of pressure.

Dusseault and Morgenstern (1979) found that the grain contact for Swam River Sandstone, McMurray formation, and St. Peter Sandstone is sutured (Figure 2.2c). Dittes (2015) discovered that the grain contact for St. Peter Sandstone may be tangential, concavo-convex and straight (Figure 2.3). However, Bagherieh (2015) found that the grain contacts of St. Peter Sandstone is tangential (Figure 2.4).

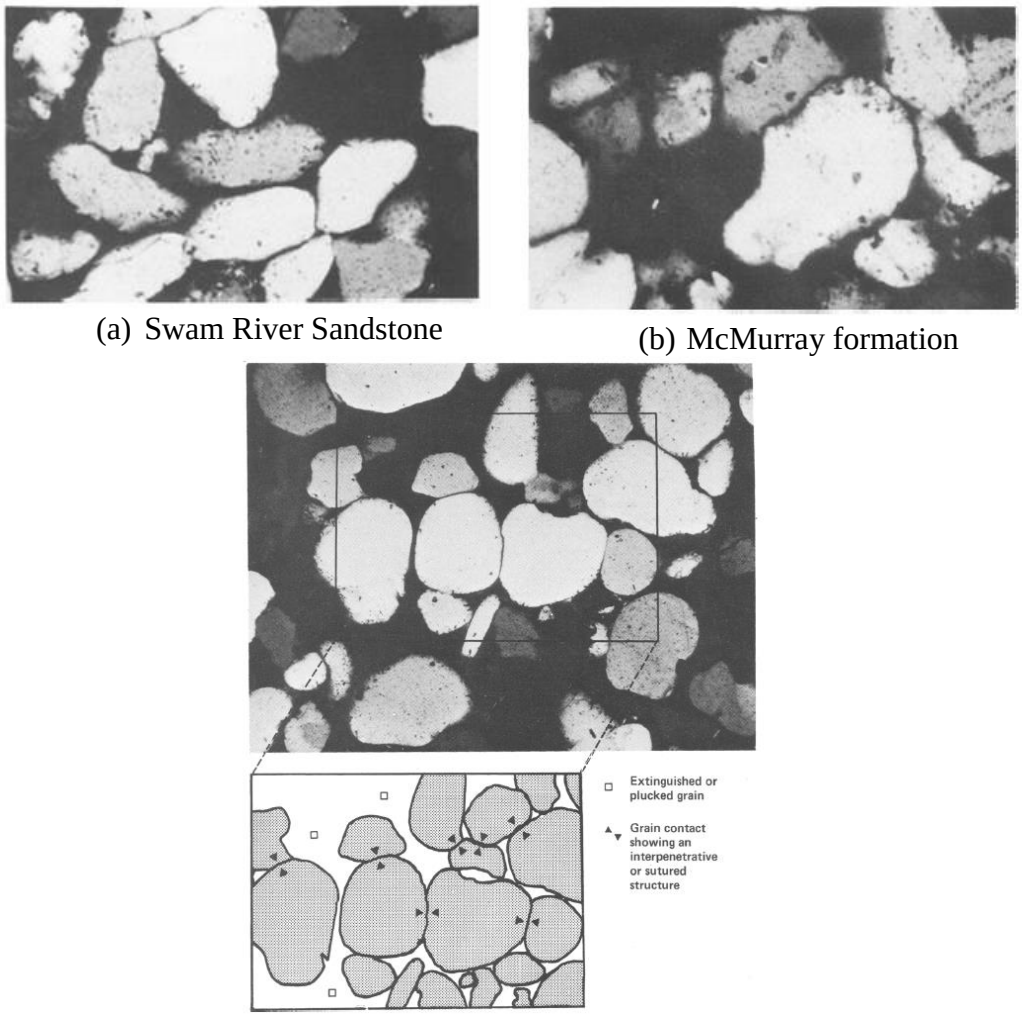

(a) Swam River Sandstone (b) McMurray formation

(c) St. Peter Sandstone

Figure 2.2. Optical electron micrographs of locked sands: (a) Swam River Sandstone; (b) McMurray; (c) St. Peter Sandstone (Dusseault and Morgenstern, (1979)

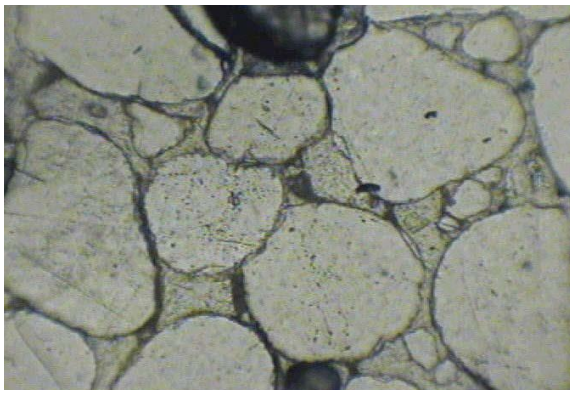

Figure 2.3. Transmitted light micrograph for St. Peter Sandstone (After Dittes, 2015)

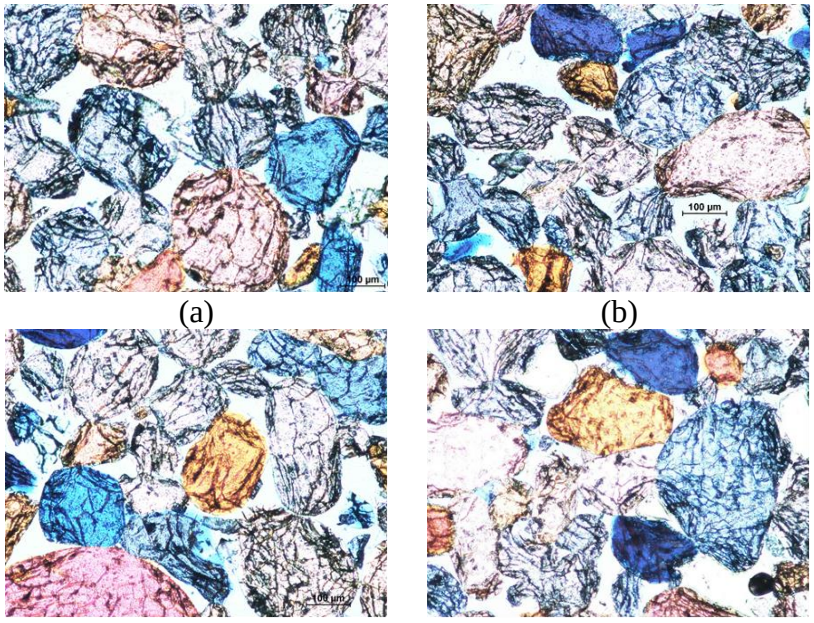

(a) (b)

(c) (d)

Figure 2.4. Thin section images for St. Peter Sandstone (After Bagherieh, 2015)

There is controversy in the grain and surface texture of locked sand. Dusseault and Morgenstern (1979) established that the interlocked textures of St. Peter Sandstone, Swam River Sandstone and McMurray formation was characterized by long and interpenetrative grain contacts (Figure 2.2). Also, Dusseault and Morgenstern (1979) discovered that the fabric of an undisturbed sample of McMurray formation displayed interpenetrative, long contacts and corroded crystal overgrowth while the fabric of St. Peter Sandstone displayed solution cavities or indentations (Figure 2.5).

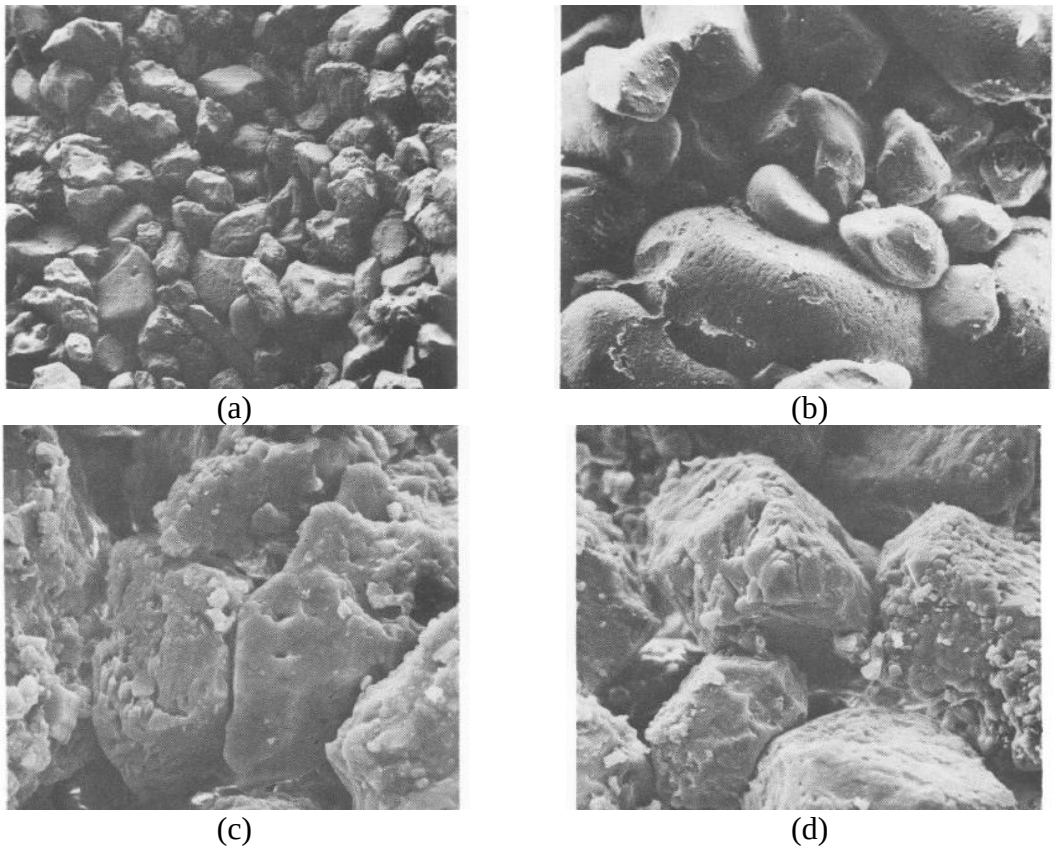

(a) (b)

(c) (d)

Figure 2.5. Locked sand fabric and grain surface texture for: (a) McMurray formation medium-grained fraction (note variability and roundness); (b) McMurray formation fined-grained fraction (mixed solution and recrystallization); (c) St. Peter Sandstone (fined grained fraction, very well rounded and surface concavities; (d) Swam River Sandstone; (undisturbed fabric, gross variations of surface rugosity are obvious). (After Dusseault and Morgenstern, 1979)

In this author's research group, Bagherieh (2015) concluded that the grain contacts of St. Peter Sandstone this research study area are not interpenetrative (Figures 2.4 and 2.6). Dusseault (1977) and Dittes (2015) also presented evidence of pressure solutions around the grain contacts of St. Peter Sandstone (Figure 2.7 and 2.8). The contrasting views from different researcher suggest that locked sands at different location may have different characteristics.

Mazzullo and Ehrlich (1983) postulated that the grain shape of the quartz grains could be inherited from the origin, modified by abrasion during transport, and/or modified by diagenetic process.

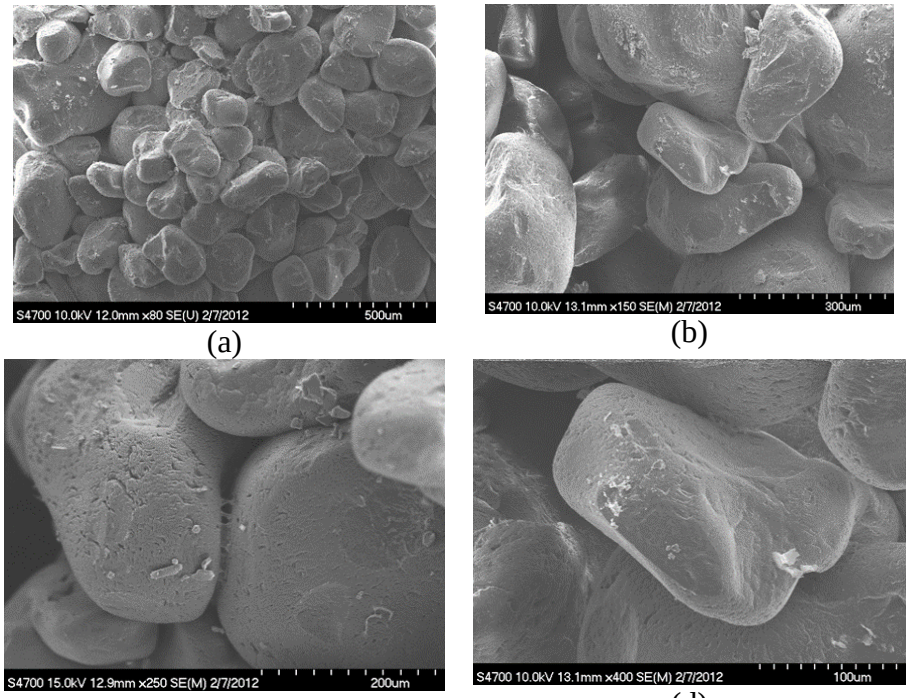

Figure 2.6. Scan electron microscope for St. Peter Sandstone (After Bagherieh, 2015)

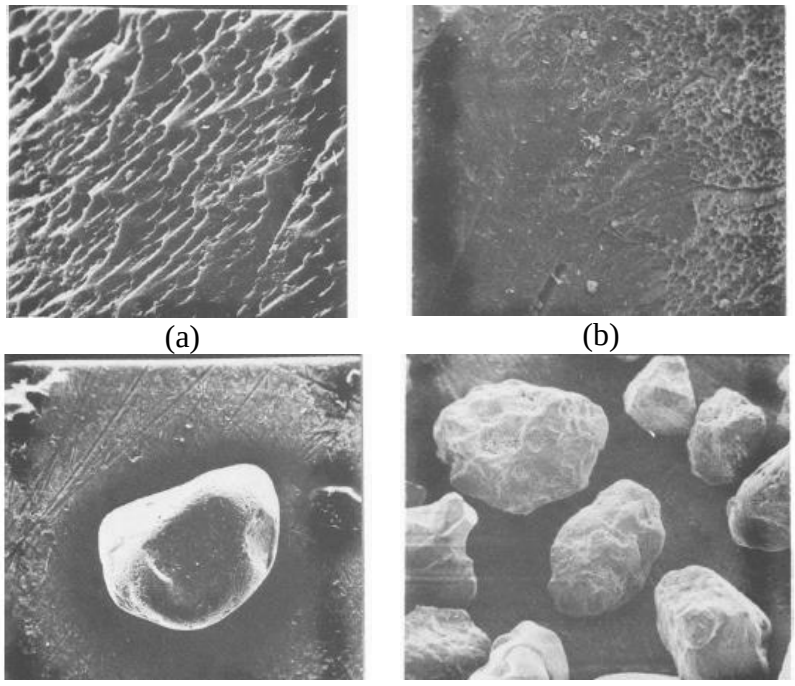

Figure 2.7. Grain surface textures for (a) Swam River Sandstone; (b) McMurray; (c) St. Peter Sandstone; (d) Preglacial sand (After Dusseault and Morgenstern, 1979)

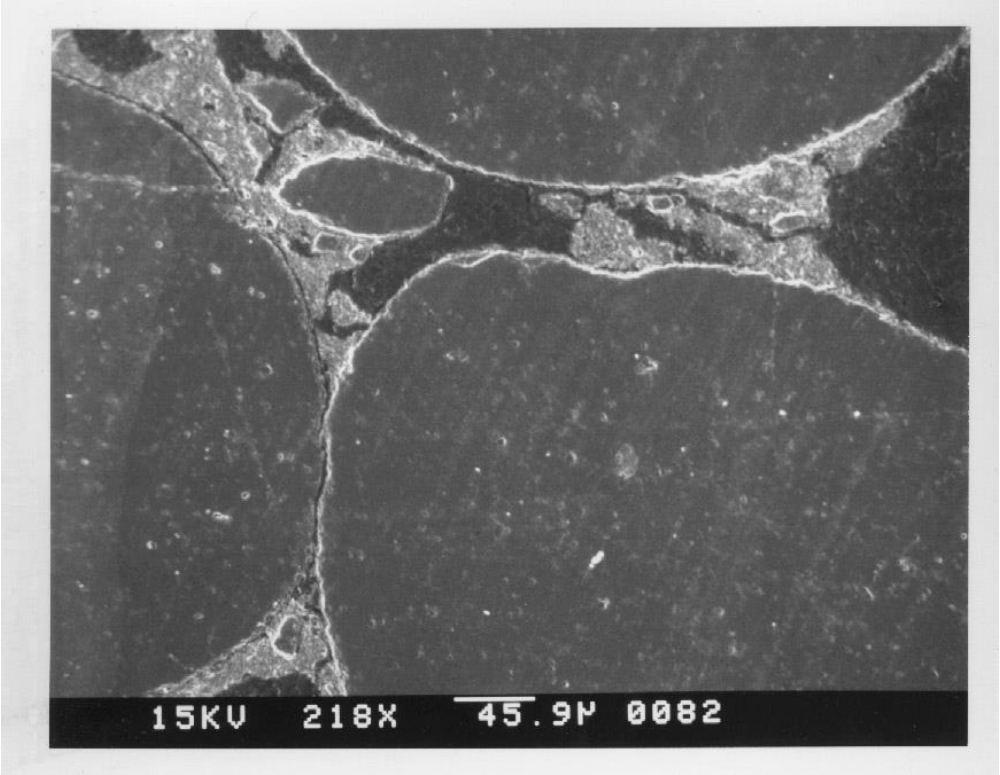

Figure 2.8. Scan electron microscope electron for St. Peter Sandstone (Dittes, 2015)

Overall, the scan electron microscope analysis reveals that the grain shapes are irregular. They further postulated that the irregular grain shapes may be attributed to: (1) conchoidal fractures on its surface, which is very characteristics of material freshly liberated by mechanical means (Krinsley and Doornkamp, 1973); (2) Protuberances and re-entrants which are source inherited; (3) overgrowth; and/or (4) shallow dislike indentations, which is manifested by concavo-convex surfaces. Pitman (1972) found that quartz overgrowth is featured in St. Peter Sandstone and that most of these quartz overgrowth associated with St. Peter Sandstone are worn and abrasion superimposed. This means that the overgrowths are formed in the source rock. The abrasions associated with grain shape feature isolated scratches, curved grooves, nonoriented v-shapes, conchoidal fractures and roundness of the edges. Figure 2.9 shows scan electron microscope images of grain shapes showing conchoidal fractures, abrasion and Protuberances and re-entrants features. More details of quartz overgrowth associated with St. Peter Sandstone are discussed in Mazzullo and Ehrlich (1983).

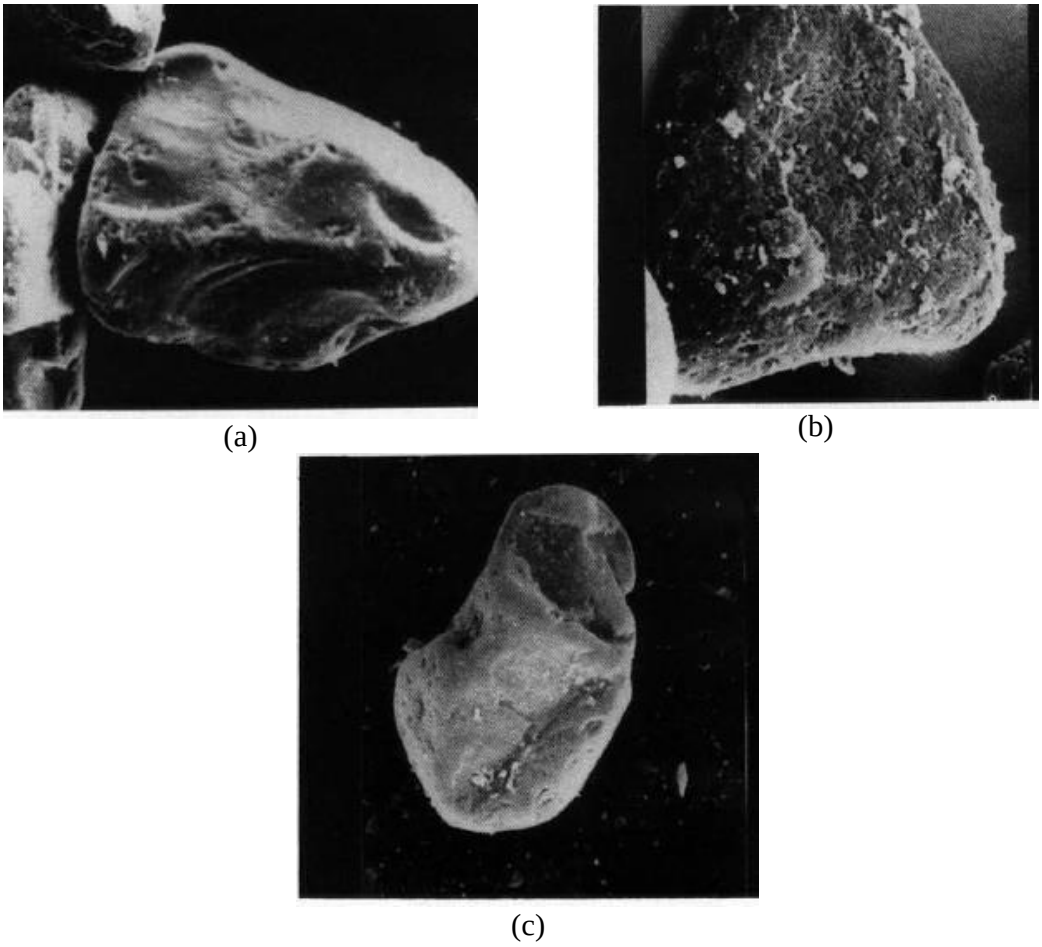

(a) (b)

(c)

Figure 2.9. Irregular grain shape of St. Peter Sandstone showing: (a) conchoidal fractures; (b) abrasion features; (c) protuberances and re-entrants (Mazzullo and Ehrlich,1983)

2.2.4. Strength Mechanics of Locked Sands. Several researchers (Watson, 1938; Payne,1967; Schwartz, 1939; Sterling, 1977; Petersen, 1978; Labuz et al.,1998; Dusseault and Morgenstern, 1979; Dittes and Labuz, 2002; Dittes, 2015; Bagherieh, 2015) have conducted laboratory tests on locked sands. The laboratory test revealed almost no cohesion and high friction angle (57^o to 70^o).

Locked sand behaves like a brittle rock and requires careful sampling and specimen preparation to produce undisturbed yet high-quality specimens (Payne,1967; Petersen, 1978; Bagherieh, 2015). Of interest to this study, is the strength of St. Peter Sandstone. The researcher has presented more details on the strength of St. Peter Sandstone in Section 2.3.

2.3. UNIAXIAL COMPRESSIVE STRENGTH OF ST. PETER SANDSTONE

The uniaxial compressive strength (UCS) is an important parameter used extensively in pillar design. The uniaxial compressive strength of St. Peter Sandstone has been reported by numerous investigators (Schwartz, 1939; Payne, 1967, Yardley, 1978, Sterling, 1978, Petersen, 1978, Dittes and Labuz, 2002, Dittes, 2015, Bagherieh, 2015). As a result of the friable nature of the St. Peter Sandstone, attempts to use conventional coring methods have been unsuccessful (Schwartz, 1939; Payne, 1967; Sterling, 1978, Petersen, 1978; Dittes and Labuz, 2002; Dittes, 2015; Bagherieh, 2015). As a result, the most challenging issue regarding uniaxial compressive strength testing for St. Peter Sandstone, is the shaping of specimen sizes for the UCS test (Petersen, 1978; Bagherieh, 2015; Dittes, 2015).

2.3.1. Sample Collection. Researcher's attempts to collect undisturbed samples of St. Peter Sandstone for testing is very difficult (Payne, 1967, Petersen, 1978, Bagherieh, 2015). Attempts by early investigators to use a split tube and Shelby tube sampling devices were unsuccessful (Payne, 1976).

Also, attempts to use the Dennison core barrel rotary sampler have also been unsuccessful due to the fragmentation of the sample by the coring fluids and water (Payne, 1967). Petersen (1978) obtained St. Peter Sandstone blocks from rock debris of a freshly exposed wall failure. The only undisturbed sample obtained from coring was an instance where an NX core barrel was used in conjunction with a moderately dense drilling fluid (Payne, 1967).

Bagherieh (2015) obtained St. Peter Sandstone samples from blasting activity or ribs of recent pillar spalling activity at the Pattison Sand Mine. These rock samples were transported from Pattison Sand Mine at Clayton, Iowa to Missouri University of Science and Technology, Rolla, Missouri. Thus, specimens may have been disturbed by blasting vibrations and road transportation in a manner that was not visible to the human eye and thus not detected by this researcher. Thus, collecting undisturbed St. Peter Sandstone samples are not only cumbersome but also very challenging.

2.3.2. Sample Preparation. Various researchers (Petersen, 1978, Bagherieh, 2015, Dittes, 2015) have reported that preparing St. Peter Sandstone samples for UCS testing is very challenging. Conventionally, coring techniques are used to prepare cylindrical samples for most rocks. Previous attempts to prepare cylindrical specimens for St. Peter Sandstone using split tube and Shelby tube samplers were unsuccessful (Payne, 1967). Generally, due to the friable nature of the St. Peter Sandstone, attempts to use conventional coring techniques has proven unsuccessful (Schwartz, 1939; Payne, 1967; Sterling, 1978, Petersen, 1978; Dittes and Labuz, 2002; Dittes, 2015; Bagherieh, 2015). In addition, an effort to obtain cylindrical cores through exploration drilling methods at Pattison Sand Mine was futile (Bagherieh, 2015). Figure 2.10 shows an unsuccessful coring attempt on St. Peter Sandstone sample at the rock mechanics sample preparation laboratory at Missouri University of Science and Technology. In Figure 2.10a, the core barrel had just been lifted and rock core is badly fractured. In Figure 2.10b, the reader can see that the remaining St. Peter Sandstone block is very friable and can easily be broken by hand. Figure 2.10c shows that the resulting rock core is sand instead of a rock core. Also, Bagherieh (2015) reported that coring slightly cemented St. Peter Sandstone with or without water proved unsuccessful (Figure 2.11 and 2.12).

Most researchers (Schwartz, 1936; Payne, 1967; Petersen, 1978; Bagherieh, 2015) prepare cubic or cuboid St. Peter Sandstone specimens. Other researchers (Payne, 1967; Petersen, 1978; Dittes, 2015) prepared cylindrical St. Peter Sandstone specimens. These researchers (Schwartz, 1936; Payne, 1967; Petersen, 1978; Bagherieh, 2015) cut blocks of St. Peter Sandstone is cut into cubic or cuboid specimens using powered or non-powered hand-held saws. The main merits of using handheld saws are that it is easy to handle and sample disturbance is minimal. Bagherieh (2015) used waterjet technology to trim the St. Peter Sandstone blocks. The main advantage was that it had almost no vibratory effects, hence, the damage to samples caused by cutting is minimal.

For UCS testing, these researcher (Schwartz, 1936; Payne, 1967; Petersen, 1978; Bagherieh, 2015) grinded the surfaces of the specimen to be subjected to loading to ensure smoothness and parallelism of the rock surfaces. They reported that the grinding process is cumbersome and time-consuming. Bagherieh (2015) revealed that one difficulty in the grinding process is the grabbing mechanism used to hold the specimen in

place. Baghereih (2015) reported that the inability to control the specimen's surface chipping even with minimal wheeling speed was very challenging. For these reasons, the grinding process is very limited (Baghereih, 2015). For small size specimens, other researchers have used sandpaper to remove surface irregularities on the sides of the specimens (Petersen, 1978; Baghereih, 2015). Several researchers have used this sample preparation approach (Petersen, 1978; Payne, 1967; Dittes, 2015; and Baghereih, 2015).

The drawback of preparing cubic, cuboid or cylindrical specimens is the disturbance during the sampling preparation process, primarily during the cutting and grinding operations. In addition, the sample preparation is time-consuming and cumbersome.

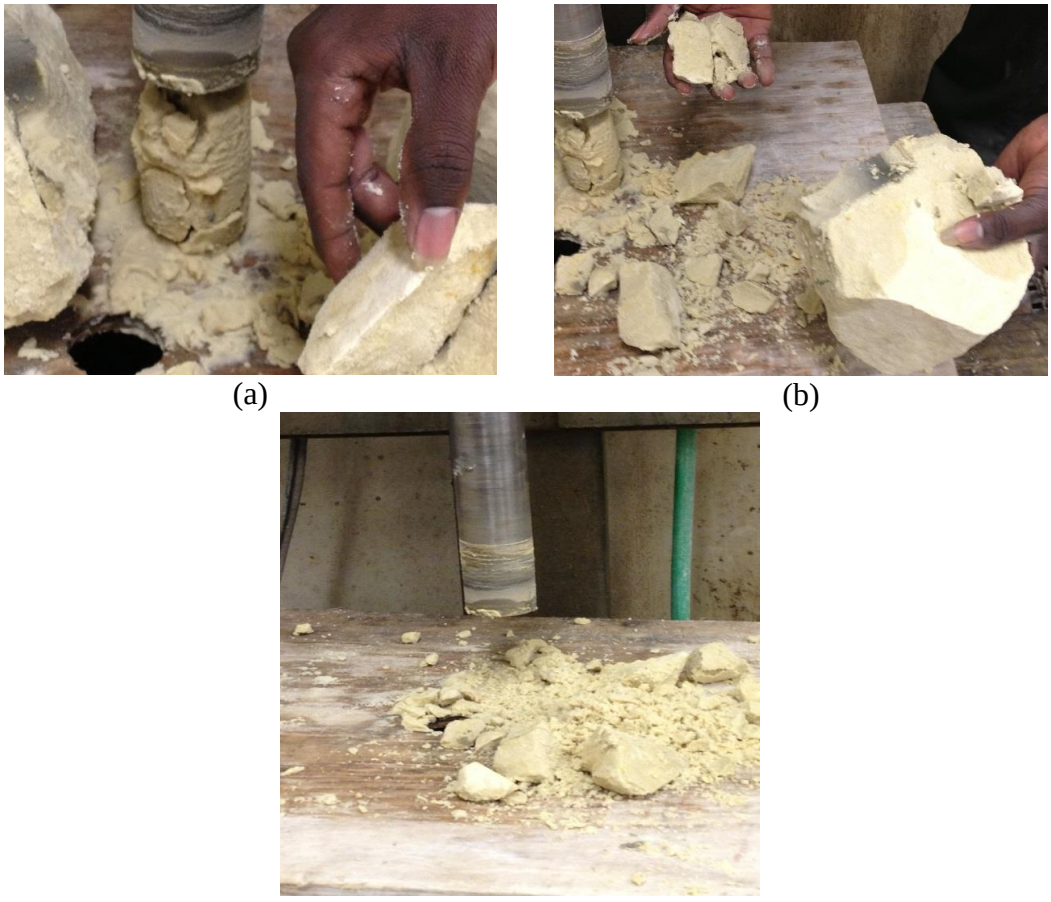

(a) (b)

(c)

Figure 2.10. (a) Unsuccessful coring of St. Peter Sandstone (uncemented) sample; (b) rock can be broken with a hand; (c) specimens is a soil-like

(a) (b)

Figure 2.11. Unsuccessful coring of St. Peter Sandstone (slightly cemented) without water: (a) during coring; (b) after coring

(a) (b)

Figure 2.12. Unsuccessful coring of St. Peter Sandstone (slightly cemented) with water: (a) after coring; (b) specimen difficult to break with hand

For these reasons, attempts to prepare statistical sample sizes for laboratory testing are limited. For instance, Schwartz (1939) was able to prepare only one dry specimen and two wet specimens for laboratory testing. Payne (1967) could prepare only eleven (11) cubic specimens. Petersen (1978) performed uniaxial compressive strength test on 22 cubic and 11 cylindrical St. Peter Sandstone specimens. Petersen (1978) also reported the results of ten (10) in-situ uniaxial compressive strength tests conducted by Yardley (1978). Dittes (2015) prepared seven (7) cylindrical specimens for uniaxial compressive testing. Thus, St. Peter Sandstone specimens cannot be obtained easily for laboratory testing (Schwartz, 1936; Payne, 1967; Petersen, 1978; Bagherieh, 2015) or in-situ testing (Yardley, 1978).

Baghereih, (2015) prepared 95 specimens of various sizes. Like Petersen (1978), Baghereih (2015) proposed an optimum specimen size of 51 square millimeters as a critical size for uniaxial compressive strength test. However, the 95 specimens had an aspect ratio of approximately one. Specimens of the same aspect ratio allow a researcher to characterize only size effect. Specimens for extensive strength characterization for the purpose of pillar design, are required to be in different shapes and sizes.

2.3.3. Uniaxial Compressive Strength Results. Numerous investigators (Schwartz, 1939; Payne, 1967, Yardley, 1978, Sterling, 1978, Petersen, 1978, Dittes and Labuz, 2002, Dittes, 2015, and Baghereih, 2015) have reported the uniaxial compressive strength of St. Peter Sandstone.

Schwartz (1939) conducted uniaxial compressive strength test on two dry specimens and one wet specimen. The UCS reported for the dry and wet specimens were 0.0038 MPa and 0.0073 MPa. The UCS results for the dry specimens was about 1 MPa. The UCS for the dry specimen was 1.53 MPa. In 1958, the Corps of Engineers also conducted UCS test on St. Peter Sandstone for a site investigation of St. Anthony Fall Lower Lock and Dam (Payne, 1967). Table 2.4 shows the UCS results of their investigation as reported by Payne (1967).

In 1978, researchers at University of Minnesota conducted laboratory and in-situ compression tests on St. Peter Sandstone due to their interest in underground space developments. Yardley (1978) reported the laboratory test results (Table 2.5).

The in-situ uniaxial compressive strength results reported by Sterling (1978) are also given in Table 2.6. Petersen (1978) performed UCS tests on cubic St. Peter Sandstone specimens with specimen sizes ranging from 13 to 51 mm in length. He also performed UCS test on cylindrical specimens that were 51 mm and 305 mm in diameter. Table 2.7 shows Petersen's UCS test results. Dittes (2015) performed UCS tests on dry and intact cylindrical specimens with diameters of 55 to 100 mm. Dittes (2015) maintained an aspect ratio of 2:1 for all test specimens.

Dittes's UCS test results are given in Table 2.8. Baghereih (2015) conducted extensive UCS tests on cubic specimen sizes in the range of 12 to 102 mm. Table 2.9 shows Baghereih's test results.

Table 2.4. Uniaxial compressive strength results after Payne (1967)

Test No.	w (%)	UCS (MPa)	Remarks
1	14.6	5.86	Medium to low dry strength, fairly well cemented
2	10.4	9.45	High dry strength, hard at field moisture
3	13.2	6.83	Medium to low dry strength, fairly well cemented
4	9.4	14.48	High dry strength, hard at field moisture
5	3.8	4.67	Medium to low dry strength, hard at field moisture
6	5.0	6.83	Medium to low dry strength, hard at field moisture
7	5.3	16.34	High dry strength, hard at field moisture
8	10.1	13.86	High dry strength, hard at field moisture
9	10.1	19.45	High dry strength, hard at field moisture
10	6.4	14.28	High dry strength, hard at field moisture
11	3.5	6.48	High dry strength, hard at field moisture

Table 2.5. Uniaxial compressive strength results after Yardley (1978)

Size (mm)		Equivalent* Width (mm)	UCS (MPa)
Width	Length		
25	25	25	2.14
32	32	32	1.93
51	38	44	2.34
51	44	48	2.83, 3.03
64	38	48	3.31
60	51	49	3.93
64	51	55	3.86
57	51	57	3.72
64	51	54	3.52

* Equivalent width is the square root of the product of specimen width and length

These authors (Schwartz, 1939; Payne, 1967, Yardley, 1978, Sterling, 1978, Petersen, 1978, Dittes and Labuz, 2002, Dittes, 2015, and Baghereih, 2015) found show large variability in the uniaxial compressive strength results.

Payne (1967) and Baghereih (2015) found that the spatial variability in the strength values, is as a result of the friable nature of St. Peter Sandstone, specimen size, and specimen shape and particle structure of the St. Peter Sandstone.

Table 2.6. Uniaxial compressive strength results after Sterling (1978)

Test No	Size (mm)			Equivalent width (mm)	width/height ratio	UCS (MPa)
	Width	Depth	Height			
1	292	152	279	211	0.76	4.56
2	305	152	178	216	1.21	6.83
3	216	203	229	209	0.91	2.31
4	203	203	254	203	0.80	1.43
5	203	229	203	216	1.06	3.19
6	229	229	241	229	0.95	5.82
7	203	203	165	203	1.23	3.1
8	178	203	254	190	0.75	1.6
9	191	203	178	197	1.11	3.22
10	203	203	102	203	1.99	5.92

Table 2.7. Uniaxial compressive strength results after Petersen (1978)

Nominal Size (mm)	Specimen's shape	Individual UCS (MPa)	Mean (MPa)	Standard deviation (MPa)
13	Cube	1.03, 1.28, 1.38, 1.59, 2.00, 2.07, 2.28	1.66	0.46
25	Cube	1.45, 1.59, 1.59 , 1.79, 2.38	1.76	0.37
38	Cube	2.34, 2.48, 2.55, 2.55, 2.96, 3.03	2.65	0.28
51	Cube	3.38, 4.21, 4.76, 4.96	4.33	0.71
51	Cylinder	2.86 , 3.14, 3.48, 3.69, 3.96, 4.07, 4.31, 5.69, 6.69	4.21	0.52
305	Cylinder	3.59 3.79	3.69	0.15

This is because sample preparation techniques that minimize sample disturbance have not been established by the literature. In general, an ideal sampling technique will have no mechanical disturbance as disturbance can result in loss of strength of up to 10% (Skempton and Sowa, 1963; Ladd and Lambe, 1963, Noorany and Seed, 1965). Disturbances on St. Peter Sandstone due to sampling, transportation, storage, and sample preparation can significantly reduce its compressive strength.

Table 2.8. Uniaxial compressive strength results after Dittes (2015)

Test No.	Specimen diameter (mm)	Aspect ratio	UCS (MPa)
1	90.29	2:1	1.18
2	90.29	2:1	0.39
3	90.29	2:1	0.84
4	55.80	2:1	0.69
5	55.80	2:1	0.70
6	55.80	2:1	0.59
U-1	76.20	2:1	0.24

Table 2.9. Uniaxial compressive strength results after Baghereih (2015)

Nominal Size (mm)	Individual UCS Results (MPa)	Mean UCS (MPa)	Standard Deviation (MPa)
12	0.10 0.17 0.23 0.24 0.31 0.43 0.50 0.81 0.81 0.87 0.95 1.03 1.12 1.22 1.29 1.30 1.43 1.45 2.03 2.06 2.12 5.38	1.18	1.12
25	0.24 0.55 0.71 0.72 0.82 1.22 1.31 1.33 1.78 1.83 1.95 2.23 2.31 2.90 3.79 4.22 4.98 5.04 6.06 6.36 7.27 11.78	3.16	2.83
38	0.82 0.82 0.93 2.02 2.43 2.48 2.76 2.81 2.91 3.33 3.74 4.37 4.60 4.61 4.95 5.38 6.59 7.22 8.13 8.93 9.18 15.02	4.73	3.39
51	1.80 2.13 2.20 3.00 3.25 3.43 3.50 3.60 3.66 3.81 3.81 4.14 4.21 4.37 5.32 7.00 8.69 8.95 10.63 12.85 21.99 24.55	6.68	6.10
76	1.53 1.84 2.83 5.25 17.67	5.82	6.78
102	0.95 4.36	2.65	2.41

Regardless of the cause of the differences, the tests done by Baghereih (2015) at Missouri University of Science & Technology represent the best available data on St. Peter Sandstone at the Pattison Sand Mine. Consequently, the pillar design work in this dissertation relies more heavily on the results published by Baghereih (2015).

2.3.4. Size and Shape Effect of St. Peter Sandstone. Uniaxial compressive strength of St. Peter sandstone exhibits significant size or shape effects.

Size effect is defined as a decrease in compressive strength as the specimen size increases. Size effect may be due to structural defects (joints, fractures, faults, bedding planes, cleats, inclusions, etc.) in the rock mass. These structural defects control the behavior of the rock mass. The same aspect ratio is maintained when analyzing the effect of specimen size on UCS. Shape effect, on the other hand, refers to an increase in compressive strength as width to height (w/h) ratio increases. Shape effect is caused by the greater confinement generated within wider specimens.

Bieniawski (1968) carried out UCS test on cubic coal specimens and showed that the UCS of coal decreased with increasing specimen size until after a specimen of 1 m, when the UCS was nearly constant. Nevertheless, Obert et al. (1946) reported no change in UCS with specimen size while significant UCS reductions with increasing specimen size have been reported for iron ore (Jahns, 1966), diorite (Pratt et al., 1972), sandstone (John, 1972), limestone, marble, basalt, gabbro, and granite (Hoek and Brown, 1980). Hoek and Brown (1980) compiled UCS results for several igneous and metamorphic rocks (except limestone, which is sedimentary) and concluded that UCS decreases with increasing specimen size (Figure 2.13). Hawkins (1998) performed uniaxial compressive tests on sedimentary rocks and observed that the maximum compressive strength was obtained from specimens cores of about 40-60 mm in diameter while lower compressive strength values were measured for both smaller and larger diameter core specimens. He concluded that typical size effect trend for most sedimentary rocks is as shown in Figure 2.14. This finding also concludes that Figure 2.13 is not applicable to all rocks, as most of the strength data were from igneous and metamorphic rocks (Tuncay and Hasencebi, 2009).

Yardley (1978) carried out UCS test on St. Peter Sandstone cubic specimens (Figure 2.15) and observed that the UCS increases with increasing specimen size. However, Petersen (1978) and Bagherieh (2015) reported that the UCS of St. Peter Sandstone increased with increasing specimen size but after specimen size of 51 mm the UCS decreases with increasing size (Figures 2.16 and 2.17). Petersen (1978) and Bagherieh (2015) UCS test results conclude that the maximum compressive strength for

St. Peter Sandstone occurs when specimens size is about 51 mm in length or 51 mm in core diameter while lower compressive strength values were measured for both smaller and larger specimen sizes. Lower UCS values for specimen size less than 51 mm in length is due to sample disturbance. Lower UCS values for specimen sizes greater than 51 mm in length is due to structural defects. The general trend is, however, consistent with the UCS test results conducted by Hawkins (1998). Thus, the effect of specimen size on strength for St. Peter Sandstone is consistent with that proposed by Hawkins (1998) for sedimentary rocks.

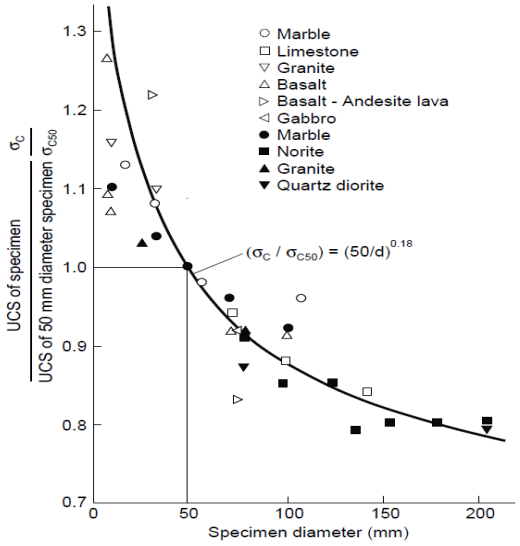

Figure 2.13. Effect of UCS on specimen size after Brown (1981)

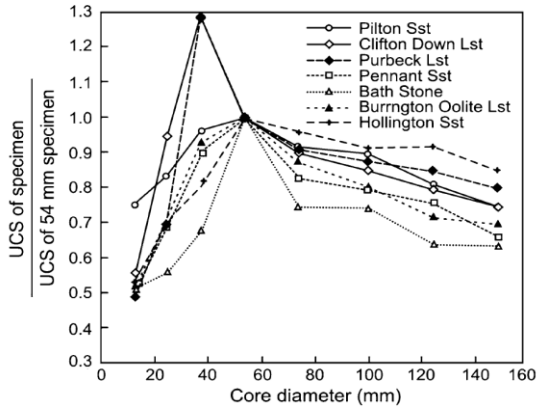

Figure 2.14. Effect of UCS on specimen size for sedimentary rocks after Hawkins (1998)

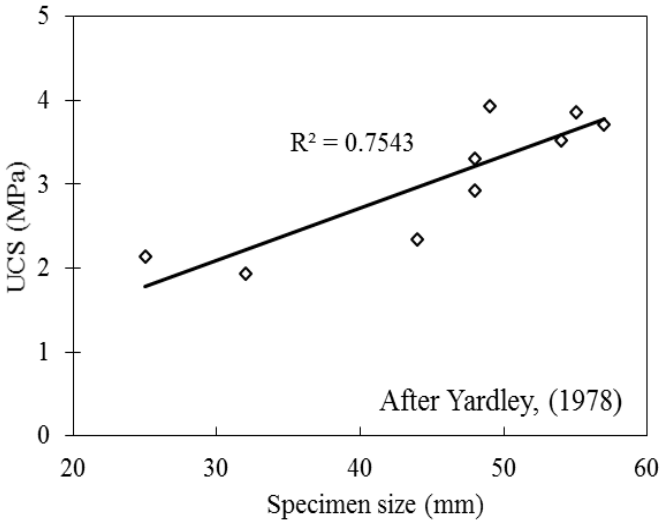

Figure 2.15. Average UCS variation with size after Yardley (1978)

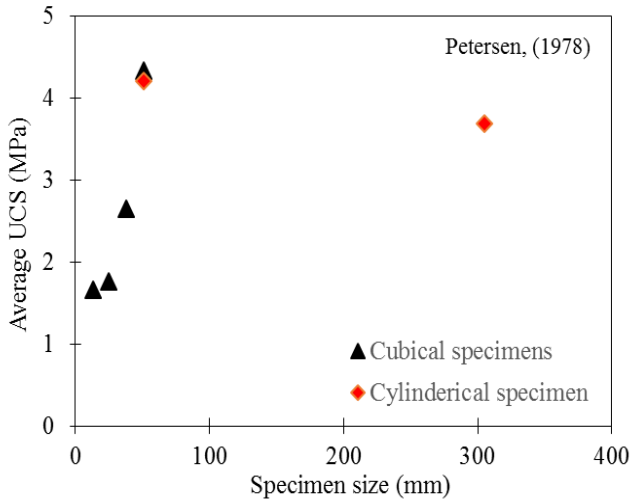

Figure 2.16. Average UCS variation with specimen size after Petersen (1978)

Payne (1967) studied the effect of moisture content on UCS. From his results (Figure 2.18), UCS increases with increasing moisture content until, at a moisture content of 10%, the strength decreases as moisture content increases. Dittes (2015) studied the effect of specimen diameter on UCS of St. Peter Sandstone but that study was very limited because of limited experiments (Figure 2.19).

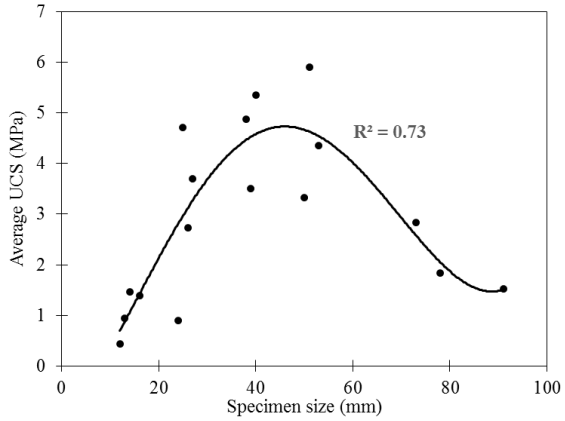

Figure 2.17. Average UCS variation with specimen size

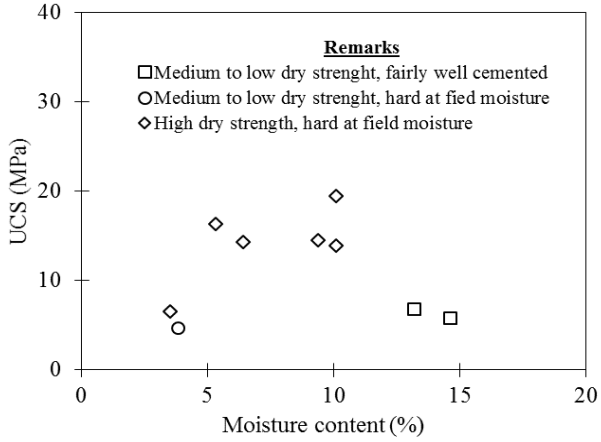

Figure 2.18. Average UCS variation with moisture content after Payne (1967)

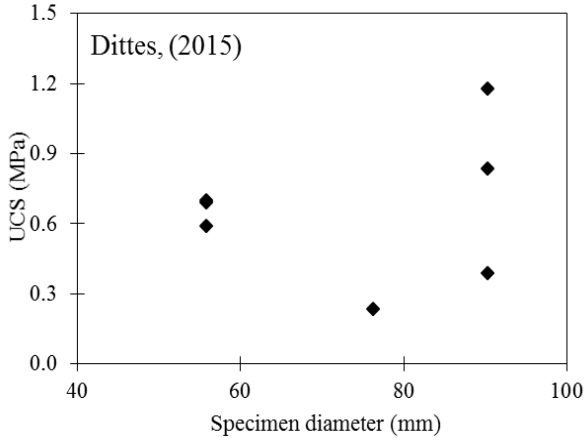

Figure 2.19. Average UCS variation with specimen size after Dittes (2015)

Sterling (1978) studied the effect of specimen shape on UCS of St. Peter Sandstone. Sterling's test results (Figure 2.20) show that increasing width-to-height (w/h) ratio increases UCS. Till date, shape effect investigations for St. Peter Sandstone have been very limited (Sterling, 1978, Baghereih, 2015).

Thus, the most challenging issue for anyone trying to apply empirical pillar design criteria for St. Peter Sandstone is that it is difficult to scale-up laboratory and in-situ strength values due to material variability, sampling effects, specimen preparation and testing, and size and shape effects (Payne, 1967; Yardley, 1977; Petersen, 1978; Sterling, 1978; Baghereih, 2015; Dittes, 2015). All these issues may be related to inhomogeneity of the St. Peter Sandstone structure (Baghereih, 2015).

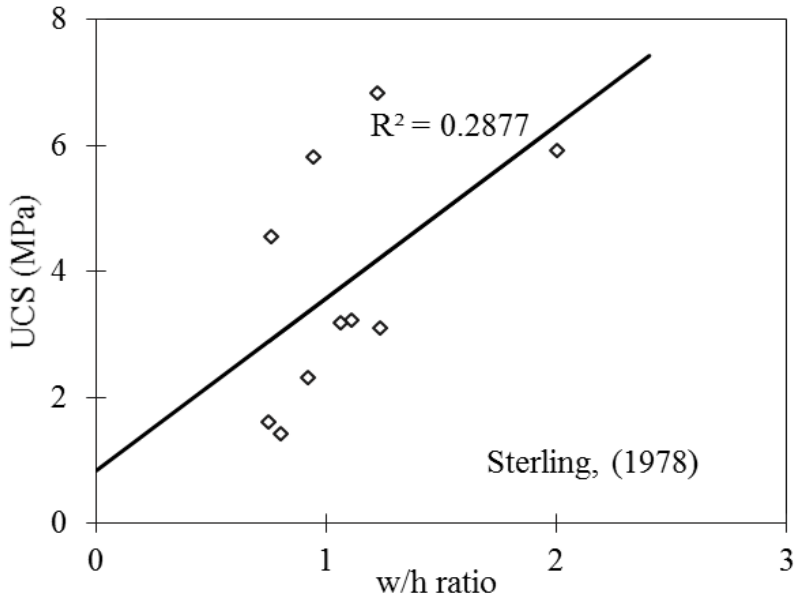

Figure 2.20. Average UCS variation with specimen size after Sterling (1978)

2.3.5. Uniaxial Compressive Strength of Cemented St. Peter Sandstone.

Various investigators (Schwartz, 1936; Payne, 1967; Dusseault and Morgenstern, 1979, Petersen, 1978; Baghereih, 2015) have reported that St. Peter Sandstone is cohesionless. However, the Baghereih (2015) reported that the upper part the St. Peter Sandstone shows varying degrees of cementation. Scanning Electron Microscope (SEM) conducted

by Baghereieh (2015) clearly distinguished uncemented St. Peter Sandstone from the cemented St. Peter Sandstone (Figure 2.21). According to Baghereieh (2015), Figure 2.21 showed SEM images of uncemented and cemented St. Peter Sandstone. Baghereieh (2015) reported that while Figure 2.21a shows no cementation, Figure 2.21b, on the other hand, shows a higher degree of cementation.

Baghereieh (2015) obtained cemented St. Peter Sandstone from Pattison Sand Mine. Figure 2.22a shows an uncemented sample while Figures 2.22b to 2.22f show five cemented samples collected from the mine site. Baghereieh (2015) prepared cylindrical specimens of the cemented St. Peter sandstone for uniaxial and tensile compression tests, respectively (Figure 2.23). The results of the UCS and tensile strength tests are given in Tables 3.12 and 3.13, respectively. The UCS of the cemented St. Peter Sandstone is within the range of 14 to 124 MPa.

(a)

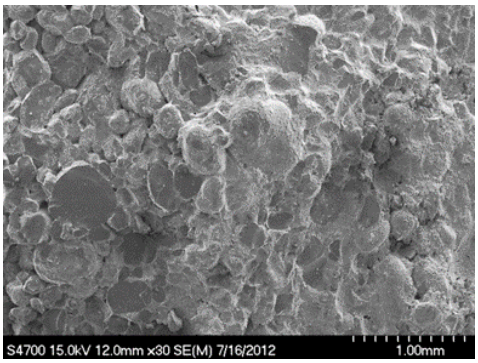

(b)

Figure 2.21. Scan electron microscope images of: (a) uncemented St. Peter Sandstone; (b) cemented St. Peter Sandstone after Baghereieh (2015)

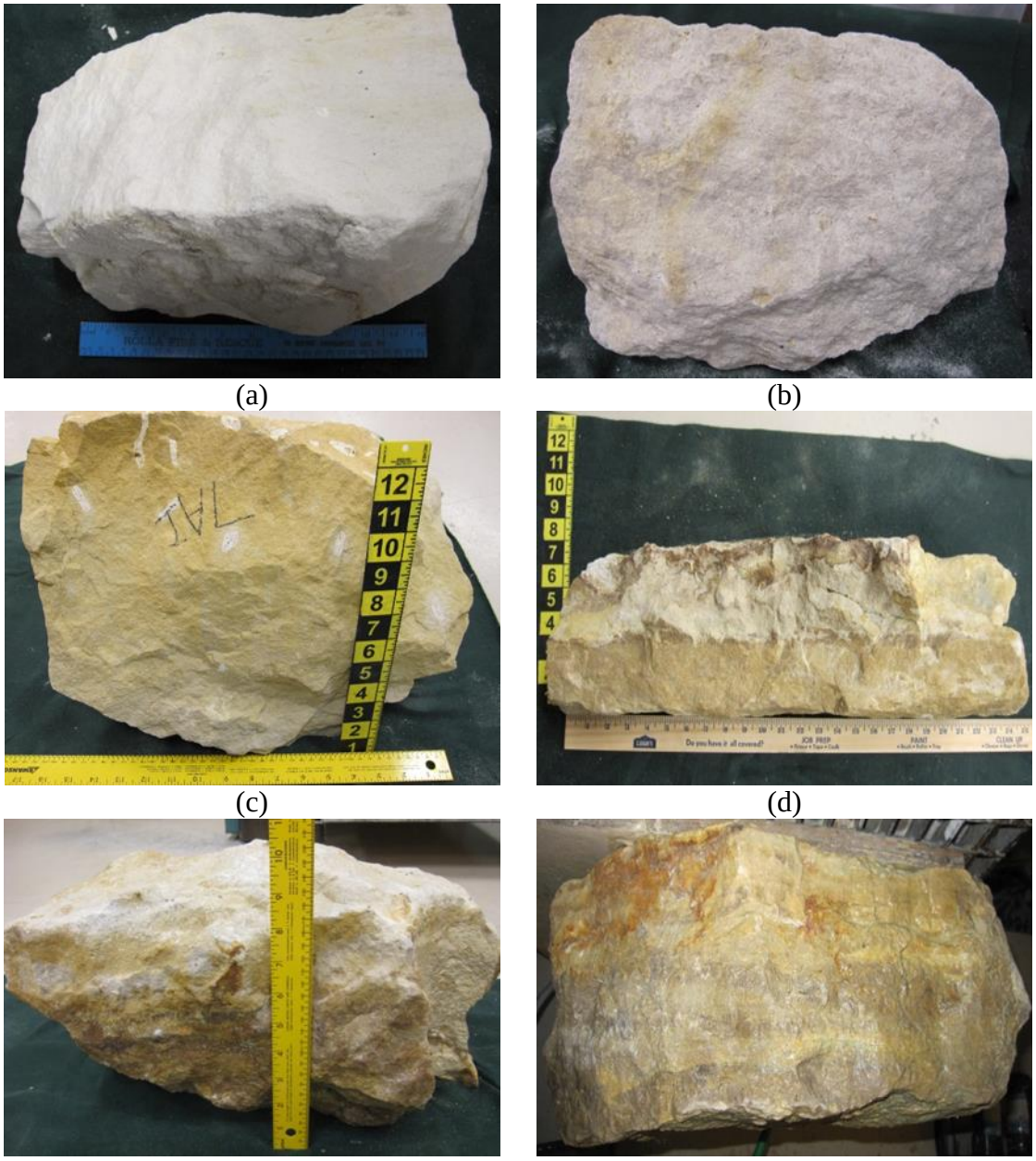

Figure 2.22. Images of St. Peter Sandstone samples: (a) uncemented; (b) -(f) cemented

2.4. TRIAXIAL COMPRESSION TESTING ON ST. PETER SANDSTONE

Triaxial compression test is a more versatile test than other shear strength tests. In this test, drainage can be controlled quite well. There is no rotation of σ_1 and σ_3. In triaxial tests, the failure plane can occur anywhere.

Figure 2.23. Specimens of cemented St. Peter Sandstone

Table 2.10. UCS for cemented St. Peter Sandstone after (Bagherieh, 2015)

Sample ID.	# of specimens	Average UCS (MPa)	Standard Deviation (MPa)
BK4	4	18.89	3.20
7AI-2	5	28.21	6.20
BK5	4	42.09	6.99
En	6	59.89	13.88
BK1	6	95.23	21.39

Table 2.11. Indirect tensile strength for cemented St. Peter Sandstone (Bagherieh, 2015)

Sample ID	# of specimens	Average UCS (MPa)	Standard Deviation (MPa)
7AI-2	6	2.46	1.14
BK5	5	3.61	1.12
En	8	4.78	2.15
Bk1	7	6.94	1.92

Also, stress paths to failure can be controlled by the researcher. In triaxial tests, complex stress paths in the field can be more effectively modeled in the laboratory (Holt et al, 2009). In triaxial compression test, the specimen is subjected to confining pressures

and a compressive load is applied in the vertical direction (Figure 2.24). The results of triaxial tests can be used to draw Mohr-Circles. A failure envelope is fitted to the Mohr-Circles. The failure envelope can show basic shear strength parameters (mainly friction angle and cohesion).

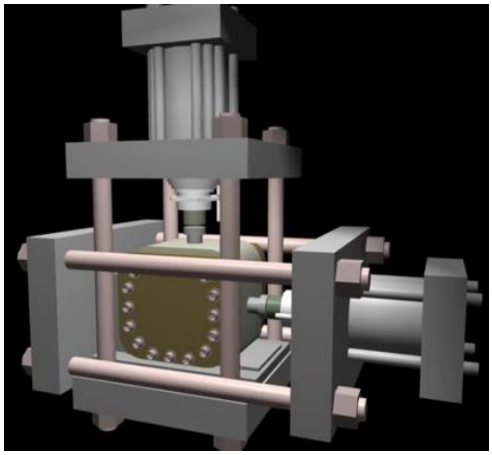

(a)

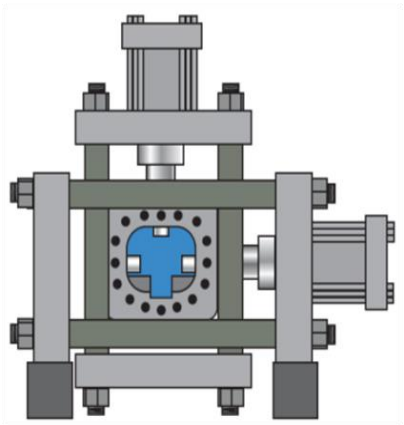

(b)

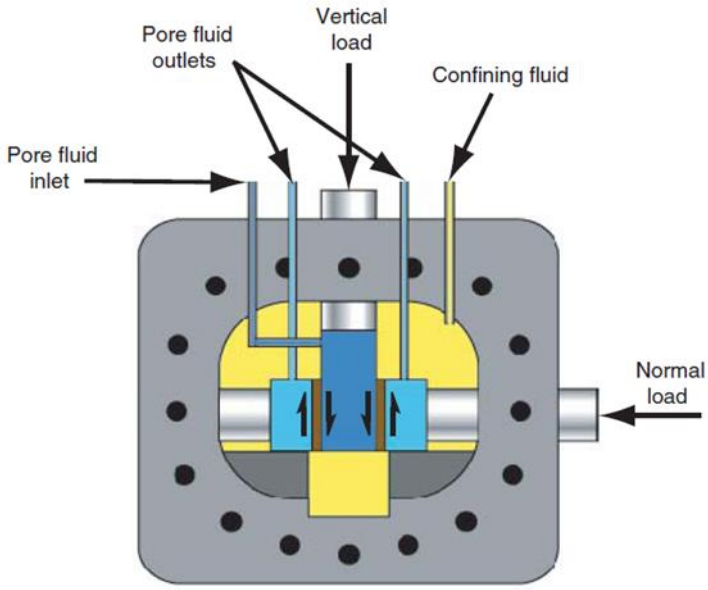

(c)

Figure 2.24. (a) Three-dimensional illustration of true-triaxial pressure vessel and biaxial load frame b) two-dimensional illustration of true-triaxial pressure vessel and biaxial load frame c) the cross section of pressure vessel (Bagherieh, 2015)

The shear strength failure envelope can be expressed as a function of confining pressure. Triaxial test helps to elucidate the mechanical behavior of rocks or soils (Bagherieh, 2015; Mishra and Janeček, 2017).

Watson (1938) is among the first researchers to carry out a triaxial compression test on densely packed and loosely packed St. Peter Sandstone specimens at Twin City Minnesota. Watson's results revealed friction angles of 42º and 33º for the densely and loosely packed St. Peter sands, respectively. Also, Watson (1938) carried out a triaxial test on eight (8) undisturbed St. Peter Sandstone specimens. His results revealed a friction angle of 60º and lack of cohesion (Figure 2.25). Labuz et al (1998) conducted triaxial tests on intact St. Peter Sandstone specimens (Figure 2.26) and obtained a friction angle of 63º. Dittes and Labuz (2002) performed in-situ pressuremeter tests on wet St. Peter Sandstone.

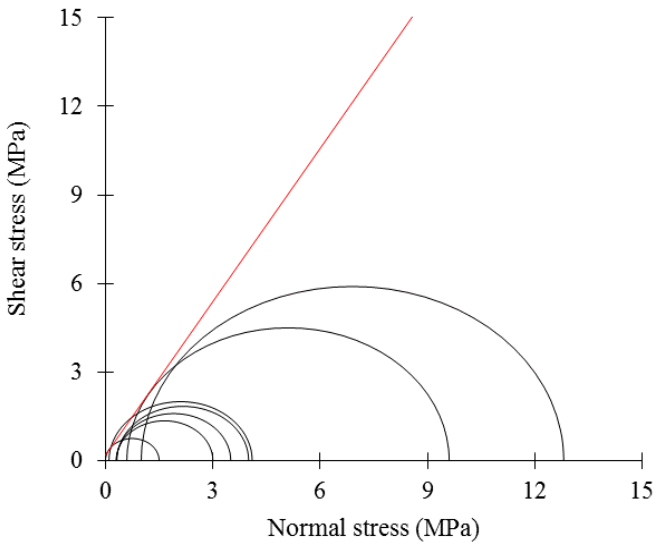

Figure 2.25. Mohr envelope of St. Peter Sandstone (Watson, 1938)

Their friction angles were within the range measured in the laboratory. Triaxial test results conducted by Dusseault and Morgenstern (1979) revealed a friction angle of 63º. Dusseault and Morgenstern (1979) and Dittes and Labuz (2002) used the direct shear test to determine the friction angle of St. Peter Sandstone.

The direct shear test results reported by Dittes and Labuz (2002) revealed a friction angle of 57º, while Dusseault and Morgenstern (1979) reported about 67º.

Baghereih (2015) reported results of triaxial compressive strength tests conducted by the author's research group. Baghereih (2015) prepared cubic specimens in a way similar to the sample preparation procedure discussed above. Figure 2.27 show cubic or rectangular specimens used for triaxial compression tests. A major challenge was that the design of the testing machine is for cylindrical specimens. However, the specimens used for the triaxial tests were mainly cubic or rectangular in shape. This challenge can be overcome by using triaxial testing machines that accommodate cubic specimens, such as that used by Minaeian (2014). The specimen dimensions and test results of the specimens presented in Figure 2.27 are given in Table 2.12.

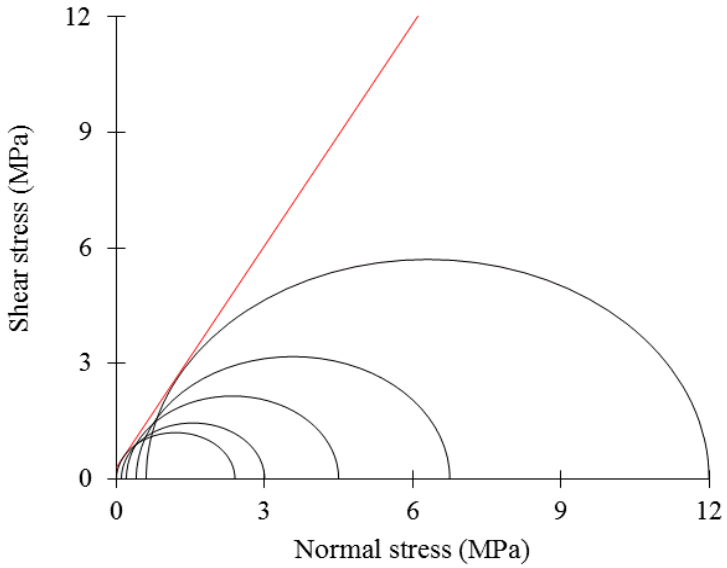

Figure 2.26. Mohr envelope of St. Peter Sandstone (Labuz et al., 1998)

The test equipment captures the stress-strain responses of St. Peter Sandstone under triaxial testing condition during the tests. The numbers on the stress-strain curves indicate the applied confining pressure. No confining pressure, indicated as zero (0), on the stress-strain curve represent uniaxial compressive testing condition.

(a) 1S specimens

(b) 6AR specimens

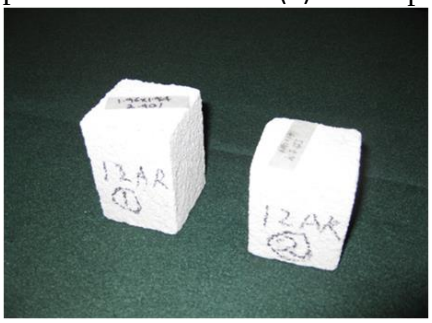

(c) 12 AR specimens

Figure 2.27. Specimens utilized for the triaxial test

Table 2.12. Confining stresses and axial stresses at failure

Sample ID	Dimension (mm)	Confining Stress (MPa)	Axial Stress at failure (MPa)
1S-2	51×51×70	0.66	20.23
1S-1	51×51×81	2.06	25.76
1S-3	51×51×67	3.44	31.75
1S-4	47×48×50	6.87	41.50
1S-5	47×46×67	6.87	42.10
6AR-1	51×51×57	0.69	25.74
6AR-3	51×51×54	3.45	46.23
6AR-2	51×51×48	6.87	88.73
12AR-2	48×51×65	0.70	14.37
12AR-1*	50×50×74	6.88	------

*A jacket leak occurred in this experiment

The stress-strain response at zero confining pressure shows brittle behavior. However, as the confining pressure increases, the stress-strain responses show a ductile and strain softening behavior. In general, the stress–strain curves show an increase in strength as confining pressure increases. Figures 2.28a and 2.28b show typical stress-strain response for 6AR, and 1S, respectively. Other stress-strain response for St. Peter

Sandstone can be found elsewhere (Bagherieh, 2015, Dusseault, 1977). These stress-strain plots show that St. Peter Sandstone behaves as strain softening material. Bagherieh (2015) reported that the friction angle for St. Peter Sandstone range of 59^{o} to 70^{o}, with an average of 63^{o}. Figure 2.29 shows a Mohr envelope for 6AR.

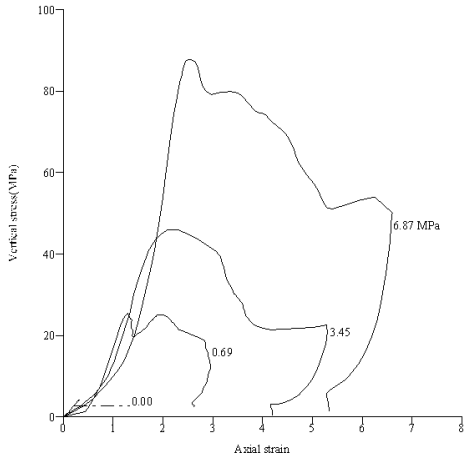

(a)

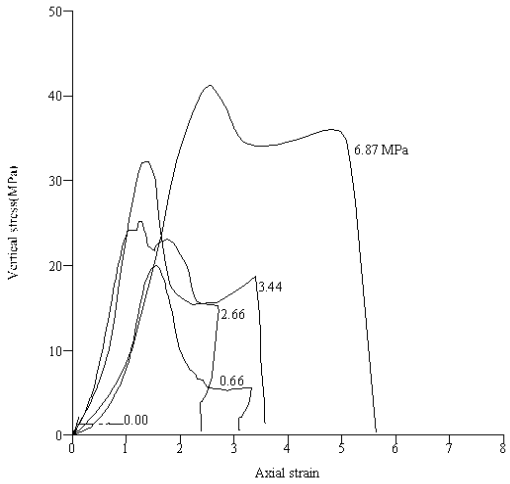

(b)

Figure 2.28. Axial stress-strain curves under different confining stresses for: (a) 6AR and (b) 1S samples

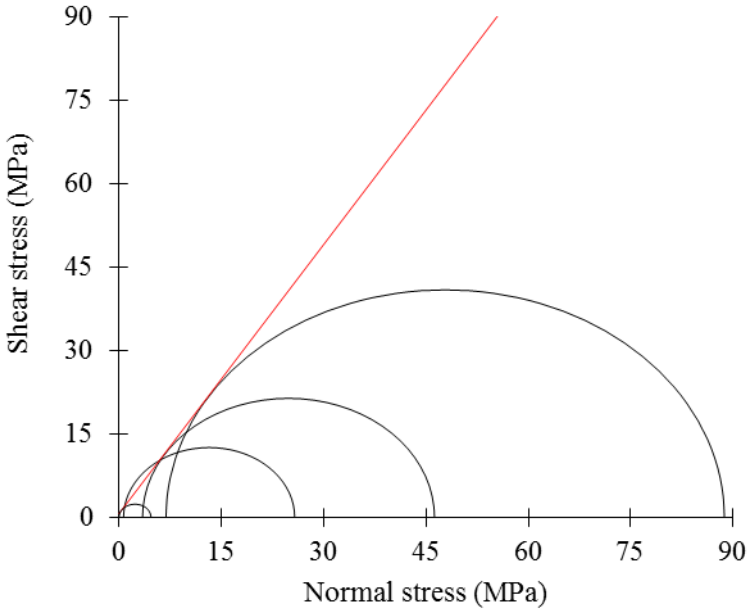

Figure 2.29. Mohr envelop for 6AR specimens

2.5. PILLAR DESIGN FOR ST. PETER SANDSTONE

In a typical room and pillar mine, pillars are required to support the overlying strata. Stable pillars and roof spans provide safe working conditions in room and pillar mines. Pillar design involves estimating the pillar stress, strength, and safety factors. The mining engineer then predicts an optimal pillar size that satisfies economic and safety constraints (Esterhuizen, 2007).

2.5.1. Pillar Stress. Pillar stress is the ratio of the overburden load to the pillar area. The overburden load imposed on a pillar is constant. However, the pillar area may change with time depending on factors such as the magnitude of the pillar load, weathering, geological discontinuities, pillar rock and surrounding strata strength properties. An engineer can estimate the pillar stress using empirical or numerical methods.

The tributary area method is the empirical approach mostly used to estimate pillar stress. The tributary area method assumes that the overburden weight is equally distributed (Brady and Brown, 1985). Also, the method assumes that the overburden load is applied perpendicular to the pillar area. For this reason, the tributary area method cannot be used to estimate the pillar stress of inclined pillars. Other limitations of the

tributary area method are that it ignores: pillar stress distribution, deformation and failure characteristics of the roof-pillar strata, and the interaction between the roof and pillar strata (Jeremic, 1985). For this reason, the tributary area method predicts the upper limit of the average pillar stress (Esterhuizen et. al., 2011).

A researcher can use numerical methods to estimate pillar stress. For example, Mark (1987) used two-dimensional finite element model to determine the accuracy of the tributary area method's prediction of pillar stress. Mark's model predicted average pillar stresses that were 2-8% less than the tributary area predictions. However, Esterhuizen et. al. (2011) found that the tributary area method predicts the upper limit of the average pillar stress. Thus for practical design purposes, Equation (2) can be used to estimate the pillar stress.

$$\sigma_P = 0.025H\,\frac{(w+l)^2}{w^2} \tag{2}$$

Where w is the pillar width, l is the entry width and H is the overburden depth. w, l , and H are in meters.

2.5.2. Pillar Strength. Brady and Brown (1985) defined pillar strength as the maximum load-bearing capacity of the pillar to axial compression. Realistic estimation of the load-bearing capacity of pillars is very challenging. Researchers have resorted to using empirical, analytical and numerical methods to estimate pillar strength.

2.5.2.1 Empirical methods. Empirical methods are widely used to estimate pillar strength because it is easy to use and relies on scientific interpretation of real mining experience (Mark, 1999). Pillar designers derived empirical pillar strength formulas from laboratory tests, in-situ tests, and back calculation.

A researcher can derive empirical pillar strength formulas by extrapolating the results of laboratory tests on rock specimens to full-sized pillars used in mines. This approach applies the concept of critical size proposed by Bieniawski (1968). Bieniawski (1968) defined critical size as the specimen size at which even with an increase in specimen size, the strength remains constant. Bieniawski (1968) proposed that the strength value at critical size is directly applicable to full-sized pillars. Several

researchers have used this approach to derive empirical pillar strength equations for coal (Holland and Gaddy, 1957; Obert and Duval, 1967). Petersen (1978) also used this approach to estimate the pillar strength for St. Peter Sandstone pillars at the St. Paul/Minneapolis area. A major limitation for the application of this approach to St. Peter Sandstone is that it does not fully account for shape and size effects. On one hand, the general trend for the effect of specimen size on strength is not applicable to St. Peter Sandstone (Petersen, 1978). On the other hand, to the best of this researcher's knowledge, no laboratory test has been conducted to characterize the influence of specimen shape on the uniaxial compressive strength of St. Peter Sandstone. Consequently, Petersen's empirical pillar strength formulas derived by extrapolating the results of laboratory tests to full-sized pillar are not adequate.

The researcher made an effort to estimate pillar strength of stable St. Peter Sandstone pillars at an abandoned St. Peter Sandstone mine. The ages of these pillars were from 35 to 72 years. This researcher computed the safety factor (pillar strength divided by pillar stress) to ascertain if these pillars are stable. Figure 2.30 shows estimates of safety factors for stable pillars at the abandoned St. Peter Sandstone mine. It is obvious that the safety factors given in Figure 2.34 are less than one. Safety factors less than one indicates that the pillar is unstable or failed. However, this is not consistent with field observations. Hence, the researcher concluded that Petersen's empirical pillar strength is inadequate to estimate the pillar strength of pillar cases in the study area.

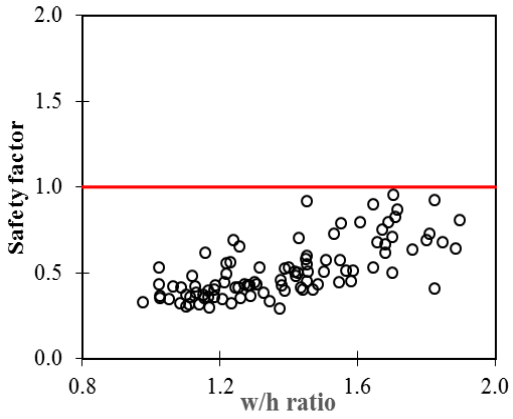

Figure 2.30. Safety factor against w/h ratio using Petersen's empirical model

Empirical pillar strength formulas can also be derived by back calculation. In this approach, the researcher collects data on observed failed and stable pillars. The researcher then fit a pillar strength curve to the observed failed and stable pillars case history data. For example, Salamon and Munro (1967) and Mark (1999) used this technique to determine the pillar strength for coal. Hedley and Grant (1972) and Pritchard and Hedley (1993) also employed this approach to derive a pillar strength formula for hard rocks. Nevertheless, Peterson's attempts to apply this approach to estimate the strength of St. Peter Sandstone was not possible, owing to little room and pillar underground developments at that time (Petersen, 1978). Currently, there are numerous room and pillar case histories from which a researcher could, in theory, derive an empirical pillar design method based on this approach, yet no work has been conducted in this area. The use of this empirical approach requires failed and stable pillar case histories. Perhaps, this is because this researcher could not find a failed St. Peter Sandstone pillar case nor has there been any report of one in literature. Consequently, this researcher attempts to derive pillar strength equation based on the back-calculation approach was not possible.

Another empirical approach involves scaling uniaxial compressive strength of intact pillar rock material to estimate the strength of a pillar. Various researchers have used different scale-effects for different rock masses (Table 2.13): 58% for quartzite rock (Hedley and Grant, (1972), 69% for metasediments (Von Kimmelmann et al., 1984), 35.4 % for limestone (Krauland and Soder, 1987), 42% for Canadian Shield (Potvin et al., 1989), 31% for limestone (Sjoberg, 1972), and 42% for hard rocks (Lunder and Pakalnis, 1997). This researcher attempted to establish the efficacy of using the scale-effect of the uniaxial compressive strength of St. Peter Sandstone to estimate pillar stability. Using an average uniaxial compressive strength of 4.5 MPa (Figure 2.17), he computed the safety factors of the pillar cases at the CGB Mine in Clayton, Iowa. The effect of down-scaling the uniaxial compressive strength on the stability of St. Peter Sandstone pillars is shown in Figure 2.31. The reader can see that even at a uniaxial compressive strength of 7.2 MPa, some of the pillars had safety factors less than one.

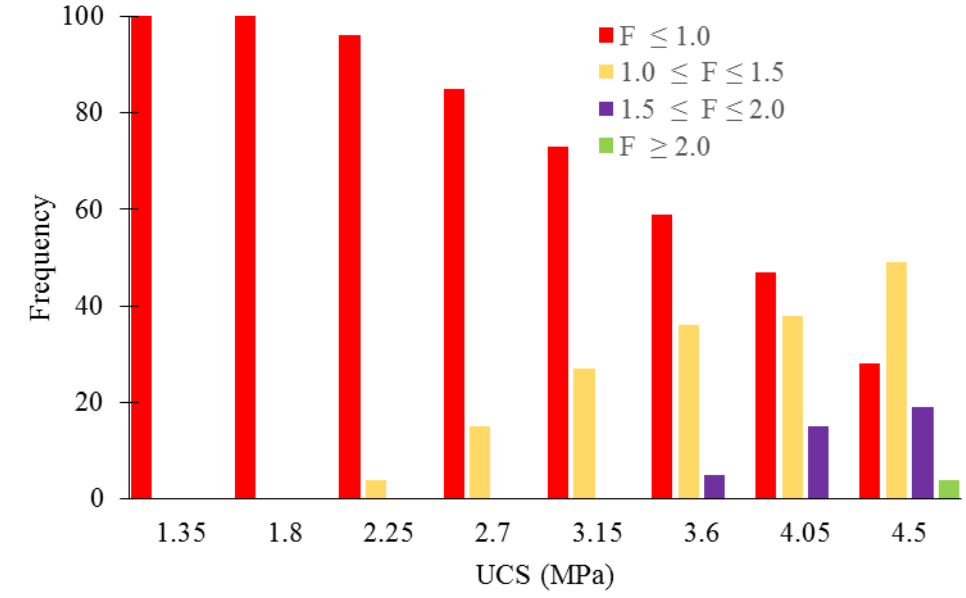

(a)

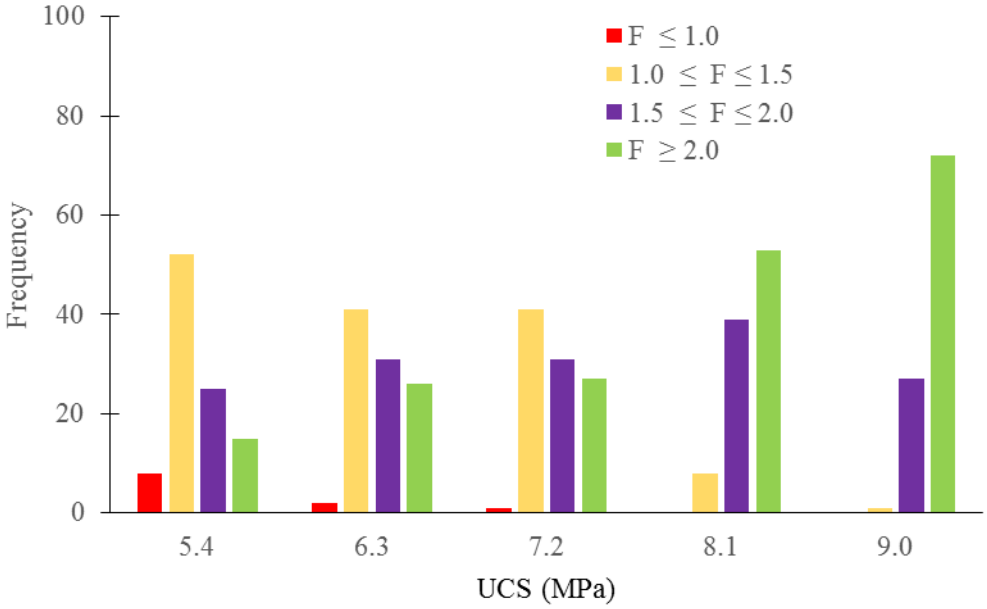

(b)

Figure 2.31. Effect of UCS on safety factor of pillar cases in Iowa

Thus, the most challenging issue for deriving empirical design for St. Peter Sandstone is that scaling intact strength is difficult due to material variability and effects of sampling, specimen preparation and testing, size and shape effect (Payne, 1967; Petersen, 1978, Bagherieh, 2015; Dittes, 2015).

Table 2.13. Empirical strength formula for hard rock pillars

Authors	Pillar strength	σ_c (MPa)	Rock mass
Hedley and Grant, (1972)	$133\frac{w^{0.5}}{h^{0.75}}$	230	Quartzite
Von Kimmelmann et al., (1984)	$65\frac{w^{0.46}}{h^{0.66}}$	94	Metasediments
Krauland and Soder, (1987	$35.4\left(0.778+0.222\frac{w}{h}\right)$	100	Limestone
Potvin et al., (1989)	$0.42\ \sigma_c\frac{w}{h}$	-	Canadian Shield
Sjoberg, (1972)	$74\left(0.778+0.222\frac{w}{h}\right)$	240	Limestone
Lunder and Pakalnis, (1997)	$0.42\ \sigma_c(\ 0.68+0.52k)$	-	Hard rocks

2.5.2.2 Analytical approach. Wilson (1972) developed an analytical pillar design approach, which is widely used by the mining industry. Wilson's pillar strength Equation is given by:

$$\sigma_p = 4\rho h(p^3 - 0.003pmh + 0.000003m^2h^3)tons \quad (3)$$

$$\sigma_p = 4\rho h(pl - 0.015(p+l)mh + 0.000003m^2h^2)tons \quad (4)$$

Where ρ is the density of the rock in ton/ft^3, h is the depth of cover in feet, p is the width of the pillar in feet, l is the length of a pillar in feet and m is the pillar height in feet. According to Wilson, Equation (3) and (4) respectively, can be used to estimate the pillar strength for squared and rectangular pillars. This researcher used Equations 2.2 and 2.3 to estimate the pillar strength of St. Peter Sandstone. He concluded that the pillar strength estimated using Wilson equations underestimate the pillar strength for St. Peter Sandstone as many of the pillars resulted in safety factors less than one (Figure 2.32). Hence, the analytical pillar strength widely used by the mining industry cannot be used to estimate the pillar strength of St. Peter Sandstone.

Wilson (1972) defined pillar strength as the numerical integration of the pillar stress distribution divided the pillar area. Wilson's estimated pillar strength is based on

the pillar stress distribution at the pillar midheight. To the best of the researcher's knowledge, no attempt has previously been conducted to estimate pillar strength using pillar stress distribution. In this study, the researcher seeks to estimate pillar strength of St. Peter Sandstone using the pillar stress distribution at the pillar midheight using numerical methods.

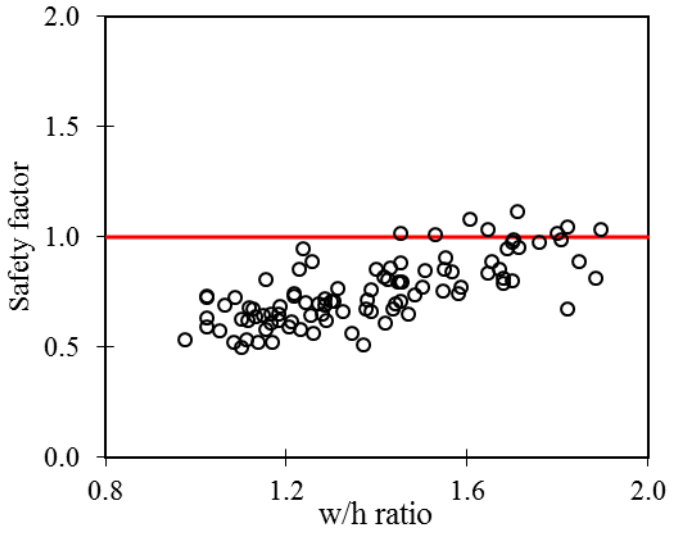

Figure 2.32. Safety factor against w/h ratio using Wilson equations

Wilson (1972) postulated that a pillar is grouped into two zones: a central inner core subjected to triaxial stress conditions and surrounded by a yield zone, which protects the inner core. According to Wilson, the stress at the pillar rib is relatively low and suffer little constraints. As one moves from the pillar rib towards the center of the pillar, the stress gradually increases until it reaches a peak value. Thus, the yield zone according to Wilson is the horizontal extent from the pillar rib to the peak stress. The pillar rock between the pillar rib and peak stress is broken and flows towards the roadway. The yield zone surrounds the inner core. Hence, the inner core remains undisturbed. Figure 2.33 shows the pillar stress distribution at the midheight of a pillar and illustrates the yield zone and pillar core. However, Wilson's pillar stress distribution fails to fully elucidate the effect of the mechanics of friction angle and cohesion on pillar stress distribution.

According to Wilson (1972), the shape of the pillar stress distribution shows whether a pillar is stable (Figure 2.34a), approaching its load-bearing capacity (Figure 2.34b) or ultimate loading capacity or pillar failure (Figure 2.34c). As a result, pillar designers can use the shape of the pillar stress distribution profile to determine whether the pillar strength equation is conservative or overly conservative, underestimated or overestimated. A major criticism of Wilson's work is that he did not relate the pillar stress distribution to the average pillar stress. Consequently, it is difficult for an engineer to relate the behavior of the pillar stress distribution to the average pillar stress. This study will attempt to relate the pillar stress distribution to the average pillar stress.

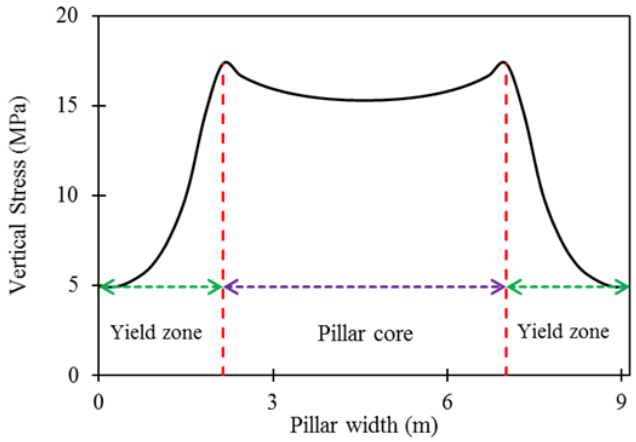

Figure 2.33. Pillar stress distribution showing yield zone and pillar core

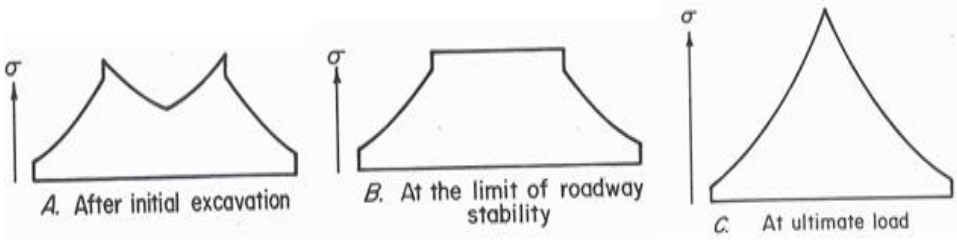

Figure 2.34. Stress distribution profiles for (a) stable pillar (b) limit of roadway stability and (c) ultimate load capacity (Mark, 1987)

2.5.2.3 Numerical methods. Numerical modeling has found increasing application in pillar design. Hoek and Brown (1980) used an elastic model to estimate pillar strength for various rock masses. Several researchers have also employed numerical methods to estimate pillar strength for hard rocks (Lunder and Pakalnis, 1997; Esterhuizen, 2007; Mortazavi et al., 2009; Martin and Maybee, 2000; Arthur et. al., 2016). Esterhuizen et al. (2010), Esterhuizen and Mark (2009), Jaiswal and Shrivastva, (2009), Mohan and Sheorey (2001), Wang et al. (2011), Fahrman (2016) and many others have used numerical models for pillar design for coal. Despite the numerous applications of numerical models in pillar design, however, numerical models have previously never been used to predict pillar strength of St. Peter Sandstone. This study will attempt to use numerical modeling to: estimate the strength of St. Peter Sandstone pillar reveal factors that affect pillar strength modeling, and elucidate possible causes of pinch put failures. This is the first time these numerical modeling and analysis will be conducted on St. Peter Sandstone pillars. These analyses are expected to advance the research frontier in pillar design and ground control for St. Peter Sandstone.

An investigator can use three techniques to solve field problems. These methods are experimental, analytical and numerical. The experimental approach is expensive, time-consuming and cumbersome and usually does not allow much flexibility in parameter variations. Analytical or classical methods are: rigorous; mathematical solutions are exact; and the controlling parameters (geometry and material) can be varied. The advantage of the analytical method is that it can solve simple geometry of a domain. The major limitation of the analytical methods lies on the fact that it cannot deal with complex geometries and material heterogeneity.

Numerical methods take advantage of computing capabilities and provide greater flexibility in solving complex problems while handling complex geometries and material heterogeneity with ease. The most used numerical methods are finite element methods, finite difference methods, and boundary element methods. Finite difference method uses the differential form of the governing partial differential equations while the finite element and boundary element methods are based on their integral form and require solving a global system of equation systems. In this study, the researcher used finite difference method in modeling pillar, roof and floor strata. In particular, this researcher

used the Fast Lagrangian Analysis of Continua in three- dimensions (FLAC3D), an explicit finite difference software manufactured by Itasca Consulting Group of USA. FLAC3D is well established for engineering mechanics computations. FLAC3D is capable of simulating the behavior of three-dimensional problems in geotechnical engineering. For this reason, the principal researcher investigator purchased FLAC3D for this study.

2.6. SUMMARY

The St. Peter Sandstone is a homogenous stratified arenaceous clastic sedimentary rock of middle Ordovician age. The formation covers more than 576,000 km^2 of Middle North America. St. Peter Sandstone was initially recognized in Missouri, Iowa, Minnesota, Illinois, Arkansas, southern Wisconsin, Kansas, Indiana, Tennessee, Kentucky, Arkansas, Oklahoma, South Dakota, Nebraska, Michigan, and Ohio. Stratigraphic correlation of St Peter Sandstone and adjacent formations have found equivalence in Missouri, Iowa, Minnesota, Illinois, Arkansas, and other Mississippi Valley states. The thickness of St Peter Sandstone is not uniform and is due to erosional channels and karstic terrains underlying carbonate rocks.

St. Peter Sandstone comprises of two members (Tonti and Starved) based on the grain size, type, and sequence of sedimentary structures. The Tonti Member is the finer grained member while the Starved member is a medium to coarse-grained one. St. Peter Sandstone may have been deposited by eolian or fluvial actions.

St. Peter Sandstone is characterized as locked sands having: no cohesion, highly quartzose mineralogy, high strength, steeply curved failure envelopes, low porosity, considerable age, lack of interstitial cement, brittle behavior, residual shear strengths of 30o-35o, and extremely large dilation rates at failure. It is considered as a very dense sand with a relative density of 100 to 135%. The porosity of St. Peter Sandstone is within the range of 19 to 30%.

Locked sands require careful sampling and specimen preparation efforts to produce undisturbed yet high-quality specimens. The quality of the sample is then a key factor in any estimate of St. Peter Sandstone’s strength. The uniaxial compressive

strength of St. Peter Sandstone varies from the range of 0.1 to 24.55 MPa, with the standard deviation being almost to the mean (Bagherieh, 2015).

Pillar design criteria for mining excavations are derived using empirical, analytical or numerical methods. No pillar design method exists for St. Peter Sandstone. Deriving empirical design equations for St. Peter Sandstone challenging because scaling intact strength is difficult due to material variability, effects during sampling, specimen preparation and testing, size and shape effect (Payne, 1967; Petersen, 1978, Bagherieh, 2015; Dittes, 2015). Petersen, (1978) empirical pillar strength model, which is widely used in the mining industry, is inadequate to estimate the strength of St. Peter Sandstone pillars.

Wilson, (1972) analytical pillar strength equations model, which is widely used by the mining industry, is inadequate for estimating the strength of St. Peter Sandstone pillars. To the best of this researcher's knowledge, no attempt has previously been made to estimate pillar strength using pillar stress distribution (analytical method). This study will seek to estimate pillar strength of St. Peter Sandstone using the pillar stress distribution at the pillar midheight. A major criticism of Wilson's work is that he did not relate the pillar stress distribution to the average pillar stress. Consequently, it is difficult for an engineer to relate the behavior of the pillar stress distribution to the average pillar stress. This study will attempt to relate the pillar stress distribution as a function of the average pillar stress.

Numerical methods have found increasing application in pillar design for coal and hard rocks. Despite the numerous application of numerical models in pillar design, however, numerical models have previously never been used to predict pillar strength of St. Peter Sandstone. Numerical methods, however, provide a viable path to: estimate the strength of St. Peter Sandstone pillar; reveal factors that affect pillar strength modeling; and elucidate possible causes of pinch out failures.

3. STUDY SITE AND EXPERIMENTAL CHARACTERIZATION

This Section presents study sites and experimental design techniques used in this study. Particularly, this section discusses: (i) study sites, (ii) geology of Pattison and CGB Mines, (iii) field investigations, (iv) ground control in St. Peter Sandstone mines, (v) stress change and roof displacement monitoring in St. Peter Sandstone mines.

3.1. STUDY SITE

A number of underground developments have been constructed in the St. Peter Sandstone. In particular, the room and pillar underground mining method has been used to exploit St. Peter Sandstone formation in Clayton, Iowa, Crystal City, Missouri, Guion, Arkansas, Pacific, Missouri, and St. Paul-Minneapolis, Minnesota. Room and pillar developments in Clayton, Iowa are the main study sites in this study.

The largest silica mine operation in St. Peter Sandstone in Iowa is located in Clayton, along the Mississippi River. From 1878 to 1929, the St. Peter Sandstone quarried from the river bluffs was used for glassmaking and foundry. The sand produced from a second St. Peter Sandstone quarrying operation was used as a feedstock for a brick and tile plant in the 1920s. In 1916, Langworthy Silica Company quarried the St. Peter Sandstone for foundry sand for John Deere Tractor Works. By 1945, the removal of the overburden material at Langworthy Silica Company was too expensive, hence, the company started using the room and pillar mining method. Typical room span was 12.19 meter square and 15.24 meter high. From 1945 to 1982, underground extraction was operated by Martin Marietta Corporation. Underground mining at this property stopped in 1982. After 1982, the mine was used for underground storage, typically corn, cottonseed, fishmeal, fertilizer, logs, coal, and tires. The Clayton silica sand mine was also used as a defense shelter, housing 44,000 people during the Cold War. In 1983, Pattison Sand Company, LLC purchased the mine and used for underground storage of fertilizers and other bulk commodities. In 2004, Pattison was approached by a former mine geologist to consider re-opening the silica sand mine. In 2005, they started mine development. In 2007, the mined area used for storage was sold to Consolidated Grain Barge (CGB). Since 2007, Pattison Sand Company has operated the Clayton silica mine. Underground

mining at Pattison Sand Mine was completed in 2016. Figure 3.1 shows the property boundaries of the room and pillar operations at CGB and Pattison Sand Mine.

The life of the pillars at CGB mine ranges from 35 to 72 years with an average of 54 years. The life of pillars at the Pattison Sand Mine ranges from about 1 to 10 years with an average of about 5 years. For the purpose of pillar design, Pattison Sand Company used the CGB mine site because it has a long history of pillar performances.

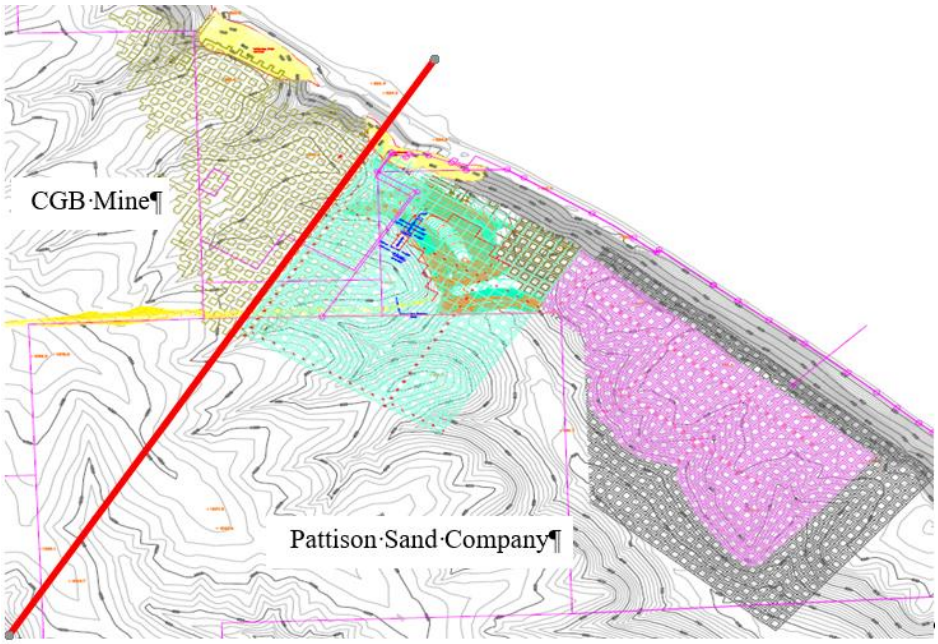

Figure 3.1. Property demarcation of CGB Mine and Pattison Sand Company. Red line shows property boundary between the two owners

3.2. GEOLOGY OF THE PATTISON SAND/CGB MINES

Pattison and CGB Mines are located at Clayton, Clayton County, Iowa. These mines are situated at the northeastern corner of Iowa. The St. Peter Sandstone at these mines are along the Mississippi River. The St. Peter Sandstone unconformably underlies the Oneota limestone. At these mines, the Platteville limestone overlies the St. Peter Sandstone. The general stratigraphic units at Pattison Sand and CGB mines are shown in Table 3.1.

The St. Peter Sandstone is very pure and coarse-grained sand rock composed of quartz. The particles of St. Peter Sandstone are loosely held together and in some

locations, it is a bed of sand. With an increase of cementing material, the St. Peter Sandstone rock becomes less friable and passes into quite a hard sandstone. About 1.22 to 1.83 meter of the upper part of the St. Peter Sandstone is usually cemented. The St. Peter Sandstone has a wide range of colors, varying from white, light gray, yellow, red, and chocolate brown. This coloring is due to small amounts of iron oxide which was deposited around and between the sand grains by percolating waters, the iron being derived from the overlying Trenton limestone. The colors are not distributed uniformly throughout the St. Peter Sandstone rock. The colors in some instance are arranged in alternating layers or stripes, giving the rock a banded appearance; or sometimes the colors are patches of several shapes and sizes. The St. Peter Sandstone is a pure sand rock containing almost 98.94% silica, 0.60% alumina and ferric oxide, 0.33% calcium oxide and 0.14% magnesium oxide. The thickness of St. Peter Sandstone varies from 9.14 m to 33.53 m. The St. Peter Sandstone formation has no traces of organic remains and fossils are seldom found.

Overlying the St. Peter Sandstone is the Trenton formation. The Trenton formation displays an abrupt change in character. This formation is composed of limestone and calcareous shales and clays. The limestone is mostly fine-grained and compact, occurring in thin beds of uneven thickness, blue-gray or buff color and rich in fossils. The Trenton formation varies in thickness from 24 to 50 meters.

The base of the Trenton formation and resting immediately on the St. Peter Sandstone is the green shale. The thickness of green shale is 0.61 to 1.22 meters. Overlying the green shales are 4.57 to 7.62 meters of dolomitic limestone in beds from 0.2 m to 0.61 or 0.91 meters thick, weathering to buff. The dolomitic limestone is succeeded by 7.62 to 9.14 meters of compact thin bedded, limestone that is very fine-grained and compact fossiliferous limestone in uneven layers 0.0254 to 0.0508 meters thick. This rock is brittle, usually breaks with a conchoidal fracture and is light gray and blue. Sometimes the beds are separated by partings of 0.0254 to 0.0508 meters in thickness. The irregularity in the thickness of the limestone layers is caused by undulating bedding planes. Vertical or nearly vertical joints are frequently present. The thin-bedded character is as a result of weathering. The thickness of this limestone varies significantly and in some locations, it makes up the main bulk of the formation. Above this is 1.52 to

1.83 meters thick of blue-green shale. The green shale is quite calcareous and contains lenses and bands of limestone rich in fossils (the most common being Othis subaequata and Monticuliporoids). The green shale is succeeded by limestone in thin beds, compact, blue and buff in color, fine-grained and fossiliferous with a thickness of 7.62 to 12.19 meters or more. About 2.44 to 3.05 meters of limestone overlies the green shale. Also, about 0.61 to 0.91 meter of green shale overlies the limestone (Table 3.1). These stratigraphic inputs presented in Table 3.1 are Ordovician rocks. These Ordovician rocks have lasted for almost 42 million years.

Table 3.1. Thicknesses of stratigraphic units at CGB and Pattison Sand mines

Rock layers	Thickness (m)
Green shale	0.61-0.91
Limestone	2.44-3.05
Blue-green shale	1.52-1.83
Limestone	7.62-12.19
Green shale	1.52 - 1.83
Limestone	7.62 - 9.14
Dolomitic limestone	4.57-7.62
St. Peter Sandstone (cemented)	1.22-1.83
St. Peter Sandstone (Uncemented)	9.14 -33.53
Green shale	0.6-1.22

3.3. FIELD MONITORING AT ST. PETER SANDSTONE MINES

Field monitoring in underground mines can be time-consuming, expensive and difficult. Field monitoring studies involve defining the goals of the study, developing a program for instrumentation, and selecting sites for instrument installation. The goal of the field studies was to monitor stress changes in pillars and roof deformations of room spans during underground mining in St. Peter Sandstone. The measured stress changes were used, later in the research, to validate 3D numerical models. The roof deformation assessment is critical to understand the mechanisms that lead to roof failure in St. Peter Sandstone mines.

3.3.1. Background Studies on Stress Change Monitoring. Stress changes in rocks can be induced or virgin stresses. Virgin stresses may change around a major discontinuity (e.g. fault, joints, and bedding planes). As the major discontinuity creeps, stress redistribution takes place. Induced stresses may change as a result of nearby excavation in rock, drilling, blasting, and applied loads (Amadei and Stephansson, 1997). The magnitude and distribution of induced stress changes in rock masses due to excavation are complex as some region in the rock mass can experience stress increases, while other areas experience stress decrease (Kaiser and Maloney, 1992). A decreasing or increasing stress changes can have a significant influence on ground conditions. On one hand, a decrease in rock stress can lead to failure by reducing confinement, thereby, causing rock blocks to slide or unravel (Dunnicliff, 1993). On the other hand, an increase in rock stress around an excavation provides a driving force that can cause rock instability with potential for considerable violence.

Stress change measurements in rocks have found several engineering applications. In underground mining, stress change measurement is primarily used to monitor the stability of pillars or excavation walls (Lee et al., 1976; Dunnicliff, 1993). Stress change monitoring is necessary for mine engineers to optimize mine layout and pillar design, and predict loads, rock bursts and mine stability upon blasting (Maleki, 1990). Additionally, monitoring of rock stress changes with time is crucial when assessing the short and long-term performance of underground excavations such as nuclear waste repository, laboratories and tunnels in different rock masses (Fiore et al., 1984; Hustrulid and McClain, 1984; Patrick and Rector, 1983; St. John and Hardy, 1982; Heuze, 1981; Patrick, 1986; Heuze et al, 1980; Lingle et al., 1983; Lingle and Nelson, 1982; Blejwas, 1987; Zimmerman, 1982; Martin and Simmons ,1993; Read and Martin, 1992). In petroleum engineering, predicting stress changes from reservoir depletion, compaction and subsidence deformation is critical when assessing future reservoir productivity (Teufel and Farrell, 1990). In general, stress change measurements aid engineers when evaluating the need for adopting, modifying, or if necessary, reconsider the design of underground structures in view of real ground conditions as excavation proceeds (Dunnicliff, 1993). Recently, the use of numerical modeling (finite element, finite difference, boundary element, discrete element, etc.) techniques in designs have greatly

increased the application of stress change measurement in rocks (Dunnicliff, 1993). In this research, stress change monitoring was used to validate finite difference numerical modeling, which is presented in Section 4 of this work.

Actual stress of a rock mass differs from place to place depending on geological features and local stress concentration effects (Dunnicliff, 1993). For this reason, a single point measurement may be misrepresentative. To improve the reliability of the monitoring program, it is important to make many measurements all through the rock mass of concern (Dunnicliff, 1993). Monitoring of stress changes may involve accurate measurement of small quantities conducted over a long period usually in harsh environments. The duration of the stress change monitoring program depends on the nature of the engineering activity responsible for stress change and the time required for the rock mass to reach a new state of equilibrium due to excavation dynamics (Amadei and Stephansson, 1997).

Measuring rock stress change for a long period is more liable to time-dependent errors and failure as the instrument is more likely affected by factors such as humidity, dust, temperature changes, and pore pressure, among others (Amadei and Stephansson, 1997). Temperature and seasonal changes in temperature are common at shallow depth. However, an instrument operating in these adverse environmental conditions must remain stable and sensitive to load changes and vibrations associated with blasting (Amadei and Stephansson, 1997). In addition, the researcher must select an instrument capable of monitoring stress changes in tension as well as compression (Amadei and Stephansson, 1997).

Stress change in rock cannot be measured directly. As a result, researchers resort to using indirect techniques to measure stress changes in rocks. Such indirect techniques use geotechnical instruments such as deformation gages, strain cells, stiff cylindrical inclusions, solid and hollow deformable inclusions, flat jacks and hydraulic borehole pressure cells, among others. Dunnicliff (1993) grouped these indirect techniques of measuring stress change into three forms. These are: (1) repeated measurement of in-situ stress approach; (2) geophysical techniques; and (3) measurement in a borehole method.

The repeated measurement of in-situ stress method is very expensive yet has low accuracy. It employs an absolute stress measurement technique to determine stress

change in a given rock mass. The geophysical method employs seismic waves to estimate in-situ stresses. However, this method is in the early stages of development. The borehole measurement technique is a viable method of stress change monitoring which employs stiff cylindrical inclusions for stress change measurement. The two types of stiff cylindrical inclusions are soft or rigid inclusion gages. Soft inclusions gages have small stiffness relative to the host rock whilst rigid inclusion gages (also called stressmeters) have stiffness larger than the host rock. The former requires knowledge of the host rock and the constitutive behavior whilst the later requires knowledge of the rock properties and constitutive behavior only within bound (Dunnicliff, 1993). Several researchers, including Lemcoe et al. (1980), Lingle et al. (1981), and Schrauf and Pratt (1979) have comprehensively discussed applications of borehole measurement technique elsewhere. The advantages, disadvantages, and limitations soft and rigid inclusion gages are discussed elsewhere (Dunnicliff, 1993).

Among the borehole measurement techniques, the vibrating wire stressmeter is the most commonly used in mining and civil engineering project to measure stress changes in rocks. The vibrating wire stressmeter was first suggested by Hawkes and Hooker (1974) as a low-cost tool particularly to monitor stress changes in mine pillars and around underground excavations. This device is robust and consists of thin-walled steel cylinder sealed at both ends with a pretensioned vibrating wire strain gauge/transducers mounted across the mid-length diameter of the cylinder (Amadei and Stephasson, 1997). A small electromagnet both excites and senses the natural vibration of the wire. A change of stress in the rock deforms the gage body slightly, changing the stress on the wire and shifting the fundamental vibratory period. Changes in the wire frequency due to changes in the hole diameter is directly proportional to the change in stress. Several researchers have reported the calibration and performance of vibratory wire stressmeter under various loading and temperature (Seller, 1977; Fossum et al., 1977; Lingle and Nelson, 1982; Jaworski et al., 1982; Lingle, Bakhtar and Barton, 1983; Patrick and Rector 1983; Dutta 1985; Mao 1986; Dutta and Hatfield 1987; Tunbridge and Oien 1987; Herget 1991).

The vibrating wire stressmeter is better in terms of performance than the other stress change monitoring devices. In the past, the problem of the vibrating wire

stressmeter was corrosion of the stressmeter body and wire. This resulted in failure of the instrument after installations, particularly, in moist and hot environment (Lingle and Nelson, 1982; Mao, 1986; Gregory and Kim, 1981; Rogue, 1983; Carlson et al., 1980). Gregory et al. (1983) researched into ways to prevent moisture infiltration. Another challenge was the lack of repeatability of the vibrating wire stressmeter. Amadei and Stephansson (1997) found that the lack of repeatability of the vibration wire stressmeter during calibration was as a result of changes in temperature and variability in the elastic rock modulus, particularly, in moist and hot environment. Preventing internal corrosion has helped improve the design and reliability of the vibrating wire stressmeter (Gregory et al, (1983). Generally, the vibrating wire stressmeter has become an attractive device for monitoring stress changes due to its long-term stability and low-cost (Amadei and Stephansson, 1997).

One variety of the vibrating wire stressmeter is the uniaxial vibrating wire stressmeter. Dutta (1981) established that the application of uniaxial vibrating wire stressmeter in rocks does not always produce surface contact of the borehole and the gage for each installation. The lack of surface contact between the borehole and the gage has significant influence on the gage readings hence it is desirable to install several gages at one location if maximum accuracy is required. Additionally, when a uniaxial vibrating wire stressmeter is installed in rock subjected to biaxial stress changes; it may not give a correct sign of stress changes in the direction of measurement (Dunnicliff, 1993). When a complete evaluation is required for stress changes in the plane normal to the borehole axis, three uniaxial stressmeter can be set at known orientations to each other (Parizeau, 1985). The substitute is to use biaxial stressmeter.

3.3.2. Stress Change Monitoring at Pattison Sand Mine. In this research, the biaxial stressmeter using the vibrating wire technology was used to monitor stress changes in pillars as excavation proceeds. The researcher used the 4350 biaxial stressmeter model manufactured by Geokon Incorporated (Lebanon, NH) (Figure 3.2).

The sensors of this stressmeter consist of a thick-walled steel cylinder, which is grouted in a borehole of the rock under investigation. This stressmeter has three vibrating wire sensors. These vibrating wire sensors are oriented in a plane perpendicular to the borehole at 60^{o} interval and measure the changes in the biaxial stress field in the pillar

rock around the sensor. Two sensors are incorporated in the biaxial stressmeter and measure the longitudinal deformation of the stressmeter. This allows corrections due to the changes in the stress directed along the borehole. Also, there are two vibration wire temperature sensors in the stressmeter which allows corrections due to temperature variations. In principle, the sensing elements are the vibrating wire strain transducer. This transducer is anchored across the diameter of the cylinder and measures the deformation of the cylinder. Coils and magnet assemblies which are located close to the vibrating wires are used to excite the wire and sense the frequency of vibration. When a gage is connected, pulses of frequencies are applied to the coil and magnet assemblies, and these cause the wire to vibrate at resonant frequency. The vibrating wire continues to vibrate and an electrical current, at the gage frequency is induced in the coil and transmitted to the readout box for display. The radial deformation of the thick-walled cylinder is related to associated stress change using theoretically derived equations.

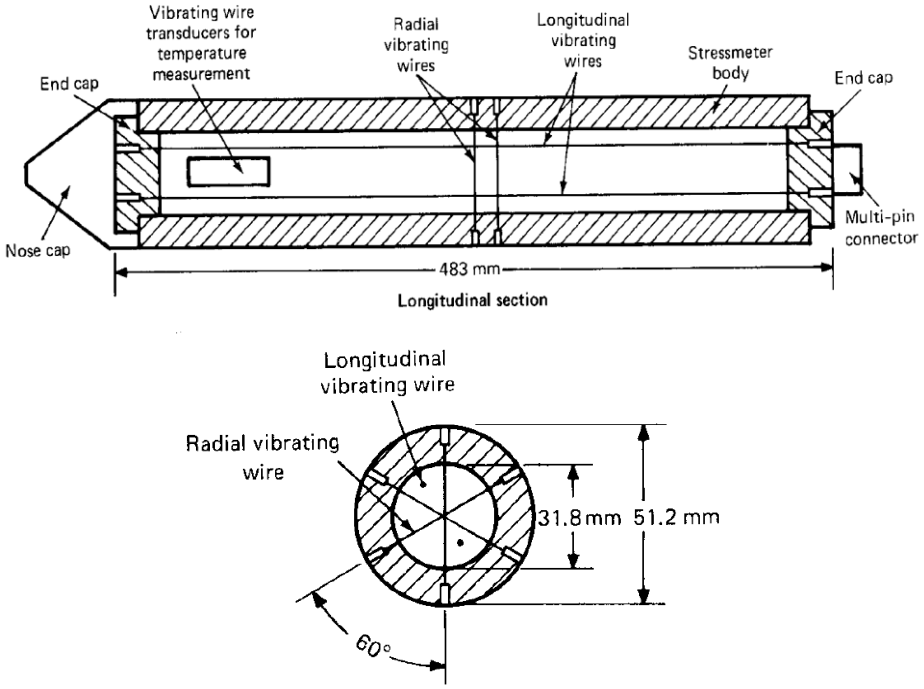

Figure 3.2. Biaxial vibrating wire stressmeter (Dunnicliff, 1993)

3.3.2.1 Planning installation of biaxial vibrating wire stressmeter. This researcher reviewed the instruction manual for the Geokon 4350 biaxial vibrating wire stressmeter carefully before the installing it. A 0.06 meter diameter diamond borehole was drilled slightly downwards to ensure that the grout does not drain from the borehole and that the stressmeter is fully surrounded with grout. Special Grout 400 expansive grout with high strength was used to ensure that the gage is in intimate contact with the surrounding rock. The proper setting tool was used for setting of the instrument in accordance with the Geokon 4350 instruction manual. After the installation, the zero reading was checked and it compared very closely to the factory reading after allowing the gage to come to an ambient temperature.

3.3.2.2 Description of instrument site. Overall, the researcher installed four (4) biaxial stressmeter at two locations at Pattison Sand Mine. At both locations, the pillar size (cross-sectional area) was 16.46 m^2 and 9.14 meter high. Also, the entry width was about 10.36 m. The roof layer was a cemented St. Peter Sandstone while the pillar rock was uncemented St. Peter Sandstone.

The researcher installed a biaxial stressmeter at 4 BQ/BP. The researcher installed this stressmeter about 7.92 m (26 feet) into the pillar (Figure 3.3). The estimated overburden depth at this site is 64 m, and the estimated vertical stress was 1.59 MPa.

The researcher installed three other biaxial stressmeters at 10 BY/BZ. The researcher installed these stressmeters about 3.08, 4.57 and 7.92 meters into the pillar from the same pillar rib (Figure 3.4). After almost a month of installation, a loose rock damaged the wire of the stressmeter installed 3.048 m into pillar rock. The overburden depth at this location was 52 meters, and the vertical stress was 1.29 MPa.

3.3.2.3 Data collection and processing. The researcher collected data at 15 minutes intervals immediately following installation to ensure good zero data and to see if the grout applies any small preload to the gage. Readings from the three radial gages were collected. The data processing involves computing the radial deformation; coefficients A and B; the maximum principal stress, minimum principal stress, and direction of the maximum principal stress p, q and θ, respectively.

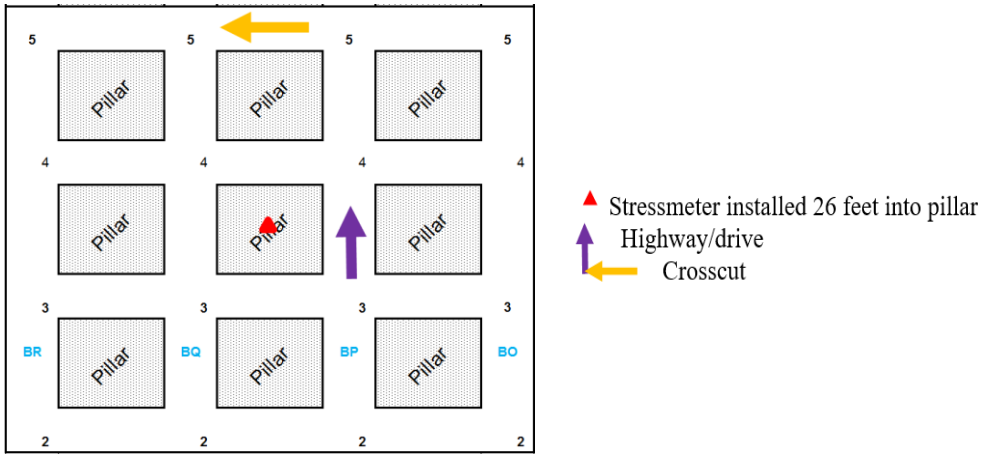

Figure 3.3. Location of biaxial stressmeter at 4BQ/BP

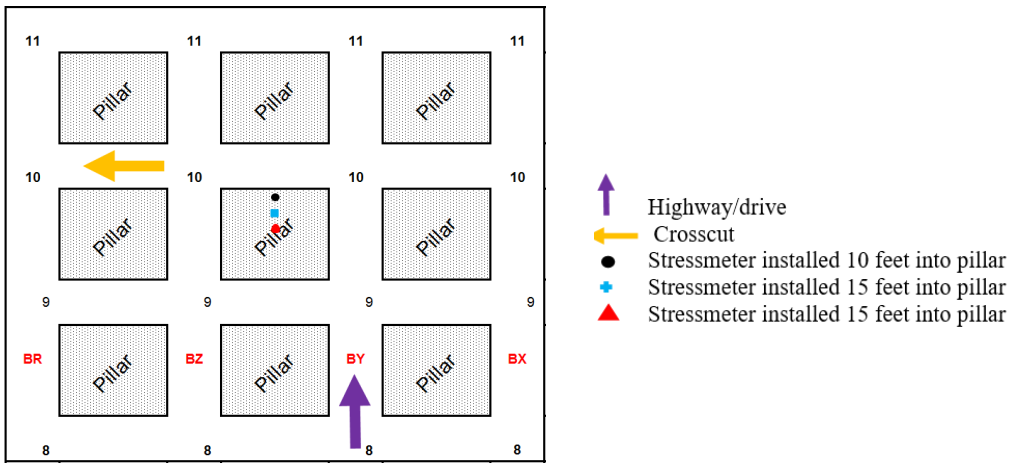

Figure 3.4. Location of biaxial stressmeter at 10BY/BZ. The red triangle is the approximate instrument location

3.3.2.3.1 <u>Gage deformation.</u> The diametral deformation of the gage is determined by measuring the resonant frequency of each of the three vibrating wires. The frequency of each wire is proportional to the strain in the wire. The researcher obtained Equations (5) to (10) from Geokon, (2017). Geokon (2017) reported that the fundamental frequency is given in Equation (5).

$$f = \frac{1}{2l_w}\sqrt{\frac{\varepsilon E_w g}{\rho_w}} \tag{5}$$

$$\Delta\varepsilon = G\Delta f^2 \tag{6}$$

$$G = \frac{4l_w^2\rho_w}{E_w g} \tag{7}$$

$$\Delta f^2 = f_o^2 - f_t^2 = 10^3(R_o - R_t) \tag{8}$$

The radial deformation (V_r) of the cylinder is given by:

$$V_r = \frac{l_w}{2} G\Delta f^2 \tag{9}$$

For biaxial stressmeter, l_w = 2 in and G = 0.36 x 10^{-9} sec^2

$$V_r = 2.54x10^{-8} G(R_o - R_t) \tag{10}$$

Where,

f = Natural frequency of the wire (s^{-1})

l_w = wire length = 0.0508 m (2 inches)

ε = wire strain

E_w = wire modulus = 207 GPa

ρ_w = wire density = 7.83 x 103 Kgm^{-3}

g = acceleration due to gravity = 9.81 ms^{-2}

R_0 = initial reading at time zero

R_t = final reading at time t

V_r = radial deformation in meters

G = Gages factors. Gage factor supplied for the three gages are 0.3522, 0.3622, and 0.3602 respectively

3.3.2.3.2 <u>Estimate "A" and "B".</u> The values of "A" and "B" can be computed graphically or theoretically. The researcher used the theoretical equations to obtain the value of A and B. Theoretical calculations make use of Equations (11) and (12) below (Geokon, 2017). The coefficients C_1 through C_9 depend on the sensor geometry and

material properties of the sensor and rock. Equations (13) to (26) defined the constants defined in Equations (11) and (12). The subscript *s* and *i* denote, respectively, the material properties of the sensor and the surrounding medium. The value of A and B are 4.87 x 10^{-8} and 2.71x10^{-7}.

$$A=\frac{R_2}{8\mu_s}\left[C_2(X_s-1)\frac{R_c}{R_2}+C_5\frac{R_2}{R_c}\right] \tag{11}$$

$$B=\frac{R_2}{8\mu_s}\left[C_3(X_s-3)\frac{R_c^{\,3}}{R_2^{\,3}}+C_7\frac{R_c}{R_2}+C_1(X_s+1)\frac{R_2}{R_c}+C_4\frac{R_2^{\,3}}{R_c^{\,3}}\right] \tag{12}$$

Where:

$$n=\frac{R_2}{R_1} \tag{13}$$

$$\mu=\frac{E}{2(1+\nu)} \tag{14}$$

$$X=\frac{3-\nu}{1+\nu} \qquad \text{(for plane stress)} \tag{15}$$

$$X=3-4\nu \qquad \text{(for plane strain)} \tag{16}$$

$$D=\left(\frac{\mu_i}{\mu_s}+X_i\right)n^2\left[\left(\frac{\mu_i}{\mu_s}-1\right)(3n^4-6n^2+4)+n^6\left(1+X_s\frac{\mu_i}{\mu_s}\right)\right]+\left(X_s\frac{\mu_i}{\mu_s}-X_i\right)\left[\left(\frac{\mu_i}{\mu_s}-1\right)+n^6\left(1+X_s\frac{\mu_i}{\mu_s}\right)\right] \tag{17}$$

$$C_1=2\left(\frac{1+X_i}{D}\right)\left[\left(\frac{\mu_i}{\mu_s}-1\right)+n^6\left(1+X_s\frac{\mu_i}{\mu_s}\right)\right] \tag{18}$$

$$C_2 = \frac{n^2(1+X_i)}{2\left(\frac{\mu_i}{\mu_s}-1\right)-n^2\left[\left(\frac{\mu_i}{\mu_s}-1\right)-\left(1+X_s\frac{\mu_i}{\mu_s}\right)\right]} \quad (19)$$

$$C_3 = -2\ \frac{(1+X_i)}{D}\, n^4 (n^2-1)\left(\frac{\mu_i}{\mu_s}-1\right) \quad (20)$$

$$C_4 = -2\left(\frac{1+X_i}{D}\right)\left[\left(\frac{\mu_i}{\mu_s}-1\right)+n^4\left(1+X_s\frac{\mu_i}{\mu_s}\right)\right] \quad (21)$$

$$C_5 = \frac{2C_2}{n^2} \quad (22)$$

$$C_6 = 2 - 2\ \frac{(n^2-1)}{n^2}C_2 \quad (23)$$

$$C_7 = 2\frac{(1+X_i)}{D}n^2\left[\left(\frac{\mu_i}{\mu_s}-1\right)(4-3n^2)+n^6\left(1+X_s\frac{\mu_i}{\mu_s}\right)\right] \quad (24)$$

$$C_8 = 2\text{-}2\ \frac{(1+X_i)}{D}\left[\left(\frac{\mu_i}{\mu_s}-1\right)(3n^6-6n^4+4n^2-1)+n^6(n^2-1)\left(1+X_s\frac{\mu_i}{\mu_s}\right)\right] \quad (25)$$

$$C_9 = -2+2\frac{(1+X_i)}{D}\left[\left(\frac{\mu_i}{\mu_s}-1\right)(4n^6-7n^4+4n^2-1)+n^4(n^4-1)\left(1+X_s\frac{\mu_i}{\mu_s}\right)\right] \quad (26)$$

3.3.2.3.3 <u>Estimating p, q, and θ.</u> Knowing A, B, and the radial deformations (V_{r1}, V_{r2}, and V_{r3}), the values of p, q, and θ, can be obtained using the equations below (Geokon, 2017). The researcher computed the values of p, q, and θ. These values are given in Appendix A.

$$p = \frac{1}{2}\left[\frac{1}{3B}\left((2V_{r_1} - V_{r_2} - V_{r_3})^2 + 3(V_{r_2} - V_{r_3})^2\right)^{1/2} + \frac{1}{3A}(V_{r_1} + V_{r_2} + V_{r_3})\right] \quad (27)$$

$$q = \left[\frac{1}{3A}(V_{r_1} + V_{r_2} + V_{r_3}) - p\right] \quad (28)$$

$$\theta_1 = \frac{1}{2}\cos^{-1}\left[\frac{V_{r_1} - A(p+q)}{B(p-q)}\right] \quad (29)$$

3.3.2.3.4 <u>Stress change results and discussions.</u> Stress change monitoring for the biaxial stressmeter installed at 4BQ/BP commenced on 4/29/2013 and continued until 1/16/2014. Figure 3.5 shows the results of the stress change monitoring exercise at this location. Overall, the maximum and minimum principal stress change increased with time as the excavation continued. The maximum principal stress change reached the highest value of 0.23 MPa after 130 blasts in 8 months at Pattison Sand Mine. Similarly, the minimum principal stress change reached the highest value of 0.31 MPa after 130 blasts in 8 months at Pattison Sand Mine.

Stress change monitoring for the biaxial stressmeter installed at 10BY/BZ commenced on 3/14/2014 and continued until 6/26/2014. This stress change monitoring continued for almost one (1) year. Within this duration, the researcher recorded 64 blasting activities at the mine. As aforementioned, the researcher installed three biaxial stressmeters positioned at 3.04, 4.57 and 7.92 meters into the pillar. Twenty-seven days following the installation, a loose rock fell and damaged the wires of the stressmeter installed 3.04 meters into the pillar rock. For the reason, its results were not presented here. Figure 3.6 shows the results of the stress change monitoring exercise at 10BY/BZ. The researcher did not record any instrument data for 193 days (from 6/28/2014 to 1/7/2015) due to no blasting activity at the mine. The maximum principal stress change reached a highest value of 0.10 MPa, while the minimum principal stress change reached -0.14 MPa, for the stressmeter installed 4.57 feet into the pillar. The maximum principal

stress change reached a highest value of 0.14 MPa, while the minimum principal stress change reached -0.07 MPa, for the stressmeter installed 7.92 meters into the pillar. At 10BY/BZ, maximum principal stress change appeared to be relatively high at the pillar core compared to pillar rib (Figure 3.6). However, the opposite is valid in the case of minimum principal stress change. Further stress change measurement will be required to explain these phenomena.

The sensors of the biaxial stressmeter are set-up to measure compressive stresses. A positive sign means the vibrating wire is in compression whilst negative means the vibrating wire is in tension. Compression or tension will depend on the magnitude of initial reading (R_o) and final reading (R_t), in that, if R_o is greater than R_t, a positive stress change will result and vice versa. In effect, a positive stress change will mean that the vibrating wire is in compression. On the other hand, a negative stress change means the vibrating wire may be experiencing stress relaxation, or lack of contact with the surrounding medium as a result of stress redistribution, or yield at the contact between the grout and the surrounding medium.

The biaxial stressmeter is capable of measuring stress changes in a medium from 0.04 MPa to up to 207 MPa. A high stress change in pillars indicates pillar instability. The opposite is true. Overall, the low stress changes measured at both locations suggest that the pillars at Pattison Sand Mine are stable.

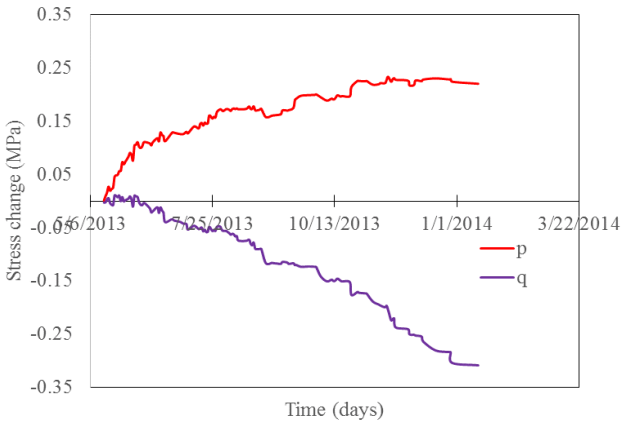

Figure 3.5. Stress change monitoring at 4 BQ/BP using biaxial vibrating wire stressmeter at Pattison Sand Mine

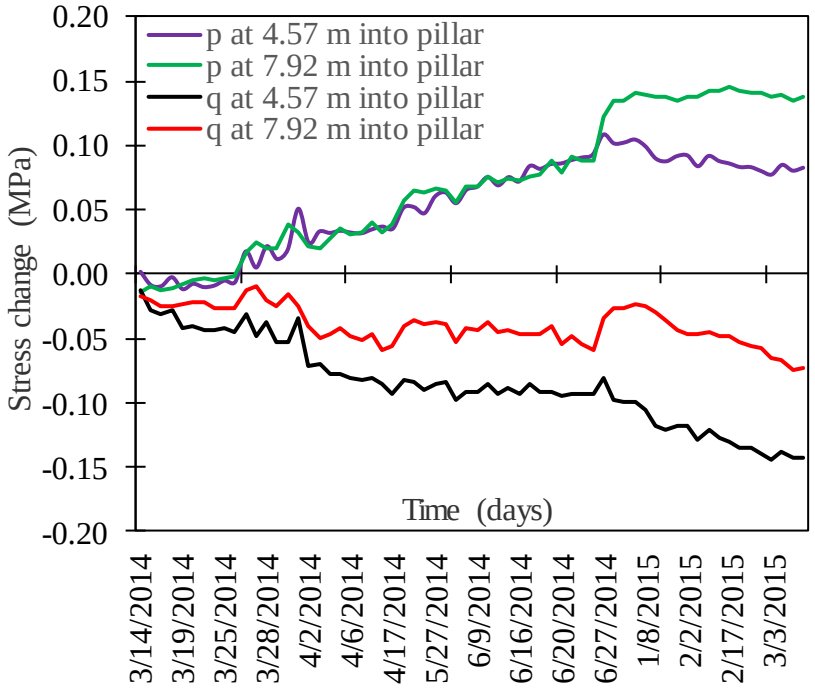

Figure 3.6. Stress change monitoring at 10 BY/BZ using biaxial vibrating wire stressmeter at Pattison Sand Mine

3.3.3. Roof Displacement Monitoring at Pattison Sand Mine. Measurement of rock deformations using borehole extensometers is essential to stability and behavioral monitoring of underground openings. The main goal of this instrumentation monitoring program was to measure the displacement of the roof at the Pattison Sand Mine.

In principle, the Geokon Model 4450 transducer consists of a vibration wire sensing element. A stress relieved spring connects the wires at one end and a connecting rod at the other end. As the connecting rod is pulled out from the gage body, the spring elongates causing an increase in tension. The vibrating wire element senses the change in tension in the spring. The tension in the wire is directly proportional to the extension. The change in displacement is a measure of the strain change in the vibrating wire. This instrument was equipped with vibrating wire cords for digit reading, and a thermistor to measure the temperature of the surroundings.

3.3.3.1 Instrument location. Overall, the researcher installed ten extensometers at two locations at Pattison Sand Mine. Five (5) extensometers were installed across the mine roof at each location to obtaining adequate roof displacement distributions. Each

borehole extensometer (Geokon Model A-1B) was equipped with Geokon Model 4450 vibration wire transducer to measure roof displacement. The location for the placement of the instruments was carefully selected with the help of mine officials to give representative data on the effect of displacement before and after blasting activities. The researcher installed these extensometers at the 4BO/BP and 10 BY/BZ crosscuts. The description of the sites is similar to that mentioned above (Section 3.3.2.2). The extensometers were placed in series at 1.524 m (5 feet) intervals.

3.3.3.2 Installation, data collection, and processing. The researcher and a team at the mine carefully followed the installation procedure in Geokon Model 1A-1B's manual. The extensometer installation team consisted of the researcher and other mine officials.

First, the team assembled the extensometer and then inserted the rod assembly and rockbolt anchor into the borehole. Then the extensometer assembly was pushed into the borehole until it was 0.38 meters from the collar of the borehole. At this point, the rockbolt anchor was expanded and tightened. The team inserted an expansion shell anchor into the borehole until the end of the swagelock fitting was about 0.0508 meters inside the hole, and tightened with a socket wrench. The team inserted the vibrating wire transducer into the swagelock fitting. We pushed the vibrating wire transducer until it engaged the connecting rod and then pushed it by rotating it by hand while applying inward pressure. We tightened the transducer into the connecting rod and connected the readout box to the black and red lead wires. We then gently pulled the sleeve of the transducer until we obtained a recording within 2500 -7500 digits. A stable reading within this range for each of the extensometers was taken as the initial reading. Finally, the team tightened the swagelock nut. The researcher used these procedures to installing all extensometers at Pattison Sand Mine. To avoid misreporting readings at each site, the researcher labeled each extensometer (see labels A, B, C, D, and E in Figure 3.7).

The researcher took the initial readings immediately after the installations. The temperature of the surroundings was also taken immediately following the installation. These initial readings served as a reference for subsequent displacement calculations. The GK 404 readout box displays the vibrating wire value in digits and temperature measurement in centigrade. When the extensometers are adjacent to the active excavation

areas, the mine officials took two readings per day - one reading before and the other after blasting. This arrangement helped to examine the effect of blasting on the roof displacements. However, as the excavation proceeds further away, the site engineers took one reading daily. The site engineer sent this information to the researcher for further processing and analysis. The researcher immediately processed the data and examined if there were any significant ground movement or instability issues. The digit readings are related to the change in displacement. The displacement measured by the vibrating wire transducer is given by Equation (30).

$$D_{uncorrected} = G(R_1 - R_0) \tag{30}$$

Where,

R_1 the current reading in digit

R_0 is the initial reading in digit

G is the calibrated factor in mm/digit (this was supplied by Geokon)

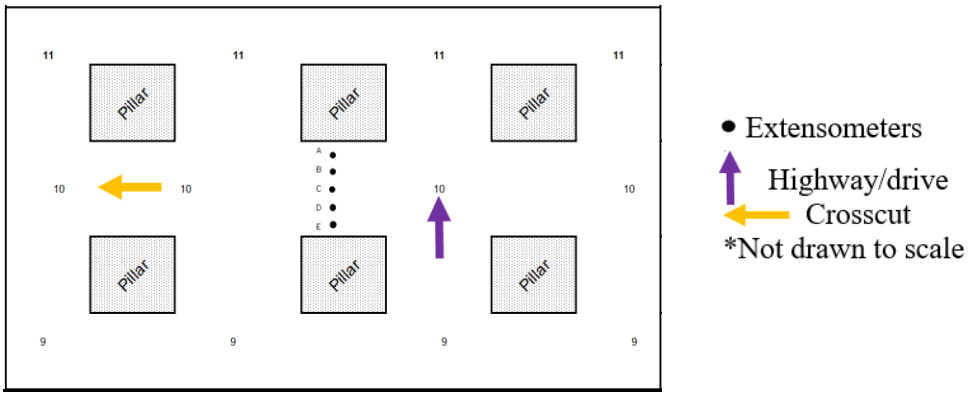

Figure 3.7. Location of extensometer at 10BY/BZ

The model 4450 vibrating wire transducers have a small coefficient of thermal expansion so often correction is not necessary. However, to achieve accurate results, temperature correction is applied when the temperature difference is greater than 10 centigrade. The temperature change ranged from -9^{o}C to 6^{o}C from the field measurements. As a result, the researcher did not apply temperature corrections to the

displacement values. A positive displacement change value represents compression whilst a negative displacement change value represents an extension.

3.3.3.3 Results and discussion of roof displacement monitoring. Roof displacement monitoring for the instrument installed at 4BO/BP commenced on 3/18/2013 whilst that at 10BY/BZ commenced on 3/17/2014. The roof displacement monitoring continued for 15 months and 11 months, respectively, at 4BO/BP and 10BY/BZ. Figures 3.8 and 3.9 show the roof displacement results for the instruments installed at 4BO/BP and 10BY/BZ sites, respectively. The results of the roof displacement monitoring are presented in Appendix B.

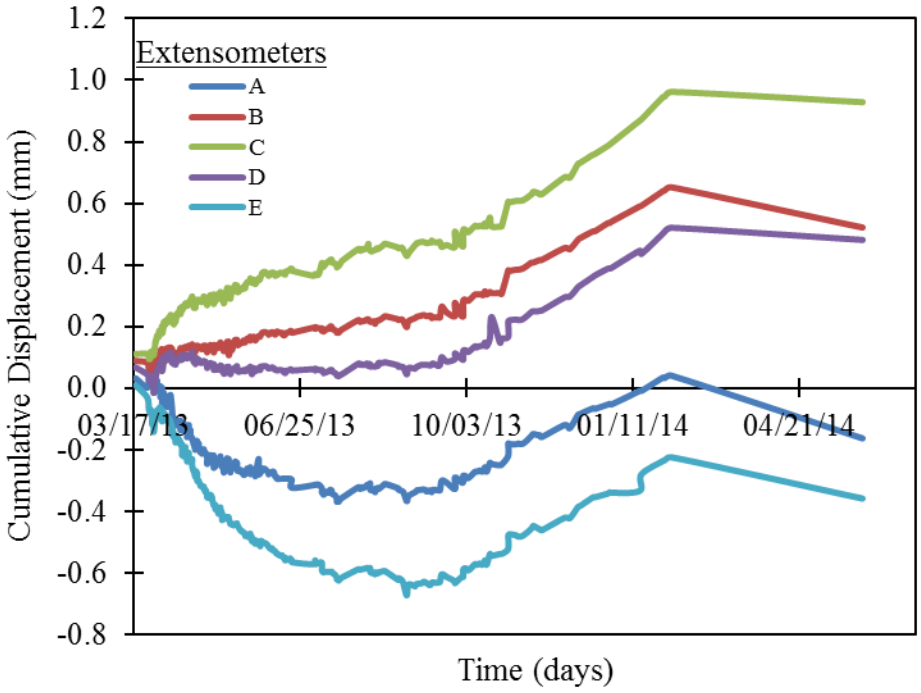

Figure 3.8. Roof displacement with time at 4BO/BP

Overall, the maximum roof displacement was 0.96 mm and 1.38 mm, respectively, at 4BO/BP and 10BY/BZ. In general, the maximum roof displacement occurred at the mid-length of the roof. The roof displacement results at 4BO/BP indicate a zone of tension (about 1.524 m from the pillar rib) and compression (between 1.524 to

7.3152 m of the roof length). However, the displacement results show that the entire roof at 10BY/BZ is under compression. Figures 3.10 and 3.11 show the roof displacement profiles as time increased for 4BO/BP and 10BY/BZ, respectively. The fact that roof displacement profiles obtained at 4BO/BP confirmed qualitatively to theoretical predictions, offers credibility both to the classical beam theory (Timoshenko, 1940; Sochor, 2001) and the displacement measurements.

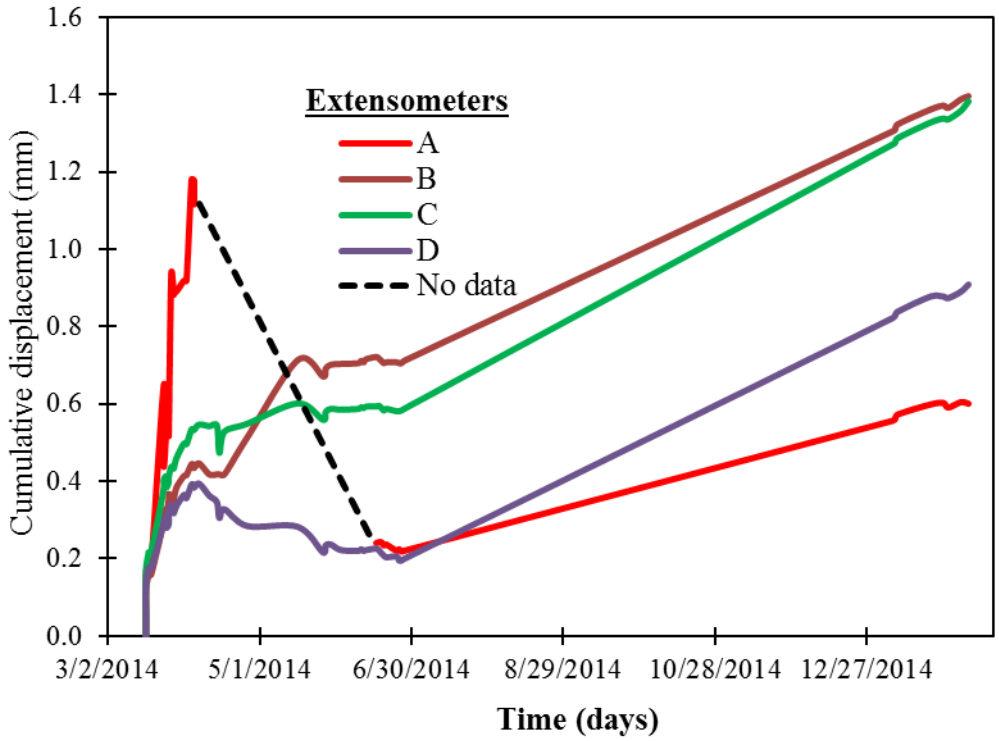

Figure 3.9. Roof displacement with time at 10BY/BZ

Another goal for the roof displacement monitoring exercise was to examine the effect of blasting activities on roof stability. Specifically, the researcher has looked into the effect of blasting on roof displacement for each extensometer, particularly at 4BO/BP. Figures 3.12 to 3.16 present the roof displacement with time before and after blasting for each extensometer at 4BO/BP. The researcher also looked into the effect of blasting on daily roof displacement profiles at 4BO/BP and 10BY/BZ.

Figures 3.17 to 3.24 present daily roof displacement before and after blasting at various days specifically at 4BO/BP. Similarly, Figures 3.25 to 3.28 present some daily roof displacement before and after blasting at various days, specifically at 10BY/BZ.

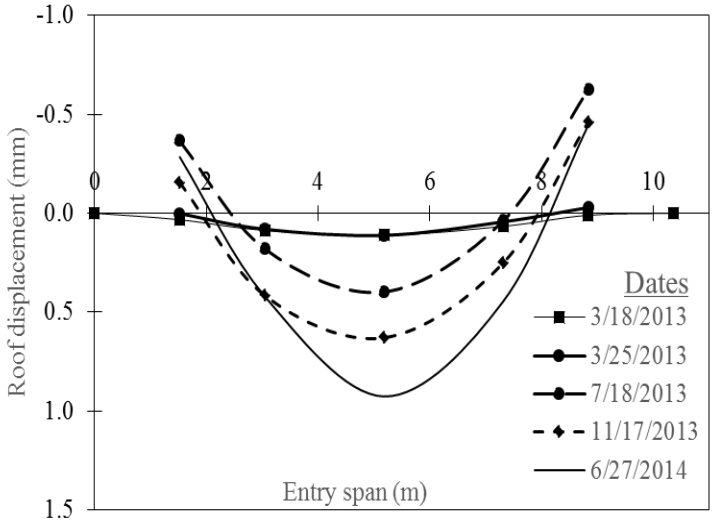

Figure 3.10. Displacement across the roof with time at 4BO/BP

In this study, the researcher investigated whether there is a significant difference between the roof displacement values recorded prior to and after blasting. Due to limited data and challenges in acquiring roof displacement data at 10BY/BZ, the researcher conducted the analysis only at the 4BO/BP site. The researcher analyzed the effect of prior and after blasting activities on roof displacement using 95% Bonferroni's simultaneous confidence interval (Table 3.2). As shown in Table 3.2, the lower and upper 95% confidence interval values indicate that the difference between the means is significant and cannot be zero. This clearly suggests that there is a significant difference between the displacement values recorded prior to and after blasting. The study concluded that blasting influenced roof displacement at 4BO/BP site.

The study also analyzed whether a significant difference exists between daily prior and after blasting activities on roof displacement profiles at 4BO/BP and 10BY/BZ sites. In particular, the researcher used the daily roof displacement profiles presented in Figures 3.17 to 3.28 to conduct this analysis. The researcher analyzed the effect of

blasting on daily roof displacement profiles using the 95% Bonferroni's simultaneous confidence interval as well as the difference in means (Table 3.3). At the 4BO/BP site, the lower and upper simultaneous 95% confidence interval values indicate that the difference between the means is insignificant and can be zero. However, at the 10BY/BZ site, the lower and upper 95% confidence interval values indicates that the difference between the means is significant and cannot be zero. This study concludes that there is a significant difference between the displacement profiles prior to and after blasting at 10BY/BZ site. However, there is no significant difference between the displacement profiles prior to and after blasting at the 4BO/BP site. These conflicting results are possibly due to the data acquisition methods in this research.

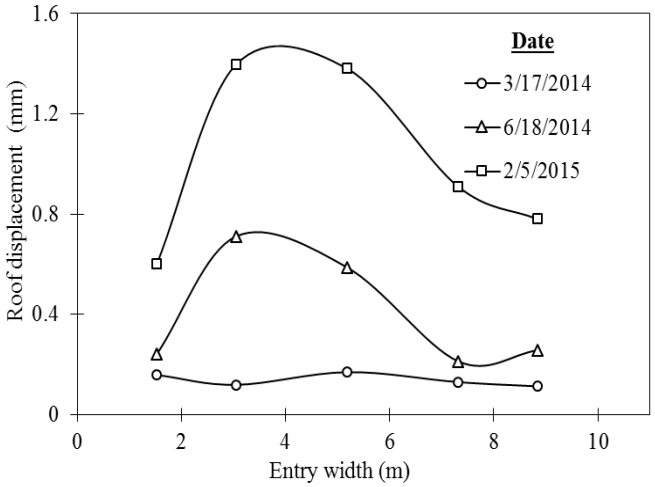

Figure 3.11. Displacement across the roof with time at 10BY/BZ

It is important to note that the site engineers took the readings from the readout box manually. Also, these readings were taken about 3 hours from the time of blasting. It is possible that these engineers missed meaningful displacement data especially in the first zero (0) to one (1) hour after each blasting. For this reason, the effect of blasting on roof displacement may be limited. Future research should use automatic data acquisition systems (such as data loggers) to shed more light on this.

Table 3.2. Effect of blasting on roof displacement at 4BO/BP

Extensometer ID	Displacement readings		Difference between means	Simultaneous 95% confidence interval	
A	Before blasting	After blasting	-0.009	-0.231	-0.205
B	Before blasting	After blasting	-0.004	0.187	0.214
C	Before blasting	After blasting	-0.002	0.367	0.406
D	Before blasting	After blasting	-0.002	0.090	0.112
E	Before blasting	After blasting	-0.005	-0.445	-0.403

Table 3.3. Effect of blasting on daily roof displacement profiles

Sites	Daily displacement profile		Difference between mean	Simultaneous 95% confidence interval	
	Before blasting	After blasting			
4 BO/BP	3/28/2013	3/28/2013	0.016	-0.0307	0.0812
4 BO/BP	3/29/2013	3/29/2013	-0.017	-0.0508	0.0766
4 BO/BP	3/30/2013	3/30/2013	-0.029	-0.0271	0.0989
4 BO/BP	3/31/2013	3/31/2013	-0.015	-0.0083	0.1161
4 BO/BP	4/1/2013	4/1/2013	-0.002	-0.0083	0.1199
4 BO/BP	5/27/2013	5/27/2013	0.010	-0.2688	0.1855
4 BO/BP	10/1/2013	10/1/2013	0.036	-0.3032	0.2862
10 BY/BZ	3/25/2014	3/25/2014	-0.008	0.2740	0.4316
10 BY/BZ	3/26/2014	3/26/2014	0.003	0.2567	0.4530
10 BY/BZ	3/28/2014	3/28/2014	0.001	0.2488	0.6148

3.4. FIELD INVESTIGATIONS AT PATTISON SAND MINE

This Section presents the results of field investigations during site visits to the Pattison Sand and CGB Mines. The researcher conducted numerous field visits to the CGB and Pattison Sand Mines. The key purpose of the visits was to conduct extensive field investigations at these mines. The goal of the field investigation was to survey room and pillar geometries that have worked successfully at the CGB and Pattison Sand Mines. The researcher used the mine topographical map to determine the overburden depths on each of the surveyed pillars. Appendix C summarizes the information collected.

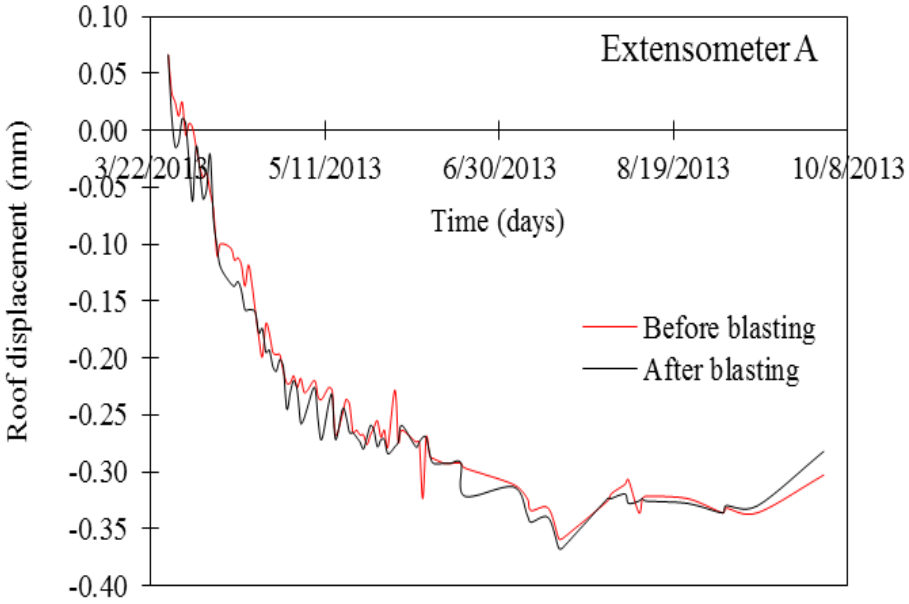

Figure 3.12. Effect of blasting on roof displacement at 4BO/BP on extensometer A

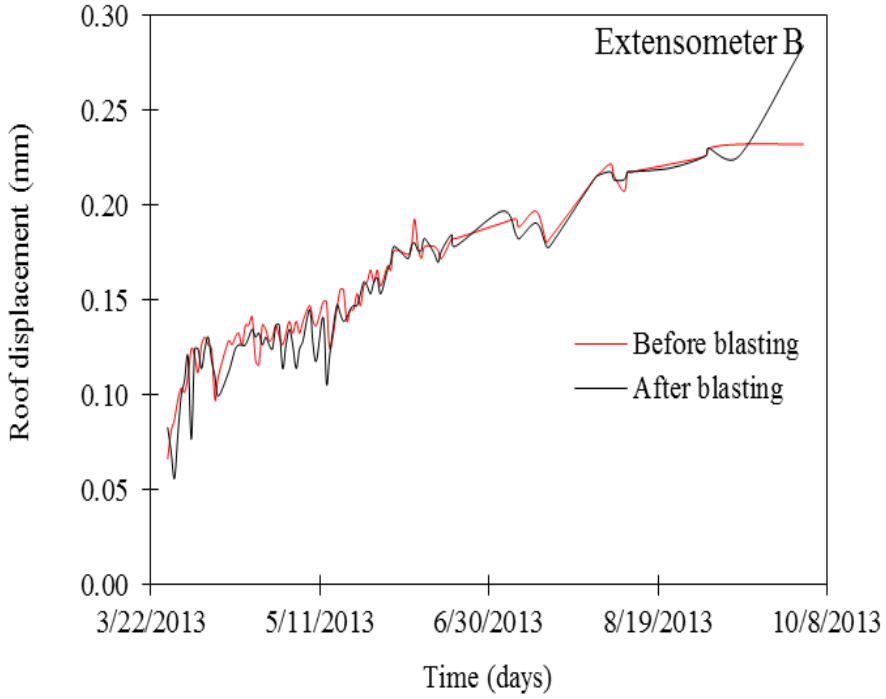

Figure 3.13. Effect of blasting on roof displacement at 4BO/BP on extensometer B

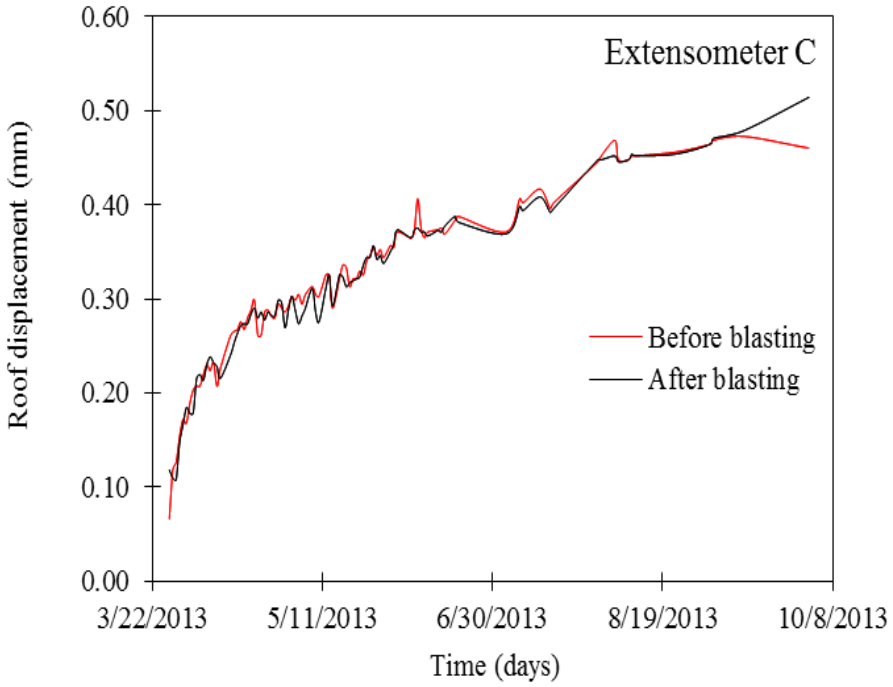

Figure 3.14. Effect of blasting on roof displacement at 4BO/BP on extensometer C

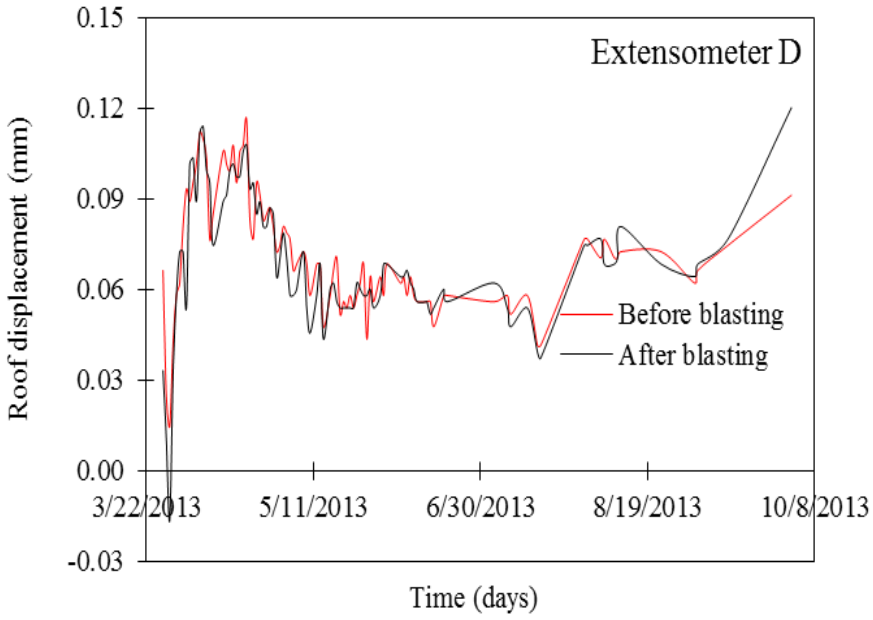

Figure 3.15. Effect of blasting on roof displacement at 4BO/BP on extensometer D

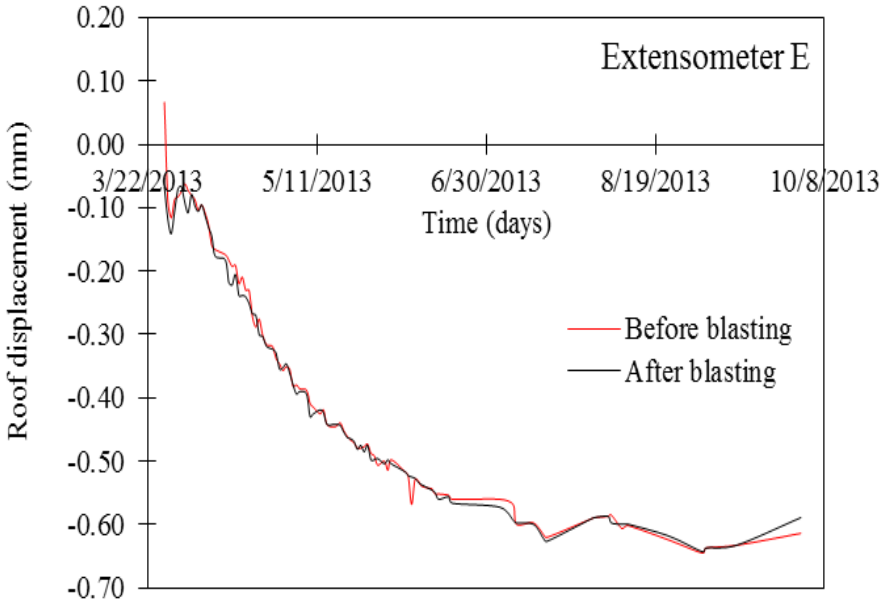

Figure 3.16. Effect of blasting on roof displacement at 4BO/BP on extensometer E

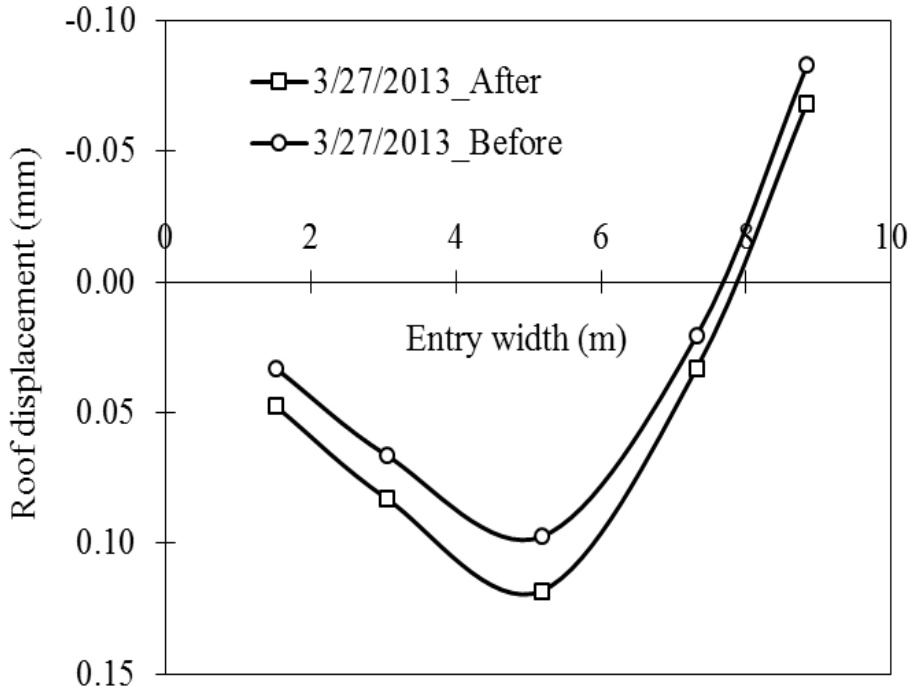

Figure 3.17. Influence of blasting on roof displacement profiles at 4BO/BP on 3/27/2013

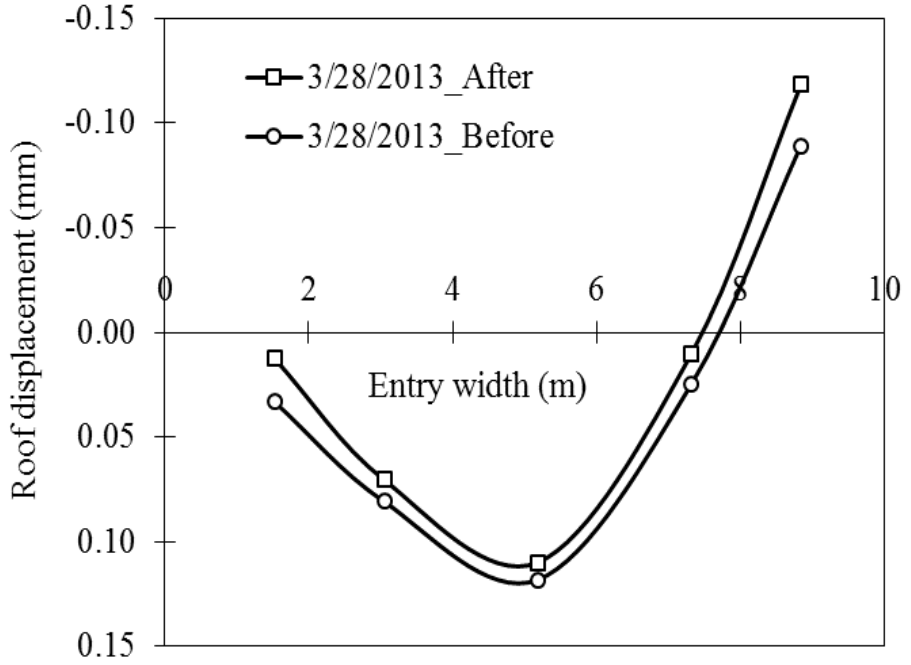

Figure 3.18. Influence of blasting on roof displacement profiles at 4BO/BP on 3/28/2013

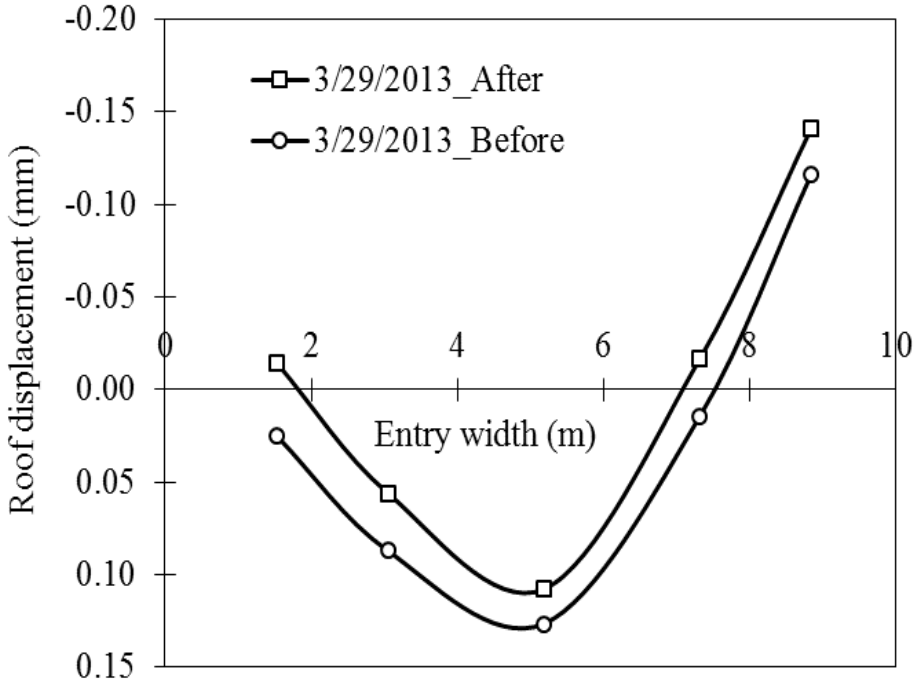

Figure 3.19. Influence of blasting on roof displacement profiles at 4BO/BP on 3/29/2013

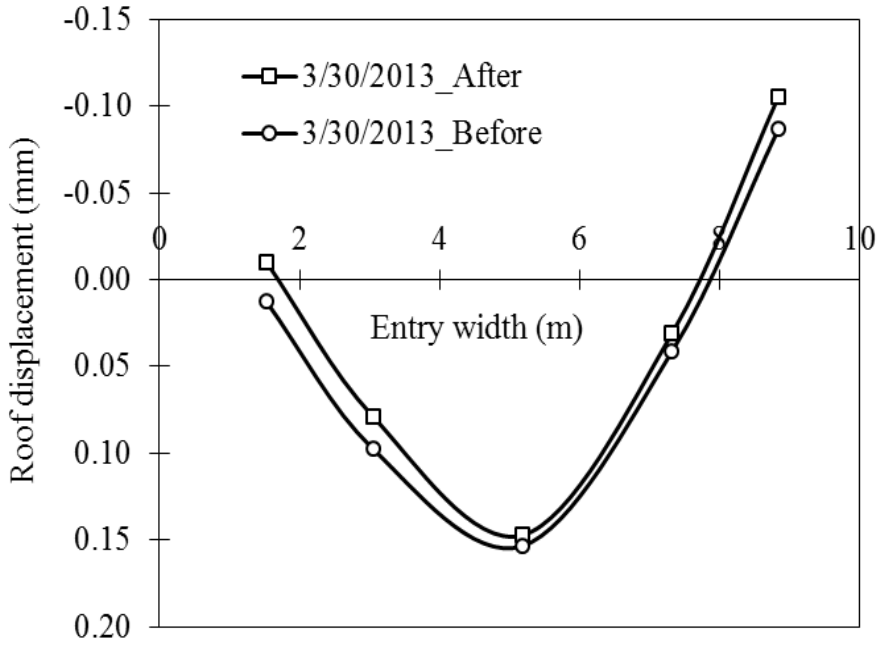

Figure 3.20. Influence of blasting on roof displacement profiles at 4BO/BP on 3/30/2013

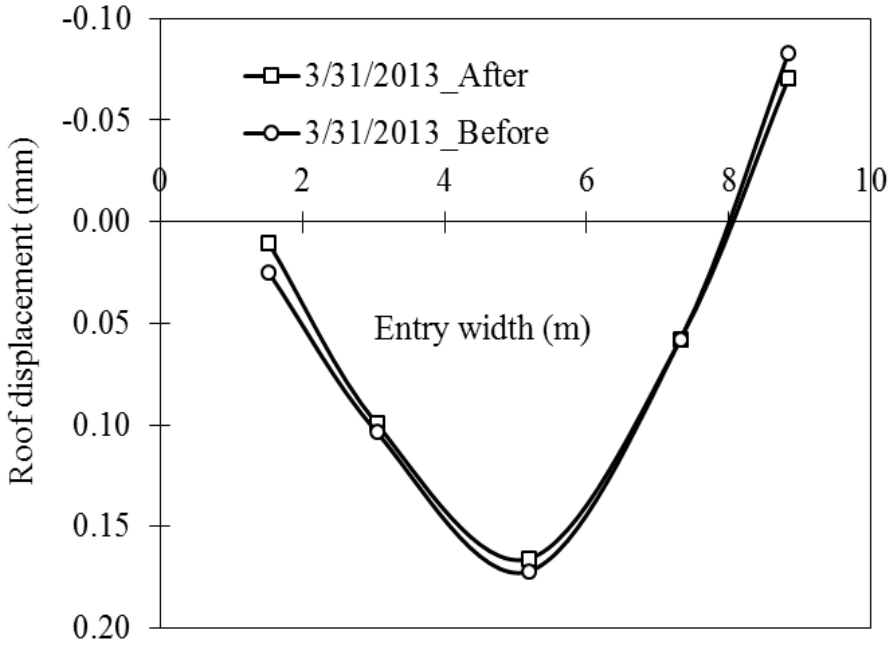

Figure 3.21. Influence of blasting on roof displacement profiles at 4BO/BP on 3/31/2013

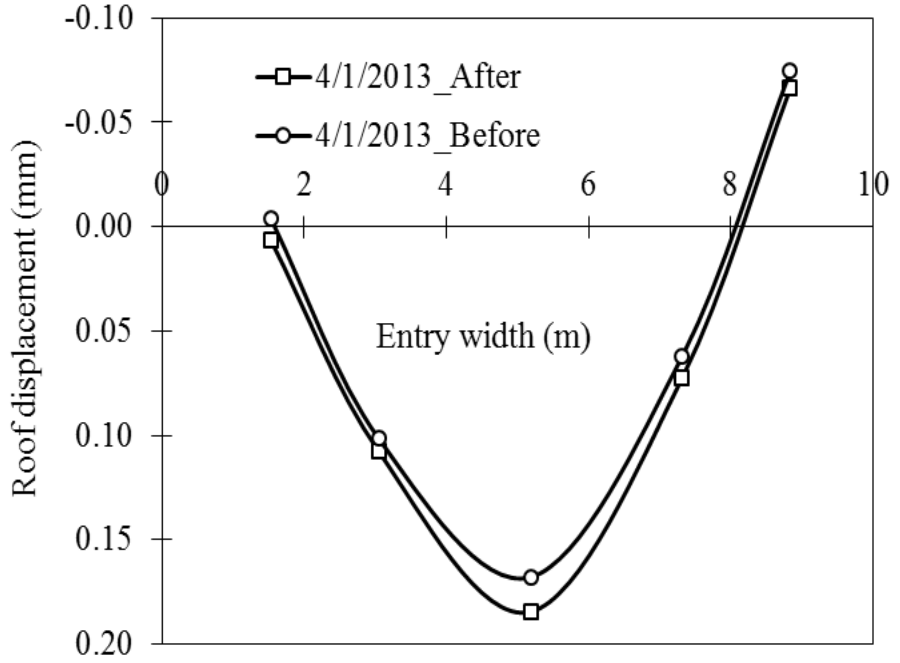

Figure 3.22. Influence of blasting on roof displacement profiles at 4BO/BP on 4/01/2013

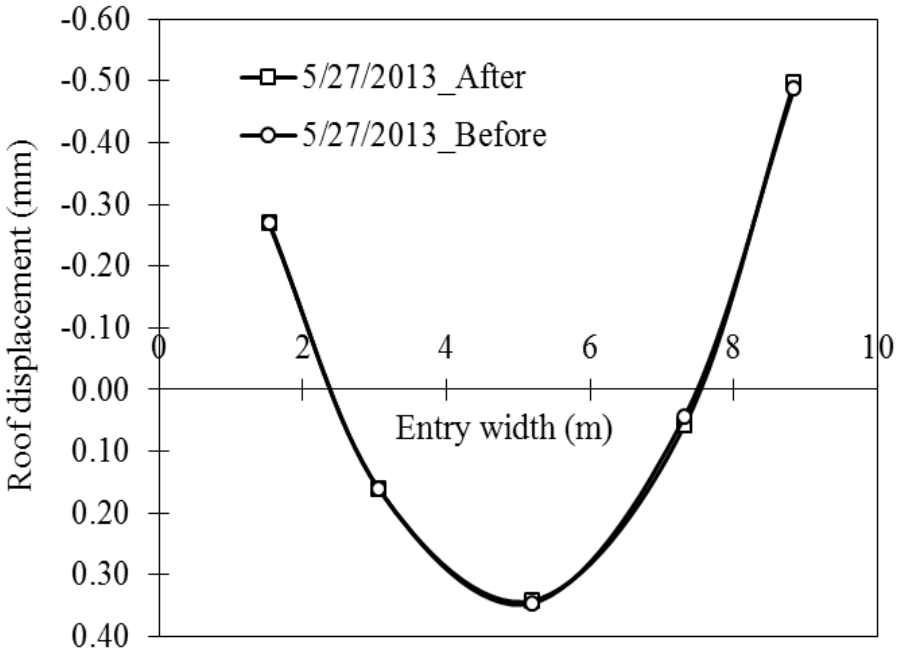

Figure 3.23. Influence of blasting on roof displacement profiles at 4BO/BP on 5/27/2013

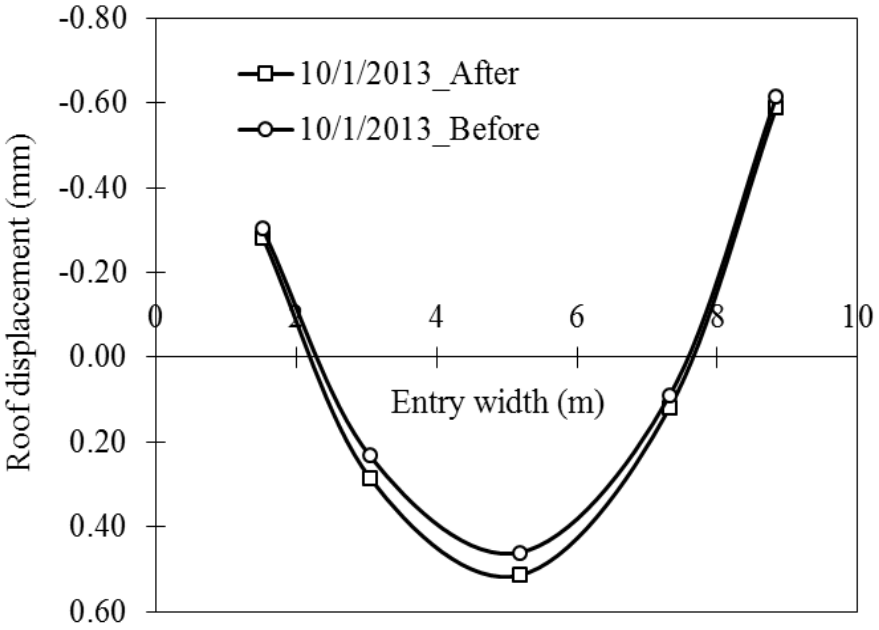

Figure 3.24. Influence of blasting on roof displacement profiles at 4BO/BP on 10/01/2013

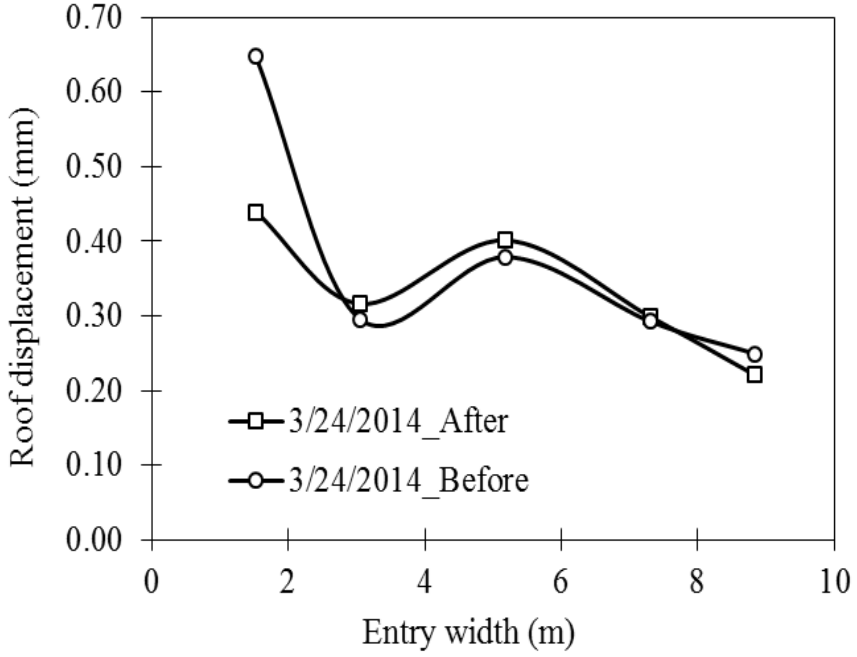

Figure 3.25. Influence of blasting on roof displacement profiles at 10BY/BZ on 3/24/2014

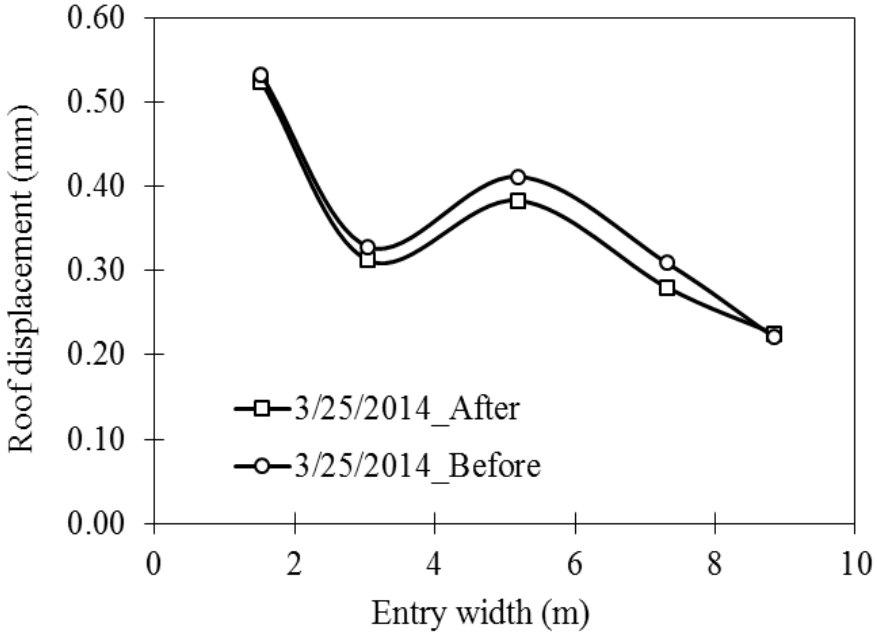

Figure 3.26. Influence of blasting on roof displacement profiles at 10BY/BZ on 3/25/2014

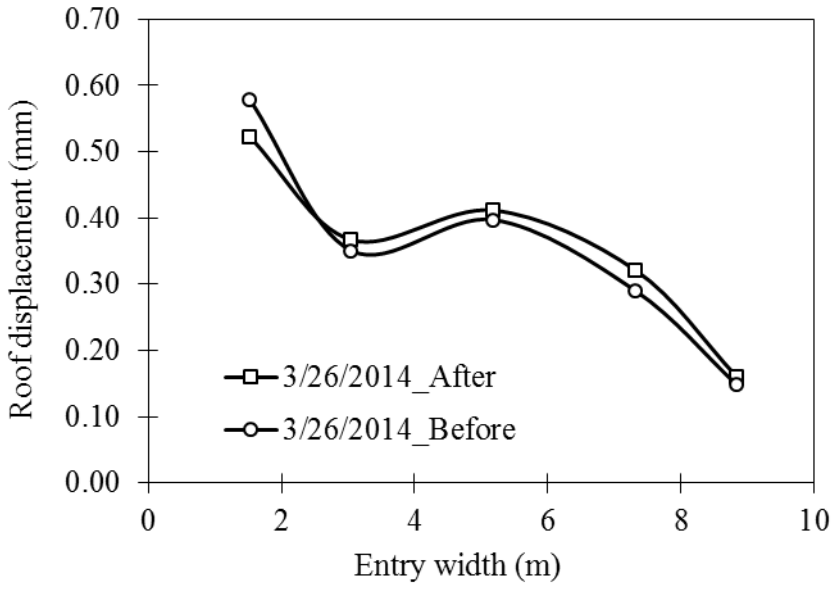

Figure 3.27. Influence of blasting on roof displacement profiles at 10BY/BZ on 3/26/2014

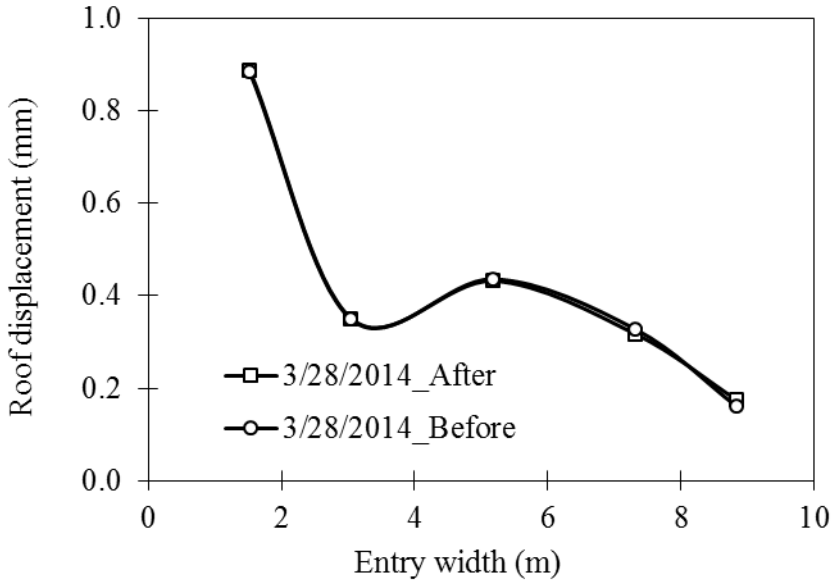

Figure 3.28. Influence of blasting on roof displacement profiles at 10BY/BZ on 3/28/2014

Another goal of the field investigation was to document the physical conditions of the pillars at the time of the survey. Appendix D shows the physical conditions of these pillars the researcher surveyed.

At the CGB Mine, the equivalent pillar widths varied from 11.89 to 16.76 square meters, with a mean of 14.33 meters (47 feet). Figure 3.29(a) shows a histogram of the pillar widths. As shown in Figure 3.29(a), 75% of the pillar sizes are within the range of 12.19 to 15.24 square meters.

The pillar heights ranged from 7.01 to 14.33 meters, with a mean of 10.36 meters. Figure 3.29(b) shows a histogram of the pillar heights. The width to height (w/h) ratios ranged from 0.95 to 2.05 meters with a mean of 1.45 meters. Figure 3.29 (c) shows a histogram of the pillar width to height ratios. The room width varied from 8.53 to 14.63 meters with a mean of 11.28 meters. Figure 3.29(d) shows a histogram of the surveyed entry widths. The overburden depth ranged from 33.53 to 65.23 meters with a mean of 52 meters. Figure 3.29(e) shows a histogram distribution of the surveyed overburden depth. The stress imposed on the pillars ranged from 2.31to 6.86 MPa with a mean of 4.16 MPa. Figure 3.29(f) shows a histogram distribution of the overburden depth surveyed.

Generally, the researcher observed that the roofs were stable although unsupported. The survey documented that some locations had pinch out failures. The researcher observed previous support practices involved the application of shotcrete to remediate pinch out failures. The pillar survey did not reveal any case in which a pillar or array of pillars had collapsed or showing potential signs of instability. This information is critical for empirical pillar design purposes. Figures 3.30 and 3.31 show stable pillar cases having w/h ratio of 0.95 and 1.17, respectively.

It is important to recall that the CBG Mine was operated from 1945 to 1982. The age of the pillars ranges from 35 to 72 years. The reader can see the physical conditions of some of these pillars at Appendix D. It is evident that these rooms and pillars are stable. There was no recorded incident of roof collapse or any other indication of pillar failure at this mine. The study revealed that the roof spans were mostly unsupported. Pinch out failures on some of these pillars did not show any sign of pillar instability.

This study has presented the most comprehensive database from which a researcher can derive a realistic pillar design methodology for St. Peter Sandstone. Based on these field investigations, one can conclude that pillar designs (dimensions and roof spans) at CGB mine are adequate to support the overburden stresses incident on them. Consequently, a researcher or mine engineer can adopt these room and pillar dimensions under similar overburden stress conditions and for safe and economic pillar design purposes.

3.5. GROUND CONTROL CHALLENGES AT PATTISON SAND MINE

This Section presents ground control challenges of mining in St. Peter Sandstone. It is important to note that the unit operations for mining St. Peter Sandstone at Pattison Sand Mine are drill, blast, load and haul, and ground support. However, underground mining in St. Peter Sandstone formation presents several unique ground control challenges due to its friable nature. Some of these challenges include rock reinforcement techniques, pinch out failures, and roof failures.

At the Pattison Sand Mine, the United States Mine Health and Safety Administration (MSHA) wrongly interpreted the occurrence of “pinch out” failures as direct evidence that, the pillars were overstressed. Therefore, MSHA recommended that

pillar sizes be increased by 150 to 250%. If these recommendations were implemented, it would have eventually closed the mine as the mine would no longer be economically viable. From MSHA's perspective, "pinch out" failure was seen as a pillar failure problem, a conclusion which ultimately led to a partial shutdown of Pattison Sand Mine in 2010.

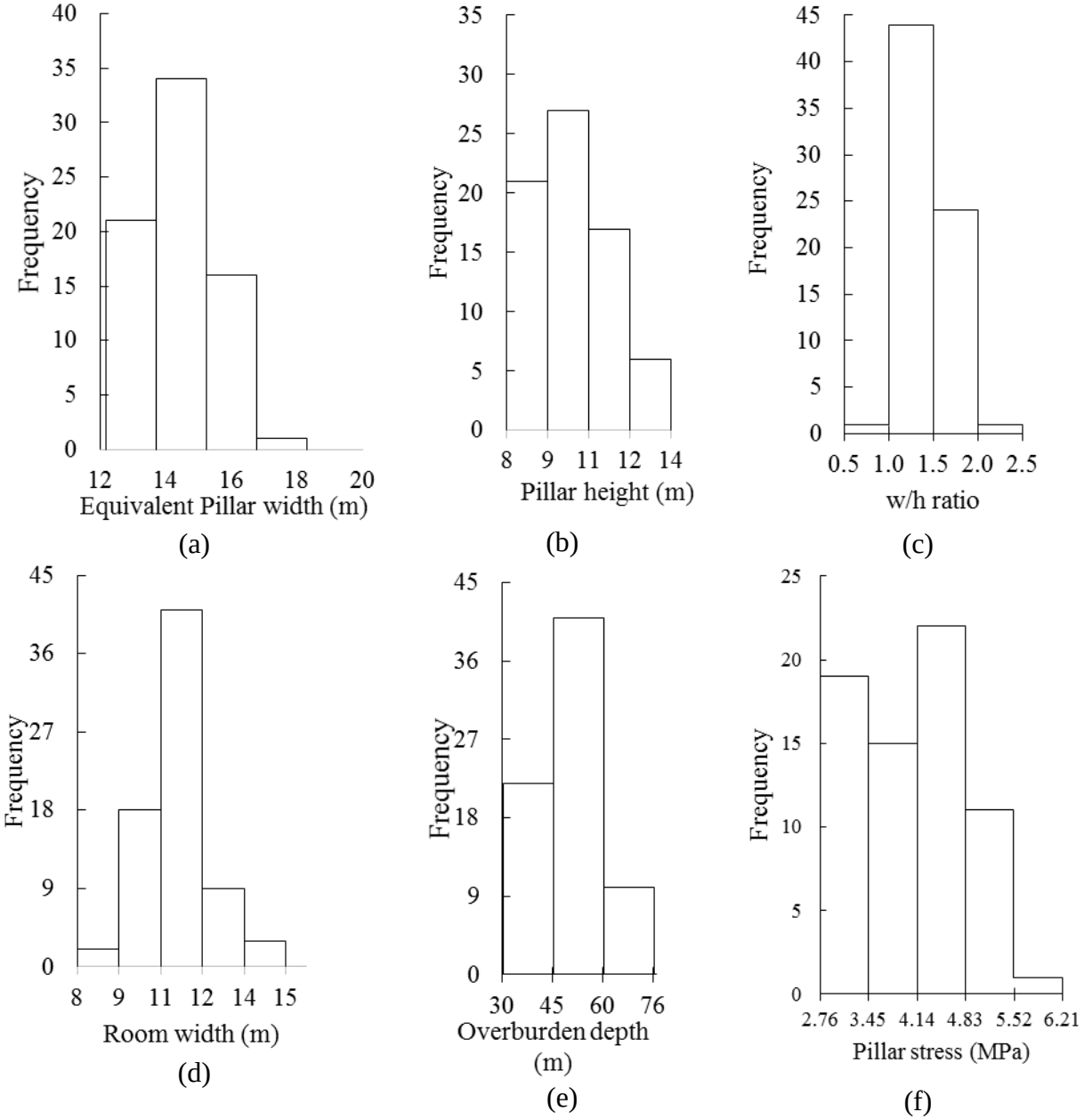

Figure 3.29. Field investigation results: (a) pillar width (b) pillar height (c) w/h ratio (d) room width (e) overburden depth (f) pillar stresses

Figure 3.30. A stable pillar with w/h ratio of 0.95

Figure 3.31. A stable pillar with w/h ratio of 1.17

The fact that pinch out failure occurred in both small and large sized pillars, does not fully support MSHA's hypothesis. For this reason, the researcher will conduct an in-depth study on the causes of pinch out failure and provide explore some promising hypotheses in Section 5.

The occurrence of pinch out failure had been a major challenge at Pattison Sand Mine. Figures 3.32 and 3.33 show a minor and a severe pinch out failure, respectively. Appendix E shows the condition of several pinch out failures at Pattison Sand Mine. To remediate pinch out failures, MSHA recommended bolting and meshing pinch out failure areas. Figure 3.34 shows a bolted, and meshed pinch out failure area. This approach was not very effective in stopping pinch out failures. A better approach was to bolt, mesh and apply shotcrete at pinch out failures areas. Figure 3.35 shows a bolted, meshed and shotcreted pinch out failure area.

Another ground control challenge was how to apply rock reinforcement techniques. The occurrence of pinch out failures wrongly led MSHA to conclude that the pillars do not have adequate strength to support the overburden materials. MSHA suggested the use of metal straps to wrap the entire pillars. Appendix F shows pillar reinforcement techniques recommended by MSHA. MSHA believed that wrapping the pillars with metal straps will provide added confinement to the pillars. Figure 3.36 shows a pillar wrapped with metal straps. However, due to the friable nature of the rock, this reinforcement technique proved ineffective as pillar rib spalling was noticeable particularly in heavily jointed regions. Figure 3.37 shows pillar rib spalling even with metal straps wrapped around the pillar.

The most challenging ground control problem was roof instabilities associated with roof falls. It is important to point out that roof instabilities do not occur in every part of the mine. Roof instabilities are predominant where the roof rock is uncemented St. Peter Sandstone, wet cemented St. Peter Sandstone, or wet thinly bedded shale following the cemented St. Peter Sandstone or limestone.

Another challenge is the interaction between several of these factors (blasting, roof support, and extent of cementing in the St. Peter Sandstone). Take as an example, the pillar and roof span shown in Figure 3.38. In the past, the roof was stable although unsupported (Figure 3.38). The roof rock shown in Figure 3.38 was cemented St. Peter

Sandstone. Currently, the roof and rock falls have triggered the inclusion of roof bolting and wire- meshing to prevent roof instabilities (Figure 3.39).

Depending on the roof rock strength, the impact of ground vibrations from blasting causes the immediate supported roof to develop rock fractures (Figure 3.40) and in some circumstances, rock debris are collected in the wire mesh. For uncemented St. Peter Sandstone roof, the researcher noticed that a few rock debris are collected before blasting (Figure 3.41), and more rock debris are collected in the wire mesh after blasting (Figure 3.42). However, where the roof rock was slightly or heavily jointed cemented St. Peter Sandstone, the impact from blasting caused loose rocks to be collected in the wire mesh as shown in Figures 3.43 and 3.44). Thus, the major challenge is the cost associated with using wires for re-meshing the roof.

Also, where the thickness of the cemented St. Peter Sandstone is less than 0.61 meters and excess pore pressure has developed in the shale bed, the impact of blasting have triggered massive roof falls. Wet or moist roofs resulted from percolation of water in the roof. Water in mine roof layers reduces the bonding between the roof layers (particularly in the vicinity of roof containing shale layers), induces swelling, and results in loss of strength at the rock interfaces. Figure 3.45 shows a massive roof fall resulting from a wet and thin layer of shale which delaminated from limestone. It is important to note that the roof location shown in Figure 3.45 was meshed and bolted prior to the roof fall. This roof failure (Figure 3.45) can be prevented by using long rocks bolts anchored in the overlying limestone layer. Appendix G shows various roof conditions and other associated challenges.

3.6. SUMMARY

The study sites used in this study are Pattison Sand and CGB St. Peter Sandstone mines. Pattison and CGB mines are located at Clayton, Clayton County, Iowa. The CGB mine operated from 1945 to 1982, whereas Pattison Sand mine operated from 2007 to 2016. Thus, the ages of pillars at CGB mine range from 32 to 72 year and 1 to 10 years at Pattison Sand mine.

Figure 3.32. A minor pinch out failure at Pattison Sand Mine

Figure 3.33. A severe pinch out failure at Pattison Sand Mine

Figure 3.34. Bolted and meshed pinch out failed areas at Pattison Sand Mine

Figure 3.35. Shotcrete sprayed on pinch out failed area at Figure 3.68

Figure 3.36. A pillar strap with a metal plate

Figure 3.37. Rock spalling around a pillar wrapped with a metal strap

Figure 3.38. Shotcrete around pinch out failed areas at Pattison Sand Mine

Figure 3.39. Stable roof with bolt and mesh

Figure 3.40. Closer look at roof fractures on uncemented St. Peter Sandstone

Figure 3.41. Few rock debris collected in wire mesh before blasting

Figure 3.42. More rock debris are collected in the mesh after blasting

Figure 3.43. Roof fractures on a slightly cemented St. Peter Sandstone

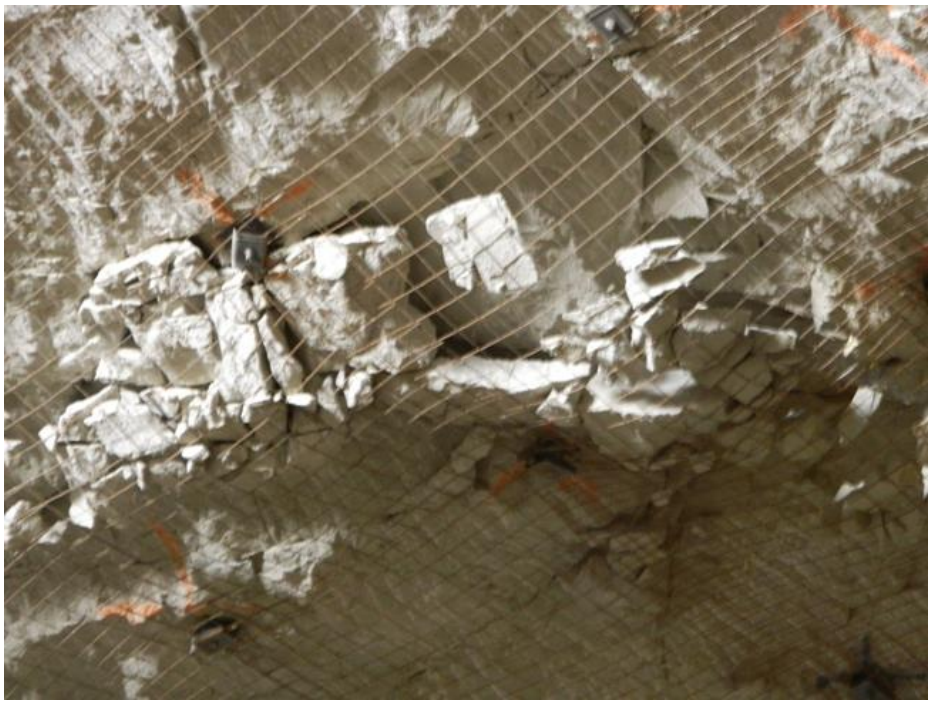

Figure 3.44. Rock debris collected in mesh on roof

Figure 3.45. Roof failure associated with weak shale layer following cemented St. Peter Sandstone

The stratigraphic units at these mines are mainly limestone, shale, and St. Peter Sandstone. The thicknesses of these stratigraphic units are given in Table 3.1. These stratigraphic units are Ordovician formation. The thickness of St. Peter Sandstone varies from 9.14 m to 33.53 m. With an increase of cementing material, the St. Peter Sandstone becomes less friable and passes into quite a hard sandstone. As a result, about 1.22 to 1.83 meter of the upper part of the St. Peter Sandstone is usually cemented.

The researcher used biaxial stressmeters to measure stress changes in St. Peter Sandstone pillars as mine developments progress. Overall, the maximum and minimum principal stress change increased with time as the excavation continued. At 4BO/BP, the maximum principal stress change reached the highest value of 0.23 MPa after 130 blasts in 8 months at Pattison Sand mine. Similarly, the minimum principal stress change reached the highest value of 0.31 MPa after 130 blasts in 8 months at Pattison Sand Mine.

Stress change monitoring at 10BY/BZ site lasted for almost one (1) year. Within this duration, the researcher recorded 64 blasting activities at the mine. At 10BY/BZ site, the maximum principal stress change reached the highest value of 0.10 MPa, while the minimum principal stress change reached -0.14 MPa, for the stressmeter installed 4.57 meters into the pillar. The maximum principal stress change reached the highest value of 0.14 MPa, while the minimum principal stress change reached -0.07 MPa, for the stressmeter installed 7.92 meters into the pillar. The maximum principal stress change appeared to be relatively high at the pillar core compared to pillar rib. However, the opposite is valid in the case of minimum principal stress change. The study suggested further stress change measurement to explain these phenomena. Overall, the measured stress change shows that the pillars at Pattison Sand mine are stable.

The researcher conducted roof displacement monitoring at 4BO/BP and 10BY/BZ sites using Geokon 4450 vibrating wire transducers. Overall, the maximum roof displacement was 0.96 mm and 1.38 mm, respectively, at 4BO/BP and 10BY/BZ sites. The roof displacement results at 4BO/BP indicate a zone of tension (about 1.524 m from the pillar rib) and compression (between 1.524 to 7.3152 m of the roof length). However, the displacement results show that the entire roof at 10BY/BZ is under tension. The fact that roof displacement profiles obtained at 10BY/BZ confirmed qualitatively to

theoretical predictions, offers credibility both to the classical beam theory (Timoshenko, 1940; Sochor, 2001) and the displacement measurements.

Another goal of the displacement monitoring study was to investigate if blasting activities influence roof displacements. The study concluded that blasting influenced roof displacement at 4BO/BP site. Also, the study found that there is a significant difference between the roof displacement profiles prior to and after blasting at 10BY/BZ site. However, there is no significant difference between the displacement profiles prior to and after blasting at the 4BO/BP site.

The researcher conducted numerous field visits to the CGB and Pattison Sand mines. The key purpose of the visits was to conduct extensive field investigations at these mines. The goal of the field investigation was to survey room and pillar geometries that have worked successfully at the CGB and Pattison Sand Mines. This study concluded that pillar designs (dimensions and roof spans) at CGB mine are adequate to support the overburden stresses incident on them. Consequently, a researcher can adopt these room and pillar dimensions under similar overburden stress conditions and for safe and economic pillar design purposes. Also, the study revealed that the roof spans were mostly unsupported. Pinch out failures on some of these pillars did not show any sign of pillar instability. The study has presented the most comprehensive database from which a researcher can derive a realistic pillar design methodology for St. Peter Sandstone.

Underground mining in St. Peter Sandstone formation presents several unique ground control challenges due to its friable nature. Some of these challenges include rock reinforcement techniques, pinch out failures, and roof failures.

4. NUMERICAL MODELING FOR ST. PETER SANDSTONE PILLAR DESIGN

The primary goal of this Section is to use numerical modeling to estimate pillar strength for St. Peter Sandstone. The work then uses this as the basis to inform pillar design in St. Peter Sandstone room and pillar mines.

The researcher conducted the numerical modeling using Fast Lagrangian Analysis of Continua in three dimensions (FLAC 3D). FLAC 3D is capable of modeling elastic and strain softening/hardening behavior of rocks using elasto-plastic constitutive laws.

Numerical models have found increasing application in pillar strength estimation (Lunder and Pakalnis, 1997; Esterhuizen, 2007; Arthur et. al., 2016, Jaiswal et al., 2009; Mohan and Sheorey, 2001). However, the use of numerical models requires the calibration of the model against measured rock mass responses (Hoek and et., 1990; Skiles and Stricklin, 2009). Accordingly, the researcher attempted to calibrate the numerical model in this work with the measured stress change response given in Section 3.3.2. While the use of numerical modeling techniques in design has greatly increased the application of stress change measurement in rocks (Dunnicliff, 1993), numerical methods have previously, to the knowledge of this researcher, never been used to predict stress changes, especially in St. Peter Sandstone room and pillar excavations. Maiden numerical procedure used by the researcher to predict in-situ stress are presented in Section 4.7. The researcher used the model to estimate pillar strength after calibrating it with the measured stress change responses. This study performed a comparative study on the effect of Mohr-Coulomb and Strain Softening Mohr-Coulomb constitutive laws on pillar strength. The researcher developed a pillar strength equation for St. Peter Sandstone room and pillar mines based on the numerical simulation results (Section 4.10). Section 4.11 dealt with the effect of extraction ratio on safety factor at various pillar widths and heights and overburden depths.

The model geometry, in-situ stresses, inputs data, numerical calibration, numerical stability and accuracy, and pillar strength modeling procedures are described in the following Sections.

4.1. NUMERICAL METHODOLOGY

Engineering mechanics problems are modeled using differential equations from physical principles. An investigator can use three techniques to solve engineering mechanics problems: experimental, analytical and numerical. The experimental approach is expensive, time-consuming and cumbersome and usually does not allow much flexibility in parameter variations. An analytical solution of a differential equation is usually a function that satisfies the differential equation and any initial and/or boundary conditions of the problem. Analytical methods are rigorous, their mathematical solutions are exact, and the controlling parameters (geometry and material) can be varied as necessary. The advantage of the analytical method is that it can exactly solve simple geometries of a domain. The major limitation of analytical methods lies in the fact that it cannot deal with complex geometries and material heterogeneity. Also, most differential equations do not have analytical solutions so numerical procedures must be used to find an approximate solution. Numerical methods take advantage of computing capabilities and provide greater flexibility in solving complex problems while handling complex geometries and material heterogeneity with ease. The most common numerical methods for geomechanical modeling are finite element methods, finite difference methods, and boundary element methods. The finite difference method uses the differential form of the governing equations while the finite element and boundary element methods are based on their integral form and require solving a global system of equations.

In this study, the researcher was interested in the stresses at the pillar nodes. The governing equation for the stresses at the nodes can be expressed as a differential equation given in Equation (31). Where σ_i is the stress at node *i*; m_i the mass, v_i is the velocity, t is the time and A is the area.

$$\sigma_i = m_i \frac{dv_i}{dt} \frac{1}{A} \tag{31}$$

The finite difference method is robust in solving differential equations. Hence, the researcher used the finite difference method to compute the stresses in the pillar. In particular, this researcher used the Fast Lagrangian Analysis of Continua in three-

dimensions (FLAC3D), an explicit finite difference software developed by Itasca Consulting Group of USA. FLAC3D is well established for engineering mechanics computations. FLAC3D is capable of simulating the behavior of three-dimensional problems in geotechnical engineering.

FLAC3D finite difference method and finite element method transform differential equations into matrix equations for each element and relate the forces at the nodes to displacement at the node. For an elastic material, the element matrices in FLAC3D are identical to those derived using the finite element method. The researcher used FLAC3D due to the following advantages it offers. Firstly, FLAC3D uses the mixed discretization scheme, which more accurately models plastic flows than the reduced integration scheme used in the finite element method (Marti and Cundall, 1982). In addition, FLAC3D finite difference method is robust in handling any constitutive model without adjustments to the solution algorithm. Several finite element codes need a different solution method for different constitutive models. For the reasons, the principal research investigator purchased FLAC3D software for this research.

4.2. NUMERICAL FORMULATION USING FINITE DIFFERENCE METHOD

FLAC3D is an explicit finite difference numerical modeling software for geotechnical engineering analysis in soil, rocks, and groundwater. FLAC3D explicit finite difference approximation uses the forward difference first order space and time derivative of the variable and assumes linear variation of the variable over finite space and time respectively. If a function (say $f_{i,j}$)) is sufficiently smooth, and the grid is equally discretized as x_1, $x_2 \ldots x_n$, then the forward difference explicit finite difference solution can be approximated using the Taylor expansion series given in Equation (32).

$$f_{i-1,j} = f_{i,j} + \frac{\Delta x}{1!} f_x + \frac{\Delta x^2}{2!} f_{xx} + \ldots\ldots + \frac{f_n{}^n}{n!} \Delta x^n + O(\Delta x^n) \qquad (32)$$

Where: O is the truncation error and $f_x = \frac{\partial f}{\partial x}$, $f_{xx} = \frac{\partial^2 f}{\partial x^2}$, ... $f_n = \frac{\partial^n f}{\partial x^n}$. Truncating Equation (32) to $O(\Delta x^2)$ gives Equation (33). Dividing Equation (33) by Δx, Equation (33) becomes Equation (34).

$$f_{i-1,j} = f_{i,j} + \Delta x f_x + O(\Delta x^2) \tag{33}$$

$$\frac{f_{i-1,j}}{\Delta x} = \frac{f_{i,j}}{\Delta x} + f_x + \frac{O(\Delta x^2)}{\Delta x} \tag{34}$$

Solving for f_x, Equation (34) becomes Equation (35).

$$f_x = \frac{f_{i-1,j}}{\Delta x} - \frac{f_{i,j}}{\Delta x} - \frac{O(\Delta x^2)}{\Delta x} \tag{35}$$

Assuming that $O(\Delta x^2)$ is sufficiently small, then approximation of the first derivative of f_x is given by Equation (36). Equation (36) is called the first order forward difference approximation of f_x, which is what FLAC3D uses to approximate spatial derivatives.

$$f_x = \frac{f_{i-1,j} - f_{i,j}}{\Delta x} \tag{36}$$

Also, replacing Δx by $-\Delta x$, subtracting this new equation from Equation (32), and simplifying, the resulting equation is given by Equation (37). Equation (37) is the first order central difference approximation of f_x. Similarly, Equation (38) can be shown to be the second order central difference derivative of $f_{i,j}$.

$$f_x = \frac{f_{i+1,j} - f_{i-1,j}}{2\Delta x} \tag{37}$$

$$f_{xx} = \frac{f_{i-1,j} - 2f_{i,j} + f_{i+1,j}}{\Delta x^2} \tag{38}$$

Similarly, higher orders of finite difference approximations can be derived by taking higher terms in the Taylor series. FLAC3D uses the central difference approach to approximate the time derivatives.

In FLAC3D, ITASCA (2008) derived the mechanics of the idealized material using laws of motion and constitutive equations of the idealized material. The resulting mathematical expression is a set of differential equations that relate the mechanical and kinetic variables to the particular geometries, material properties at a given boundary and initial conditions. FLAC3D solves the differential equation of motion given by the Cauchy equation shown in Equation (39).

$$\sigma_{ij,j} + \rho b_i = \rho \frac{dv_i}{dt} \tag{39}$$

Where σ_{ij} is the stress tensor; ρ is the mass per unit volume of the medium; $\frac{dv_i}{dt}$ is the material derivative of velocity; and b_i is the body force per unit mass.

For static analysis, the acceleration is equal to zero, hence differential equation of motion given in Equation (39) is written as Equation (40). Equation (40) is the differential equation of equilibrium.

$$\sigma_{ij,j} + \rho b_i = 0 \tag{40}$$

In this analysis, FLAC3D was used to solve the state of stress and deformation of the material near a state of equilibrium using Equation (40).

In general, the relationship between stress and strain for a material is described by it constitutive behavior. For an elastic isotropic material, the strain increments generate stress increments according to the linear and reversible Hooke's law given by Equation (41).

$$\sigma_{ij} = 2G_{ij}\Delta\varepsilon_{ij} + \alpha_2 \Delta\varepsilon_{kk}\delta_{ij} \tag{41}$$

Where α_2 is the material constant and relates to the bulk modulus (K) and shear modulus (G) in Equation (42). New stress values can be obtained from the relation given in Equation (43).

$$\alpha_2 = K - \frac{2}{3}G \tag{42}$$

$$\sigma_{ij}^{N} = \sigma_{ij} + \Delta\sigma_{ij} \tag{43}$$

For a plastic Mohr-Coulomb material, the stress is controlled by a non-associated flow rule for shear failure and associated flow rule for tensile failure. The incremental expression of Hooke's law in terms of the generalized stress and stress increments given in Equations (44) to (46) . Equations (44) through (46) are expressed as:

$$\Delta\sigma_1 = \alpha_1\Delta\varepsilon_1^{e} + \alpha_2(\Delta\varepsilon_2^{e} + \Delta\varepsilon_3^{e}) \tag{44}$$

$$\Delta\sigma_2 = \alpha_1\Delta\varepsilon_2^{e} + \alpha_2(\Delta\varepsilon_1^{e} + \Delta\varepsilon_3^{e}) \tag{45}$$

$$\Delta\sigma_3 = \alpha_1\Delta\varepsilon_3^{e} + \alpha_2(\Delta\varepsilon_1^{e} + \Delta\varepsilon_2^{e}) \tag{46}$$

Where: σ_1, σ_2 and σ_3 are maximum, intermediate and minimum principal stress respectively, such that given in Equation (47). ε_1, ε_2, and ε_3 are the maximum, intermediate and minimum principal strain vectors; and α_1 and α_2 material constants defined in Equations (48) and (49).

$$\sigma_1 \le \sigma_2 \le \sigma_3 \tag{47}$$

$$\alpha_1 = K + \frac{4}{3}G \tag{48}$$

$$\alpha_2 = K - \frac{2}{3}G \tag{49}$$

The failure envelope $f(\sigma_1, \sigma_3) = f^s$ is defined by Equation (50).

$$f^s = \sigma_1 - \sigma_3 N_\phi + 2c\sqrt{N_\phi} \tag{50}$$

Where: c is the cohesion, ϕ is the friction angle; and N_ϕ is given by Equation (51).

$$N_\phi = \frac{1+\sin\phi}{1-\sin\phi} \tag{51}$$

The tensile strength of the material cannot be greater than σ_3. The Maximum tensile strength is given in Equation (52).

$$\sigma^t_{\max} = \frac{c}{\tan\phi} \tag{52}$$

A flow rule defines plastic straining. This is given by Equation (53).

$$\Delta(\varepsilon)_p = \lambda \frac{\partial F}{\partial \sigma} \tag{53}$$

Where

$\Delta(\varepsilon)_p$: Increment vector of plastic strain

$\frac{\partial F}{\partial \sigma}$: Direction of the plastic strain

λ: Magnitude of plastic strain

The Mohr-Coulomb model can be defined with non-associated flow rules. The non-associated flow rule is similar to the conventional Mohr-Coulomb model, where the Mohr-Coulomb properties are assumed to remain constant. With the associated flow rule,

the investigator can define the cohesion, friction angle, and dilation as piecewise-linear functions of softening or hardening parameter measuring the plastic shear strain. A piecewise-linear softening law for the tensile strength can also be prescribed in terms of another hardening parameter measuring the plastic tensile strain.

In a softening or hardening rule, the yield function in relation to the effective plastic strain is given by Equation (54).

$$K_{effp} = \sigma_y + K\varepsilon_{effp} \tag{54}$$

K_{effp} : Effective softening and hardening slope
σ_y : Initial yield stress
K : softening or hardening slope

The total strain is the sum of the elastic strain (ε^e) and plastic strain (ε^p) components given by Equation (55).

$$\Delta\varepsilon = \Delta\varepsilon^e + \Delta\varepsilon^p \tag{55}$$

The elastic strain is related to the stress by Equation (56).

$$\Delta\varepsilon^e = [E]^{-1}.\Delta\varepsilon \tag{56}$$

Taking the elastic and plastic components, the Equation (56) becomes Equation (57).

$$\Delta\varepsilon^e = [E]^{-1}.\Delta\varepsilon + \lambda\frac{\partial F}{\partial\sigma} \tag{57}$$

The elastic-plastic stress and strain increments is given by Equation (58).

$$\Delta\varepsilon^e = [E]_{ep}.\Delta\varepsilon \tag{58}$$

Where, $[E]_{ep}$ is the elasto-plastic stiffness matrix. During elasto-plastic analysis, $[E]_{ep}$ is updated in the finite difference solution.

The boundary conditions in this work included fixing the displacement in the vertical, and horizontal axes and placing a constant velocity on top of the model until the

pillar failed. Initial stresses were assumed to relate the overburden depth given in Equations (59) and (60). This constitutes the initial state of the numerical scheme.

Simulation in FLAC3D involves few steps. The grid defines the geometry of the problem. Next, the investigator defines the constitutive behavior and material properties of the materials involved. Boundary and initial conditions define are the displacements and the in-situ state. An initial equilibrium state is calculated for the model. The investigator can then make a change (excavation or changing boundary conditions, etc.), and FLAC3D computes the resulting responses. FLAC3D numerical solution involves explicit time marching method to solve algebraic equations. The solution is reached after a series of computational steps. The main limitation of FLAC3D is linear simulations run more slowly than equivalent finite element programs. FLAC3D is ineffective to model beams represented as solid elements rather than structural elements or problems that contain large disparities in elastic moduli or element sizes

4.3. MODEL GEOMETRY

The researcher used FLAC 3D to create models of St. Peter Sandstone pillars with width to height ratios ranging from 0.5 to 3.0, at an interval of 0.5. The researcher varied the pillar height from 7.62 to 18.29 m. These pillar heights were typical in the study area. The researcher maintained an extraction ratio of 68% throughout the initial simulation experiments to ensure that all pillars are subjected to the same average pillar stress. (The effect of extraction ratio on safety factor is discussed in Section 4.11.) This extraction ratio represents the average extraction ratio at the CGB mine. Consequently, the room width varied as the w/h ratio increased. For pillars with the same w/h ratio, the room width varied as the pillar height increased. The researcher modeled only one-quarter of the pillar and half of the room width to take advantage of the symmetry of the problem. The researcher maintained zone aspect ratio of unity for the pillar elements to increase the accuracy of the simulation results.

To reduce computational time, the researcher considered only five overlying strata, typical of the study area, having obtained the thickness of the various overlying strata from drill logging data and a topographic map. Figure 4.1 shows model geometry and thicknesses of the overlying strata for a pillar with w/h ratio of 1.5.

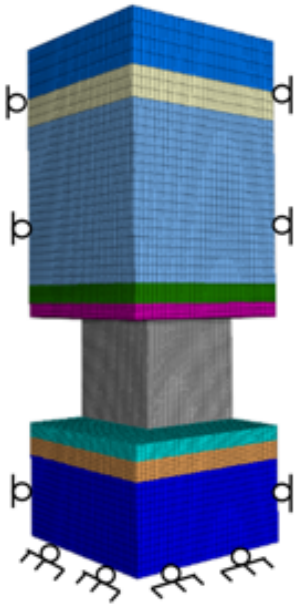

LEGEND		
Color	Rock Layers	Thickness of layers(m)
	Limestone	4.267
	Shale	2.438
	Limestone	13.716
	Shale	1.524
	Sandstone	1.219
	St.Peter Sandstone	9.144
	St.Peter Sandstone	1.219
	Shale	1.524
	Limestone	7.000

Figure 4.1. A quarter model and mesh for w/h ratio = 1.5

4.4. IN-SITU STRESSES

In the model, the researcher loaded the pillars by the weights of the overlying strata. Additional external vertical loads were also applied at the top of the pillars to account for the weight of the overlying rocks not included in the model. The researcher assumed the average vertical and horizontal in-situ stresses based on Haimson (1978). Haimson (1978) measured the in-situ vertical and horizontal stresses in the United States. The researcher believes that the in-situ stresses reported by Haimson (1978) are more representative, in the United States, than that collated worldwide by Hoek and Brown (1980).

According to Haimson (1978), the average in-situ vertical and horizontal stresses are given by Equations (59) and (60), respectively. Where σ_z is the vertical stress in the z-direction; H is the depth of the overburden materials; and σ_x and σ_y are the average horizontal stresses in the x and y-directions, respectively.

$$\sigma_z = 0.025H \tag{59}$$

$$\sigma_x = \sigma_x = 4.90 + 0.02H \tag{60}$$

4.5. INPUT DATA

The researcher obtained the physical and mechanical strength properties of the pillar, roof and floor rock from laboratory testing and literature (Bagherieh, 2015). The researcher modeled the roof and floor strata as elastic materials. The researcher used the Mohr-Coulomb constitutive law to model the pillar rock. The researcher used a friction angle of 60^o for St. Peter Sandstone. For a Mohr-Coulomb material, Equation (61) relates the cohesion (C) to the friction angle (ϕ) and uniaxial compressive strength (UCS). Table 4.1 summarizes the physical and mechanical properties of the rock masses involved in the model.

$$C = \frac{UCS(1 - Sin\phi)}{2Cos\phi} \tag{61}$$

Table 4.1. Physical and mechanical properties of rock mass

Parameter	St. Peter Sandstone	Sandstone	Limestone	Shale
UCS (MPa)	5.40	52	76	4.02
Density(Kg/m^3)	2030	2245	2563	2100
Bulk Modulus (GPa)	0.56	11.50	24.50	0.31
Shear Modulus (GPa)	0.72	9.70	14.70	0.34
Cohesion (MPa)	0.72	-	-	-
Residual cohesion (MPa)	0.00	-	-	-
Friction angle(degrees)	60.00	-	-	-
Residual Friction angle (degrees)	45.00	-	-	-
Tensile Strength (MPa)	0.54	-	-	-

4.6. NUMERICAL STABILITY AND ACCURACY

The reliability of a numerical method to predict results is dependent on convergence, stability, consistency and the magnitude of the error. In FLAC3D, numerical consistency, stability, accuracy and fast convergence of the numerical simulation depends on the mesh quality and time step used by a researcher (Abbasi et al., 2013; Knupp, 2007). The numerical solution is consistent if a reduction in the mesh sizes and time step reduces the truncation error (Ryanben'kii and Tsynknov, 2006). The

researcher computer the round-off errors (loss of precision due to rounding of decimal quantities).

The numerical stability and convergence of the explicit finite difference approach in FLAC3D depend on the mesh size and the rock stiffness (Itasca, 2013, Hosseini, 2015). In FLAC3D, the numerical time steps (Δt) sufficient to reach numerical stability is given in Equation (62) (Itasca, 2013; Hosseini, 2015). A FLAC3D numerical solution converges when the numerical time steps and the critical time step (Δt_c) are equal (Equation 63). Where Δx is the mesh size, ρ is the density, and K and G are the bulk and shear modulus, respectively. Thus, in FLAC3D, a numerically stable solution is a sufficient condition for convergence (Itasca, 2013). In FLAC3D, numerical stability and convergence are controlled by the mechanical ratio, in that, by default, when the mechanical ratio reaches 0.00001, FLAC3D solution is numerically stable and converges (Itasca, 2013, Hosseini, 2015). This is also a necessary and sufficient condition to reach near equilibrium conditions in FLAC3D. (Itasca, 2013)

$$\Delta t < \frac{\Delta x}{\sqrt{\frac{K + \frac{4G}{3}}{\rho}}} \tag{62}$$

$$\Delta t = \Delta t_c = \frac{\Delta x}{\sqrt{\frac{K + \frac{4G}{3}}{\rho}}} \tag{63}$$

One way to assess the accuracy of any numerical analysis is to solve a numerical problem and compare its solution to analytical solutions. Accordingly, the researcher computed the average pillar stress using FLAC3D and compared the results to the analytical solution (using the tributary area method).

In the numerical analysis, the researcher varied the mesh size and time step to determine their influence on the truncation error due to space and time. Also, in the numerical analysis, the researcher established the round-off error.

For a regular pillar uniformly loaded by its overburden weight, the average pillar stress was computed using the tributary area method given in Equation (2).

$$\sigma_P = 0.025H\,\frac{(w+l)^2}{w^2} \tag{2}$$

Where *w*, is the width of the pillar, *l* is the room width and *H* is the overburden depth. For example, for a regular pillar with *w* = 9.14 m, *l* = 7.02 m, and overburden stress of 0.76 MPa, the computed average pillar stress using Equation (2) was 2.381 MPa.

The researcher generated a numerical model of similar mining dimensions and overburden loading condition. In the model, the researcher restricted displacement of the four vertical symmetry planes in the normal direction (Figure 4.1). Also, the researcher fixed the bottom of the model to restrict movement in the vertical direction. The researcher then applied vertical and horizontal in-situ state of stress to the model. The researcher varied the mesh sizes while maintaining an aspect ratio of one in all these numerical analysis. The researcher defined a FISH (an internal programming language in FLAC 3D) function to determine the average pillar stress in each model. The researcher then solved this problem using FLAC3D. Table 4.2 compares the analytical solution to FLAC3D solution.

The reader can see from Table 4.2 that as the mesh size and numerical step time decreases, the truncation error also decreases. The minimum and maximum truncation errors are -1.63% and 0.92%, respectively. In this numerical analysis, the researcher recorded a round-off error of 0.0000001% of the predicted average pillar stress. The fact that the truncation and round-off errors are within the acceptable limit (Abbasi et al., 2013), provide credibility of the FLAC3D numerical solutions (Palais and Palais, 2009). The researcher deduced that FLAC3D numerical solutions obtained in this study are consistent, stable, accurate and converges to the actual solution within an acceptable margin of error. Based on this sensitivity analysis and the choice of the discretization limits, the researcher concluded that there is high confidence in FLAC3D numerical results.

The reader can see in Table 4.2 that, the average pillar stress at a mesh size of 0.61 m closely compared favorably with the analytical solution (tributary area method). However, as the pillar mesh size increased beyond 0.61 m, the average pillar stress remained practically the same even though the model slightly overestimated the pillar stress (error < 1%). From Table 4.2, the reader can see that for a mesh size of 0.30 m, the numerical model underpredicted the pillar stress by less than 2%. Mark (1987) used a two-dimensional finite element model to determine the accuracy of tributary area prediction of pillar stress. Mark's model predicted average pillar stresses that were 2-8% less than the tributary area predictions. This study further confirms that the tributary area method generally provides a satisfactory estimate of the pillar stress in a room and pillar system. However, Esterhuizen et al. (2011) have reported that the tributary area method predicts the upper limit of the average pillar stress. The researcher believes that the error corresponding to a mesh size of 0.30 m is consistent with Mark (1978) findings, hence to be conservative, the researcher used a mesh size of 0.30 m throughout the numerical modeling exercise.

Table 4.2. Comparison of analytical and numerical methods

Time step	Mesh size (m)	Average pillar stress (MPa)		Truncation Error
		Analytical method	Numerical method	
0.0003528	0.3	2.381	2.342	-1.63%
0.0007056	0.61	2.381	2.386	0.19%
0.0010583	0.91	2.381	2.397	0.68%
0.0014111	1.22	2.381	2.403	0.91%
0.0017639	1.52	2.381	2.403	0.92%

4.7. CALIBRATING THE GLOBAL MODEL

In this Section, the researcher calibrated the numerical model with the measured in-situ stress change response during mine excavations. The researcher generated a 100 m by 100 m numerical model, using FLAC3D. In the model, the researcher restricted displacement of the four vertical symmetry planes in the normal direction. Also, the

researcher fixed the bottom of the model to restrict movement in the vertical direction. The researcher then applied vertical and horizontal in-situ state of stress to the model. The researcher stepped the numerical model until the maximum unbalance forces were within an acceptable limit. At this point, the researcher set up the model in such a way that after excavating each stage, the model was stepped to equilibrium. Table 4.3 summarizes the calibration procedure. Figure 4.2 shows the excavation stages. During the simulation, the researcher monitored the maximum principal stress at the mid-zone at the mid-height location of the middle pillar (Figure 4.3). The researcher obtained a history of the maximum principal stress after each excavation stage run. The maximum principal stress change was the maximum principal stress from the prior stage minus the maximum principal stress following that stage. Table 4.4 summarizes the results of the calibration exercise. The total measured stress change, in the field, was 0.23 MPa. The reader can see in Table 4.4 that the total modeled stress change was 0.25 MPa. This researcher used the same numerical procedure to model the stress change during mining excavations at 10BY/BZ. The predicted stress change was 0.13 MPa, which compared satisfactorily with a measured stress change of 0.14 MPa (Table 4.5).

The researcher concluded that the measured stress change and the predicted stress changes are within acceptable levels. The researcher used the calibrated model to estimate the strength of St. Peter Sandstone pillars.

Table 4.3. Simulation procedure used for the calibration

Steps	Brief of 3D FDM Simulation
0	Simulate in-situ gravity stress in ground
1	Excavate stage 1 and step to equilibrium
2	Excavate stage 2 and step to equilibrium
3	Excavate stage 3 and step to equilibrium
4	Excavate stage 4 and step to equilibrium
5	Excavate stage 5 and step to equilibrium
6	Excavate stage 6 and step to equilibrium
7	Excavate stage 7 and step to equilibrium
8	Excavate stage 8 and step to equilibrium
9	Excavate stage 9 and step to equilibrium

Table 4.4. Results of stress change measured

Stages	Max. Principal Stress (MPa)	Stress Change (MPa)
1	2.68	-
2	3.00	0.32
3	2.87	-0.13
4	2.66	-0.21
5	2.85	0.19
6	2.87	0.02
7	2.89	0.02
8	2.91	0.02
9	2.93	0.02
Total	-	**0.25**

Table 4.5. Results of stress change measured at 10BY/BZ

Stages	Maximum principal stress (MPa)	Stress change (MPa)
A1	2.56	-
A2	2.47	-0.09
A3	2.65	0.18
A4	2.66	0.01
A5	2.67	0.02
A6	2.69	0.01
A7	2.70	0.01
Total		0.135

4.8. NUMERICAL MODELING OF PILLAR STRENGTH

Brady and Brown (1985) defined pillar strength as the maximum resistance of a pillar to axial compression. Pillar strength is estimated in a way similar to laboratory determination of uniaxial compressive strength of the rock. As the reader saw in Section 3, St. Peter Sandstone behaves as a strain softening material with a total loss of cohesion and a drop in friction angle. The researcher maintained a residual friction angle equal to one-quarter of the assumed friction angle. The researcher coded a piecewise user-defined linear function in FLAC3D to soften St. Peter Sandstone as the plastic strain increases.

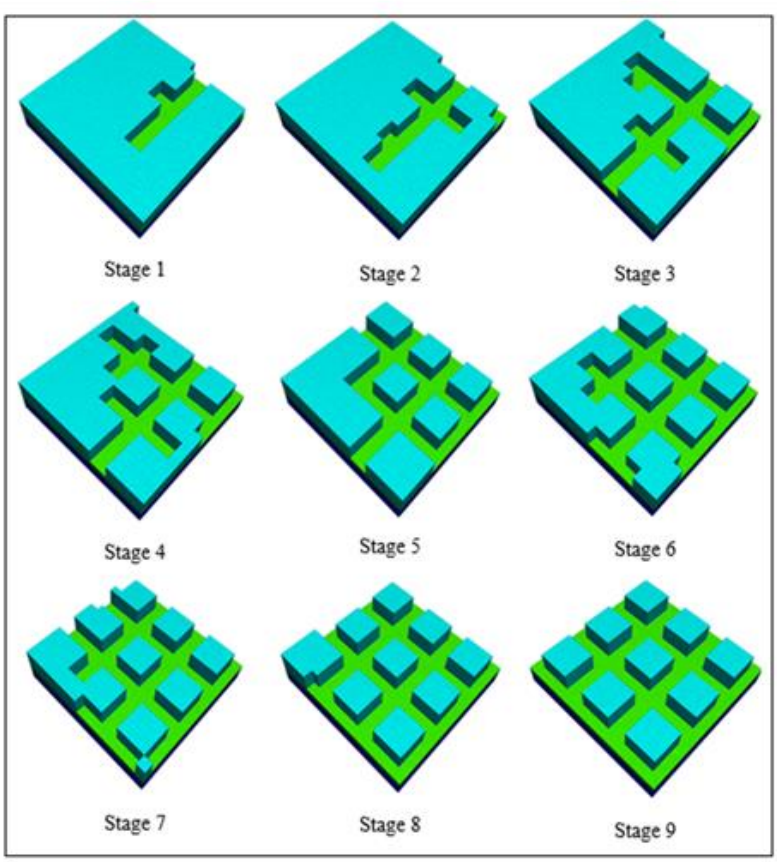

Figure 4.2. Excavation sequence used for modeling

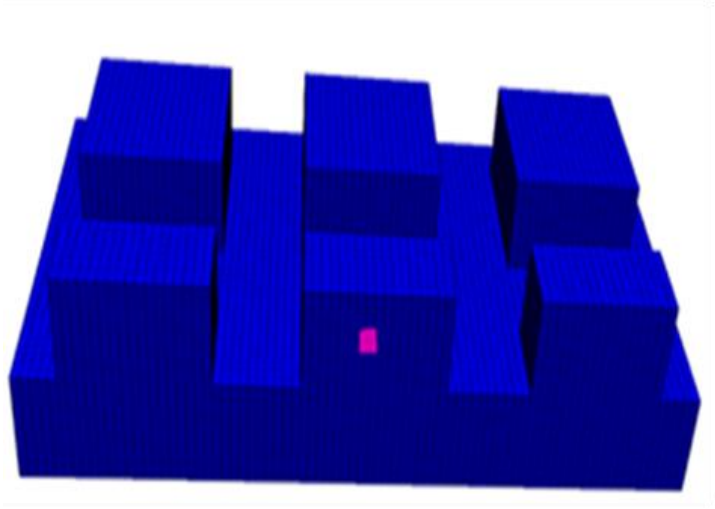

Figure 4.3. Stress change monitoring location indicated in pink

The researcher maintained a residual friction angle equal to one-quarter of the assumed friction angle. The researcher coded a piecewise user-defined linear function in FLAC3D to soften St. Peter Sandstone as the plastic strain increases. He then assumed elastic constitutive law to model the roof and floor strata and the elastoplastic constitutive laws for the pillar. Table 4.1 provides details of the physical and mechanical input parameters. Section 4.3 presents vertical and horizontal stresses applied to the model.

In the model, the researcher restricted displacement of the four vertical symmetry planes in the normal direction and fixed the bottom of the model to restrict movement in the vertical direction. He then applied vertical and horizontal in-situ state of stress to the model, as discussed in section 4.5. The researcher stepped the numerical model until the maximum unbalance forces was less than 0.001% of the average applied gridpoint force. This also allows the kinetic energy of the mesh to damp out and to generate in-situ stresses within the model. At this point, the researcher excavated the roadway (room width) leaving only the pillar supporting the overburden load. To estimate the strength of the pillar, the researcher fixed the top of the model in the vertical direction and applied a constant velocity on top of the model to generate increasing vertical loads on the pillar. The magnitude of the velocity was 10^{-5} m/s. The researcher used this value throughout the simulation exercise. The researcher monitored the average pillar stress, using FISH, and the axial strain in the pillar (computed as the mean roof-to-floor displacement over the entire pillar area divided by the pillar height). He obtained the complete stress-strain behavior of the pillar. Figure 4.4 shows a stress-strain behavior of a pillar with a w/h ratio of 1.0. The peak average pillar stress thus represents the pillar strength. Several researchers have used this numerical procedure to estimate the pillar strength for hard rocks (Lunder and Pakalnis, 1997; Esterhuizen, 2007; Arthur et. al., 2016), and coal (Jaiswal et al., 2009; Mohan and Sheorey, 2001).

The researcher used this modeling procedure to determine the pillar strength of pillars with different w/h ratios and strength properties. Section 4.9 presents the results of the modeling study.

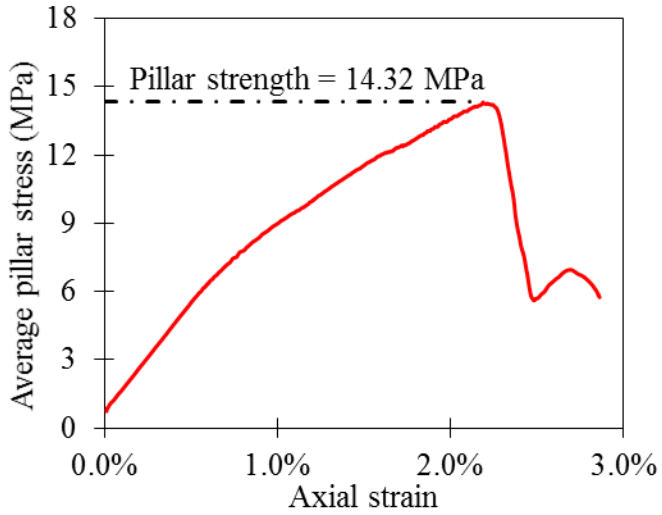

Figure 4.4. Stress-strain behaviour of a pillar with w/h ratio =1.0

4.9. NUMERICAL MODELING RESULTS

The researcher used the modeling procedure presented above to estimate the pillar strength of St. Peter Sandstone pillars. He estimated pillar strength using Mohr-Coulomb (MC) and Strain Softening Mohr-Coulomb(SSMC) constitutive laws. In the strain-softening Mohr-Coulomb model, the plastic strength properties degrade as plastic strain increases. In the conventional Mohr-Coulomb model, the plastic strength properties do not change throughout the simulation. The plastic shear strength properties the researcher used are cohesion and friction angle. This work uses the numerical modeling results to examine the effect of width to height (w/h) ratios on pillar strength as well as the effect of plastic strain, cohesion, and friction angle on pillar strength and safety factor for pillar design.

4.9.1. Effect of Width-to Height (w/h) Ratio on Pillar Strength. This work used the numerical model to examine the effect of w/h ratios on pillar strength for the St. Peter Sandstone for SSMC and MC models. Figure 4.4a compares the modeling results of the MC model to the SSMC model for w/h ratios ranging from 0.5 to 3.0.

In general, as the width to height ratio increased, the pillar strength also increased (Figure 4.4). This is because as w/h ratio increases, there is a greater tendency for the pillar to generate more pillar confinement and, hence, higher pillar strength.

The pillar strength values for the MC model is relatively high compared to that of SSMC model. Thus, the results show that the MC model predicts the upper limit of the pillar strength. This is because, in the Mohr-Coulomb model, the plastic strength properties do not change throughout the simulation compared to SSMC model where the plastic strength properties degrade as plastic strain increases. For example, the input parameters presented in Table 4.1 resulted in a pillar strength of 14.32 MPa for a square pillar with w/h ratio of 1 based on the SSMC model, and this is about 68% of the pillar strength for the MC model.

Figure 4.5b shows the influence of w/h ratio on the ratio of pillar strengths of the MC to SSMC models. As shown in Figure 4.5b, the ratio of pillar strength based on the MC model to the SSMC model is about one and half times for a w/h ratio of 1 and up to almost seven times for a w/h ratio of 3. Thus, the pillar strength based on the SSMC model is more conservative compared with that predicted using the MC model.

4.9.2. Effect of Pillar Size on Pillar Strength. This study used the numerical model to investigate size effect (pillars having the same w/h ratio) on pillar strength for the St. Peter Sandstone using SSMC and MC models. Figure 4.6 shows the influence of size effect on pillar strength for the MC and SSMC models.

In general, at the same w/h ratio, the pillar strength decreases as pillar size increases (Figure 4.6). This is because at the same w/h ratio, as pillar size increases, the pillar height also increases. This finding is consistent with the effect of specimen or pillar size on strength reported for coal (Bieniawski, 1968), diorite (Pratt et al., 1972), iron ore (Jahns, 1966), sandstone (John, 1972), limestone, marble, basalt, gabbro, and granite (Hoek and Brown, 1980). The results show that at a w/h ratio of one, the pillar strength predicted by the MC model is about one and a half times more than the pillar strength predicted by the SSMC model (Figure 4.6).

Overall, the pillar strength based on the SSMC model predicts the least pillar strength. Thus, the SSMC model presents the worst case prediction of the pillar strength. Worst case predictions based on the SSMC model is a way to compensate for uncertainties and implement conservative designs.

For these reasons, this study uses the SSMC model. Ozbay and Rozgonyi (2003) also reached a similar conclusion that the strain softening Mohr Coulomb model was more realistic in modeling coal pillar strength compared with Mohr Coulomb model.

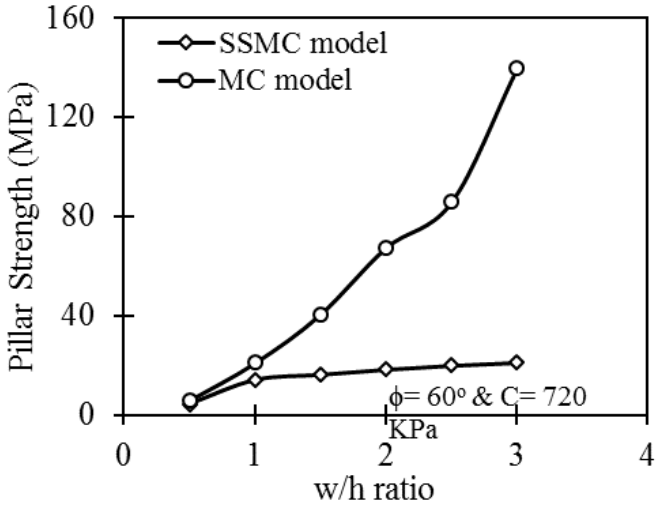

(a)

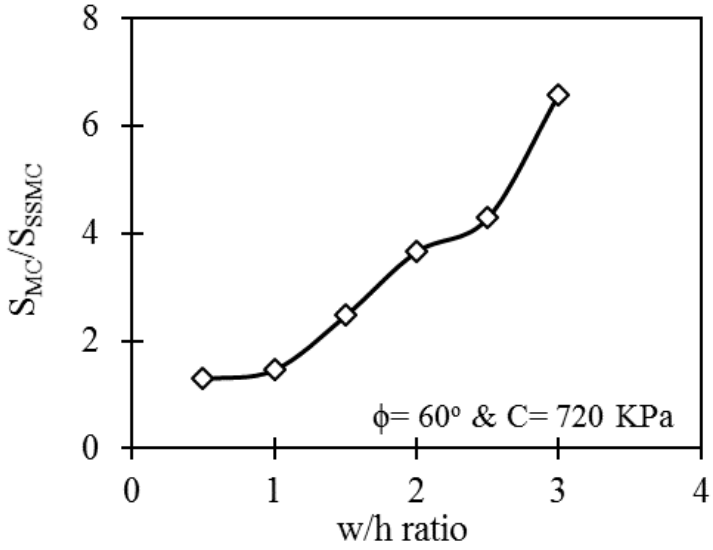

(b)

Figure 4.5. Comparing SSMC and MC models in estimating pillar strength: (a) raw results; (b) ratio of pillar strength estimates

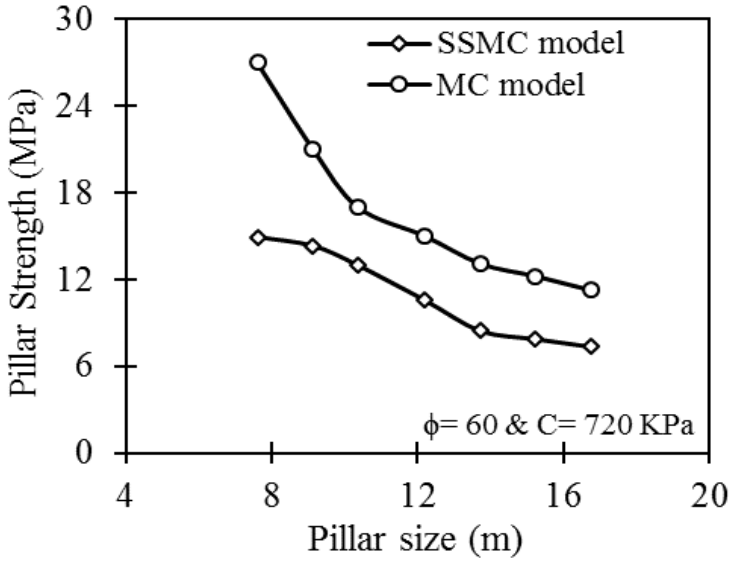

Figure 4.6. Influence of w/h ratio on pillar strength

The SSMC model requires a user-defined function that defines the rate at which cohesion and friction angle drop as plastic strain increases. Pillar strength based on the SSMC model is sensitive to several parameters including, but was not limited to, size and shape effects. Size and shape effects are also sensitive to cohesion, friction angle, and plastic strain.

4.9.3. Effect of Plastic Strain, Cohesion and Friction Angle. This researcher studied the effect of plastic strain, cohesion and friction angle on pillar strength. Figure 4.7 shows the effect of w/h ratio and cohesion on pillar strength. It is established in Section 4.9.1 that as w/h ratio increases the pillar strength also increases. The reader can see from Figure 4.7 that, as w/h ratio increases the pillar strength increased with increasing cohesion. This is because as cohesion increases, the degree of cementation in the pillar increases, hence the pillar strength also increases.

This study investigated the effect of plastic strain on pillar strength for different w/h ratios. Figure 4.8 shows the effect of w/h ratio on pillar strength at different plastic strains for the cohesion of 432 KPa, 576 KPa, and 720 KPa. The reader can see from Figure 4.8c that at a plastic strain of 0.05, the pillar strength increased to up to a w/h ratio of 1 and then it decreased slightly.

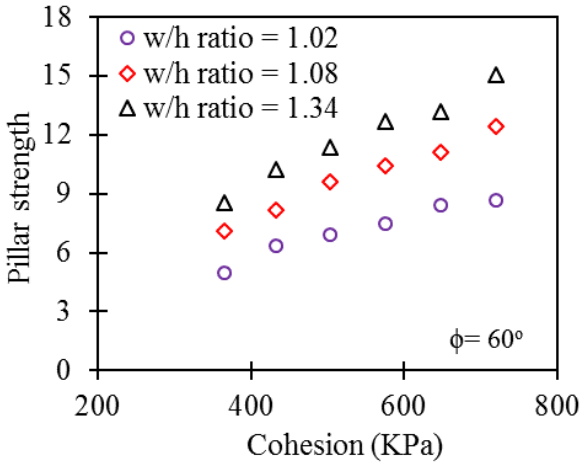

Figure 4.7. Influence of w/h ratio and cohesion on pillar strength

However, at a plastic strain of 0.05, the pillar strength increased until after w/h ratio of 1, then it remained constant (Figure 4.8b). The researcher obtained similar trends for a plastic strain of 0.05 in Figure 4.8a.

In general, the pillar strength increased gradually at a plastic strain of 0.10 and increased rapidly as the plastic strain increased. Thus, the choice of plastic strain can affect the pillar design mechanics. For example, literature reported that, as w/h ratio increases, pillar strength also increases and vice versa. However, this argument is not true for plastic strains of 0.05 and 0.10, as discussed above. The researcher concludes that modeling pillar strength using the SSMC model is very sensitive to plastic strain, hence the pillar design modelers must pay attention to the choice of the plastic strain.

Also, the reader can see that, at a plastic strain of at least 0.15, the pillar strength increases monotonically as w/h ratio increases. This is what we expect with increasing w/h ratio. In other words, a plastic strain of 0.15 presents the minimum worst-case pillar strength predictions that produce the expected strength behavior with varying w/h ratios. In this study, the researcher assumed that the strength properties of St. Peter Sandstone is isotropic. In addition, the initial in-situ vertical and horizontal stresses were based on average vertical and horizontal stresses measured in the United States (Haimson, 1978). These assumptions introduce uncertainties in the pillar strength predictions. For these reasons, for conservative pillar design, the researcher believes a plastic strain of 0.15 is reasonable for estimating pillar strength for St. Peter Sandstone. Pillar design based on a

plastic strain of 0.15 is conservative, practical, and acceptable within economic and safety constraints (see Section 4.11). For these reasons, the researcher limited the analysis to a plastic strain of 0.15.

Figure 4.9 shows the results of simulations to investigate the effect of pillar size and plastic strains for a fixed w/h ratio, on pillar strength. As aforementioned, the results show that, for a w/h ratio of unity, the pillar strength decreased as pillar size increased. This trend was the same for all the cohesion values and plastic strains simulated in this work. In laboratory determination of specimen size effect on strength, this decreasing trend is attributed to the presence of geologic discontinuities including bedding planes, cleats, cracks and inclusions in that size effect becomes less pronounced as the specimen size becomes larger and vice versa. However, in numerical modeling (since there are no discontinuities), this decreasing strength as pillar size increases maybe attributed to the increasing pillar height at the same w/h ratio.

Figures 4.10 shows the effect of pillar size on pillar strength for different cohesion and friction angles. The results show that as friction angle increased, the pillar strength also increased. Also, for the same pillar size as cohesion increases, the pillar strength also increases. Furthermore, for the same w/h ratio, as pillar size, friction angle and cohesion increased, the pillar strength also decreased.

4.10. DERIVATION OF PILLAR STRENGTH EQUATION

One of the goals of this work was to determine an empirical pillar strength criteria that can be used by engineers in St. Peter Sandstone room & pillar mines. Such empirical pillar strength criteria are usually determined by fitting a curve to field data (Salamon and Munro, 1967). The empirical models relate pillar strength to material cohesion, pillar height, and pillar w/h ratio. This researcher fitted an empirical equation (Equation 64) to the 72 modeled pillar cases surveyed at the CGB mine at different strength and deformation parameters using linear regression techniques.

$$S_P = \beta_O + \beta_1 C - \beta_2 h\left[A + B(w/h)\right] \tag{64}$$

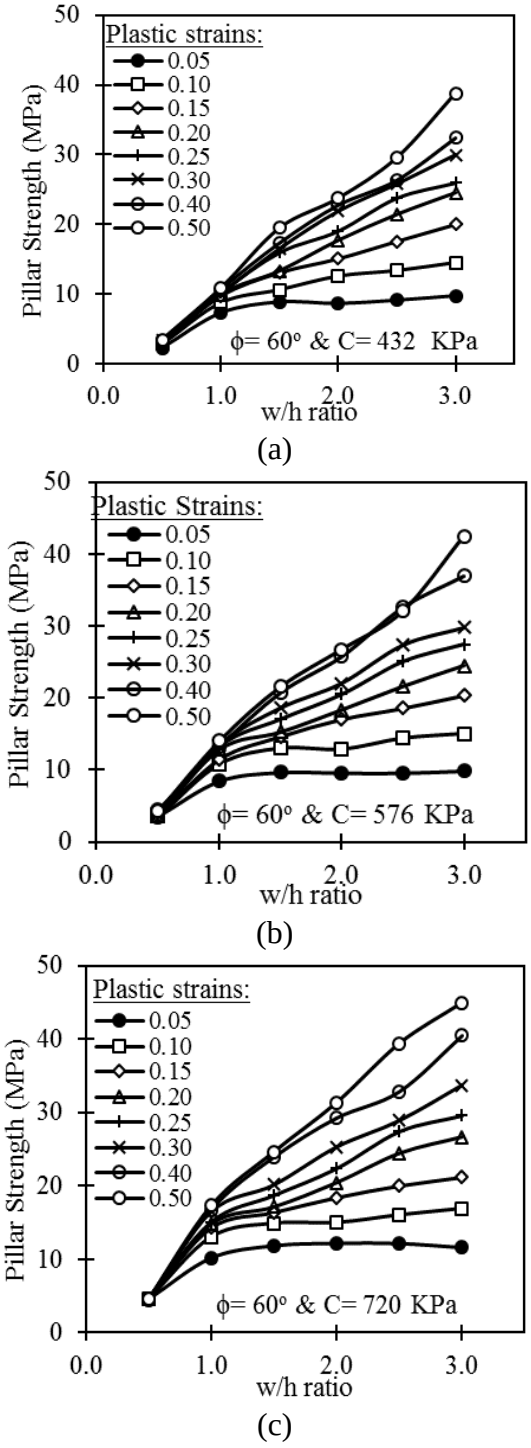

Figure 4.8. Influence of plastic strain and w/h ratio on pillar strength at friction angle of 60º and cohesion of: (a) 432 KPa, (b) 576 KPa, (c) 720 KPa

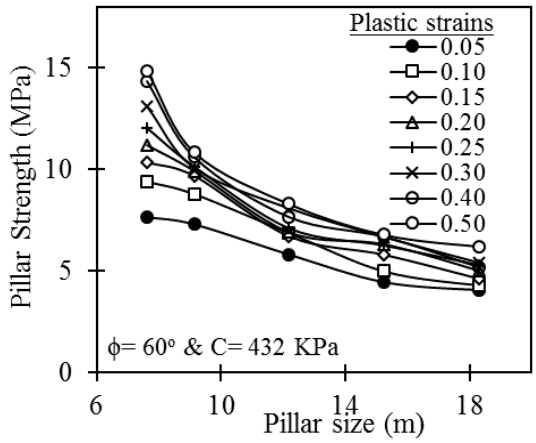

(a)

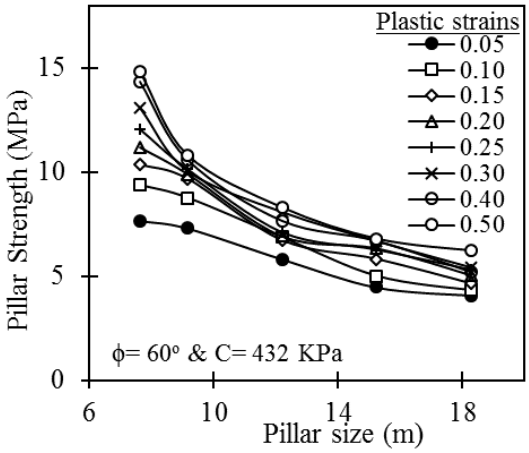

(b)

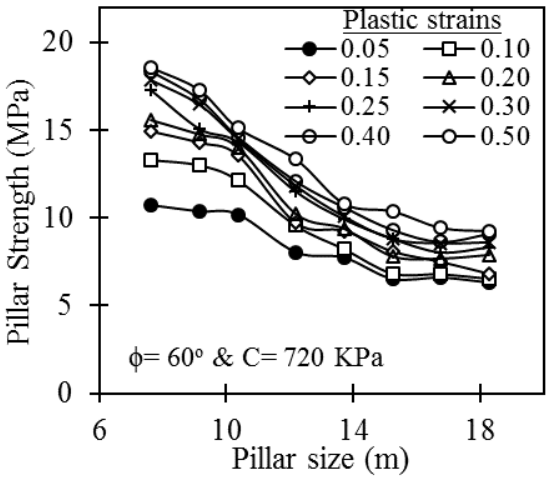

(c)

Figure 4.9. Influence of pillar size and plastic strain on pillar strength for friction angle of 60° and cohesion of: (a) 432 KPa, (b) 576 KPa, and (c) 720 KPa

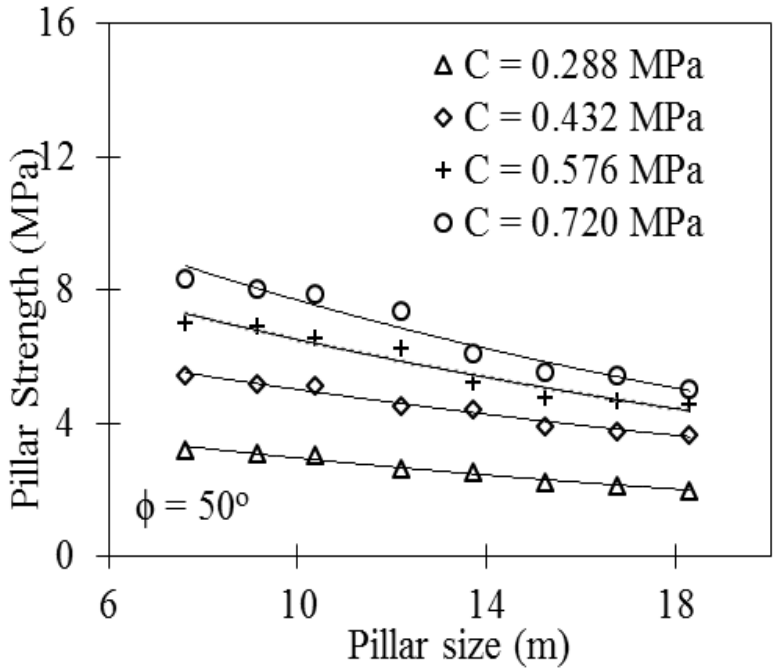

(a)

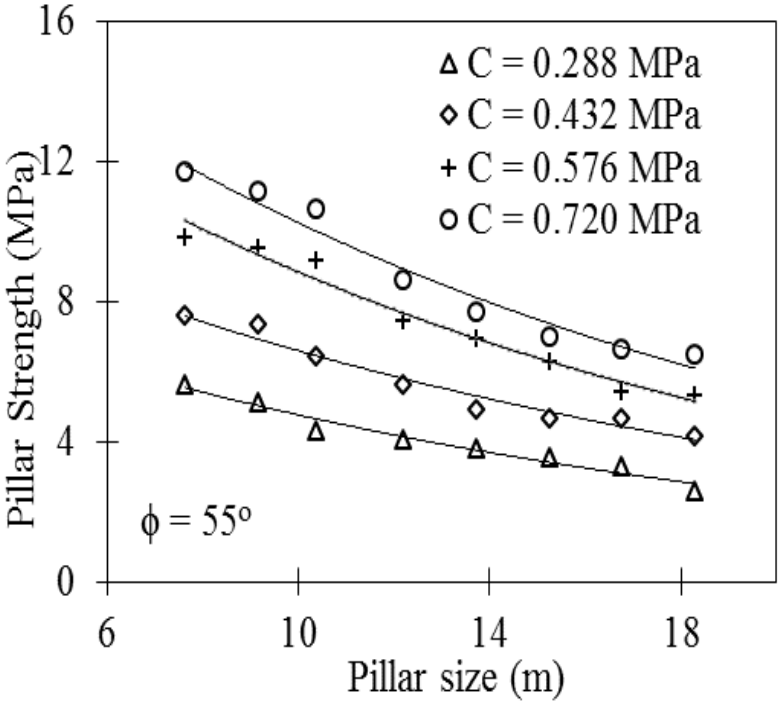

(b)

Figure 4.10. Effect of pillar size and different cohesion on pillar strength at friction angle of: (a) 50°, (b) 55°, (c) 60° and (d) 65°

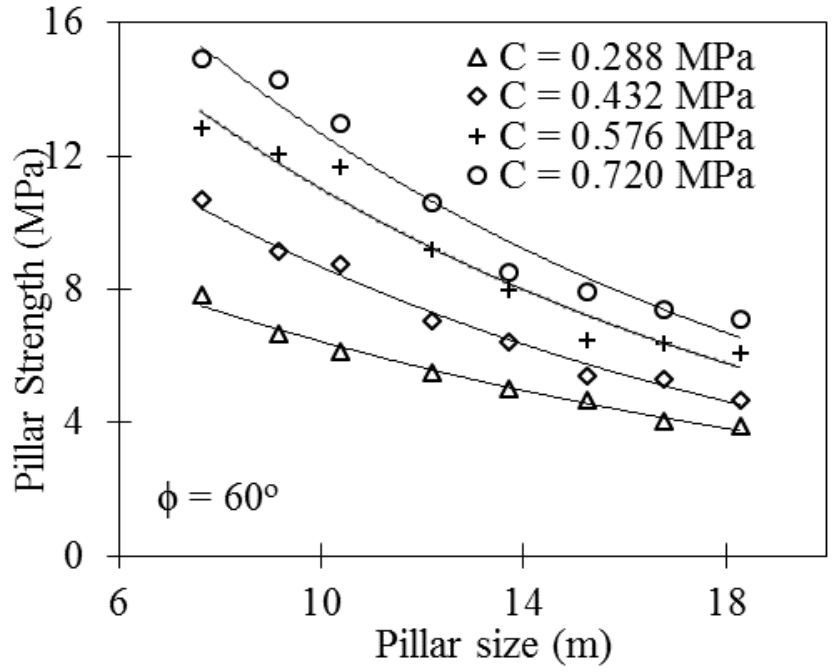

(c)

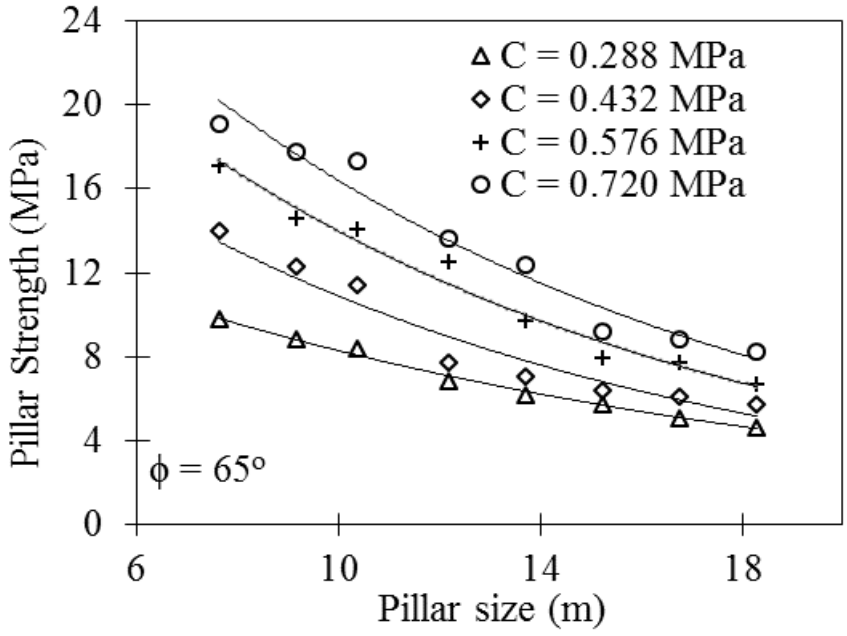

(d)

Figure 4.10. Effect of pillar size and different cohesion on pillar strength at friction angle of: (a) 50°, (b) 55°, (c) 60° and (d) 65° (cont'd)

Where, A, B, and β_O, are empirical constants. β_1 and β_2 are the coefficients of cohesion and pillar height respectively. A positive sign in Equation (64) shows increasing while a negative one connotes decreasing pillar strength with an increase in that parameter. For example as cohesion increases, the pillar strength also increases, hence β_1 is positive. On the other hand, as pillar height increases, pillar strength decreases, hence β_2 is negative. Thus Equation (64) accounts for both size and shape effect.

The researcher used the optimization solver in Microsoft Excel to minimize the sum of the least squared error (the difference between the modeled strength and Equation (64). Since this least squares optimization problem results in a nonlinear optimization problem, the optimal values are obtained with an iterative solution algorithm that starts with initial (guess) values of A, B, β_O, β_1, and β_2. Microsoft Excel Solver adjusted these decision variables until the total least squared error was minimal. The researcher used this procedure to develop empirical pillar design equation for St. Peter Sandstone for different strength properties (Equations 65 to 68).

Equation (67), for example, represents the empirical pillar strength equation for a friction angle of 60°, cohesion ranging from 0.29 to 0.72 MPa, and at a plastic strain of 0.15. Figure 4.11 shows a plot of the modeled pillar strength and pillar strength predicted with Equation (67). The reader can see that there is a strong correlation between the modeled pillar strength and Equation (67). Using similar cohesion and plastic strain values, the researcher developed Equations (65), (66) and (68) to represent pillar strength equations for friction angles of 50°, 55°, and 65°, respectively.

$$S_P = 5.759 + 16.17C - 0.426h\left[0.11 + 0.46(w/h)\right] \quad (65)$$

$$S_P = 6.767 + 9.783C - 0.440h\left[0.27 + 0.74(w/h)\right] \quad (66)$$

$$S_P = 14.360 + 11.720C - 0.903h\left[0.28 + 0.53(w/h)\right] \quad (67)$$

$$S_P = 10.017 + 9.862C - 0.657h\left[0.74 + 0.69(w/h)\right] \quad (68)$$

4.11. EFFECT OF EXTRACTION RATIO ON SAFETY FACTOR

Safety factor is expressed as pillar strength divided by pillar stress. Knowing the pillar stress and strength, the researcher estimated the pillar safety factors. Most pillar designers use safety factor as an index to assess pillar stability. Theoretically, a pillar with a safety factor less than one is unstable since the stress exceeds the strength. A pillar with safety factor greater than 1 is considered stable. However, various researchers (Bieniawski, 1968, Obert and Duval, 1967; Hedley and Grant, 1972; Lunder and Pakalnis, 1997, etc) have used a safety factor of 1.5 to 2 to compensate for variability and uncertainties related to pillar strength and stress estimates, for coal and hard rock mine designs. Designing pillars between safety factors from 1.5 to 2 is a way to resolve uncertainties and implement design conservatism.

The strength of St. Peter Sandstone is anisotropic (Bagherieh, 2015). In an idealized case, predicting the pillar strength of St. Peter Sandstone must take into consideration the variability of the strength properties of St. Peter Sandstone. However, in this study, the researcher assumed that the strength properties of St. Peter Sandstone is isotropic. In addition, the initial in-situ vertical and horizontal stresses were based on Haimson (1978) study. These assumptions introduce uncertainties in the pillar strength predictions. For this reason, the researcher recommends a safety factor of 2 for worst-case pillar design of St. Peter Sandstone.

This worst-case pillar analysis is feasible, and acceptable within economic and safety constraints. For example, using a friction angle of 60^{o} and cohesion of 0.72 MPa, the safety factor of the pillar shown in Figure 4.12, is 1.75. Although this safety factor represents the minimum safety factor for the representative pillar cases shown in Appendix D, it is obvious that the pillar shown in Figure 4.12 is very stable and shows no sign of instability. The approximate pillar width of the pillar shown in Figure 4.12 is 13.41 meters and this pillar has been standing for approximately 54 years. In addition, this pillar has pillar height of 12.19 m and extraction ratio of 73.82%.

The researcher analyzed the effect of extraction ratio on pillar safety factor for different pillar widths, pillar heights, and overburden depths. For example, Figure 4.12 shows the influence of extraction ratio on safety factor for a pillar size (width, w) of 13.41 m (i.e., a square pillar of 13.41 m × 13.41 m), pillar height (h) of 12.19 m and

various overburden depth (*H*). From Figure 4.13, a St. Peter Sandstone mine that expects a safety factor of 2 can adopt these pillar dimensions provided the overburden depth is 61 m and the extraction ratio is 70%. The researcher has presented similar analysis for various pillar sizes, pillar height and overburden depth at Appendix H. For example, the Pattison Sand mine uses a square pillar of width 16.46 m, pillar height of 9.14 m, and extraction ratio of 62%. Yet the mine operates under an overburden depth of less than 76 m. Provided all input parameters used in this study are reasonable estimates, then it is possible for this mine to increase its extraction ratio by up to 9% provided the roof span will be stable (with or without additional rock supports) (Figure 4.14).

Based on this study, it is also possible for a St. Peter Sandstone mine to adopt room and pillar dimensions that provide maximum extraction ratio and safe working conditions.

For initial design, it is practical for the design engineer to limit the roof span to less than 12.19 m. If the roof condition and actual roof performance prove satisfactory, then the room span can be increased within a safety factor of 2 (Esterhuizen et al., 2011).

4.12. SUMMARY

In this study, the researcher was interested in the stresses at the pillar nodes. The governing equation for the stresses at the nodes can be expressed as differential equations. The researcher used the finite difference method, as implemented in the Fast Lagrangian Analysis of Continua in three-dimension (FLAC3D) software, to solve these differential equations. FLAC3D uses an explicit finite difference discretization scheme to solve the associated differential equations.

The work used numerical modeling to estimate average pillar stress of St. Peter Sandstone. The researcher compared the average pillar stresses using FLAC3D to an analytical solution of a simplified problem to verify the solution. In the analysis, the researcher evaluated the influence of mesh size and time step on the FLAC3D numerical solution. The researcher found that as the mesh size and time step increased, the truncation error also increased, until after a mesh size of 1.22 m, the truncation error remained fairly constant. The minimum and maximum truncation errors were -1.63% and 0.92%, respectively.

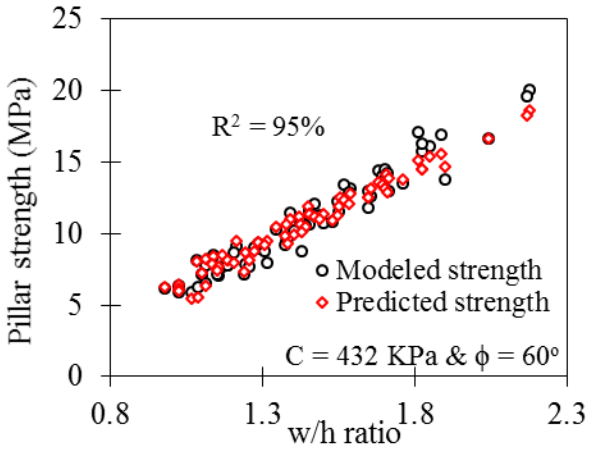

(a)

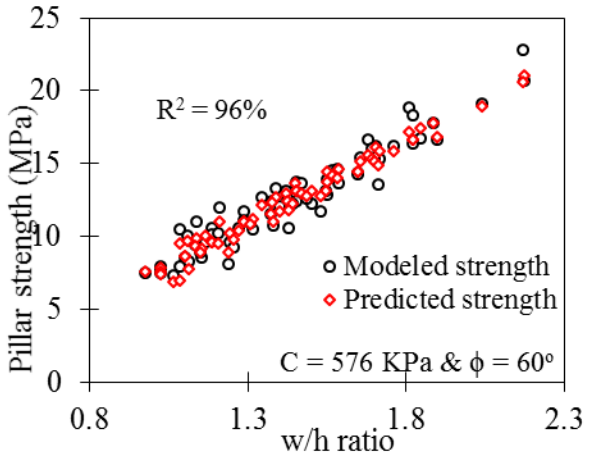

(b)

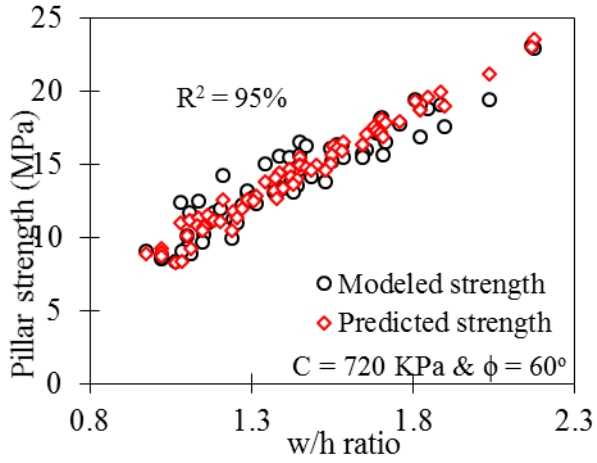

(c)

Figure 4.11. Influence of w/h ratio on pillar strength for cohesion of: (a) 0.432 MPa, (b) 0.576 MPa and (c) 0.72 MPa

Figure 4.12. A pillar with the highest stress at CGB Mine

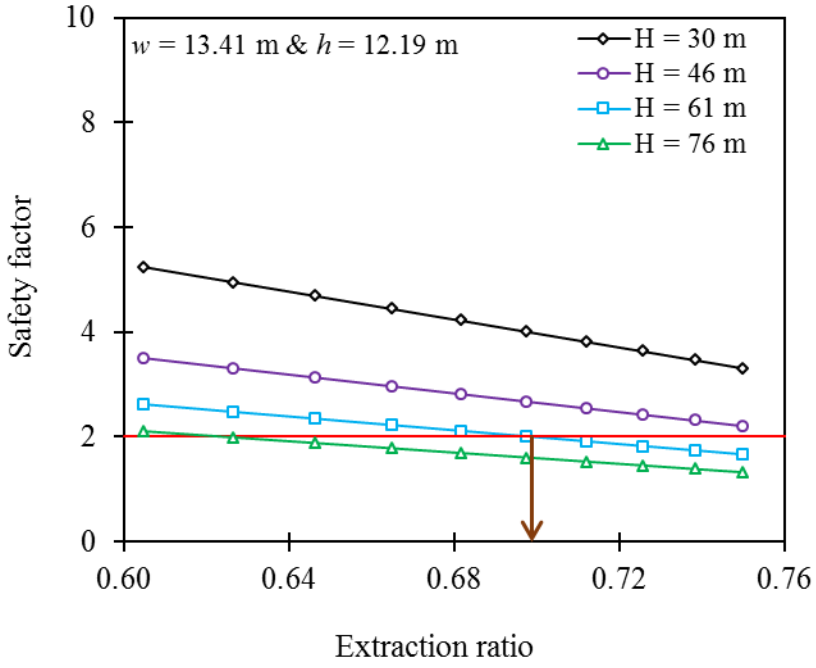

Figure 4.13. Influence of overburden depth (*H*) on safety factor and extraction ratio for pillar size of 13.41 m^2 and pillar height of 12.19 m

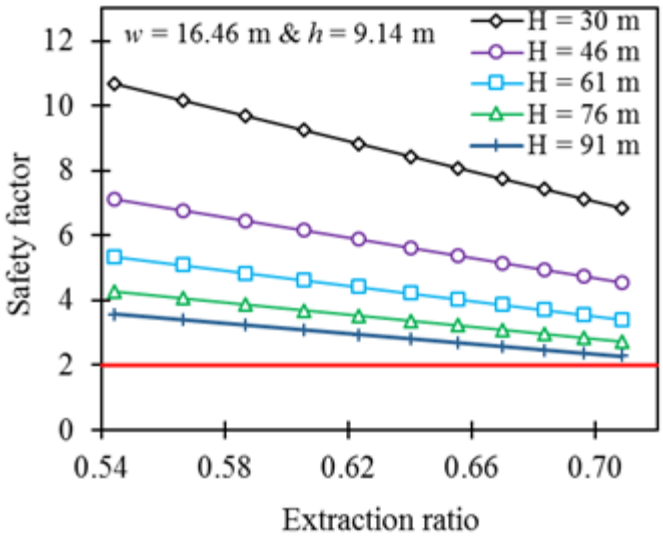

Figure 4.14. Influence of overburden depth (*H*) on safety factor and extraction ratio for pillar size of 16.46.41 m^2 and pillar height of 9.14 m

These truncation errors are within acceptable limits. In this numerical analysis, the researcher recorded a round-off of 0.0000001% of the predicted average pillar stress. The study concluded that these FLAC3D numerical solutions are consistent, stable, accurate and converge to the analytical solution within an acceptable margin of error. Based on this sensitivity analysis and the choice of the discretization limits, the researcher concluded that there is high confidence in FLAC3D numerical results.

The researcher calibrated the numerical model with actual stress change measurements. The finite difference modeling results indicated that there was a satisfactory agreement between the modeled stress change and actual stress change measured. The predicted stress change was higher than the measured stress change by 8.7%.

The work used the calibrated numerical modeling to estimate pillar strength in St. Peter Sandstone mines. Subsequently, this researcher used these results to propose a pillar design criteria for St. Peter Sandstone room and pillar mines. The researcher used the calibrated and validated model to estimate pillar strength for St. Peter Sandstone based on the average pillar stress. The researcher compared pillar strength estimates using the Mohr-Coulomb and strain softening Mohr-Coulomb constitutive laws. The results indicated that the Mohr-Coulomb models predicted pillar strength that was 1.5 to 7 times

that of the strain softening Mohr-Coulomb model. For conservative pillar design, the researcher resorted to using the strain softening Mohr-Coulomb constitutive laws to predict pillar strength for St. Peter Sandstone. The researcher has proposed Equation (67) for the design of St. Peter Sandstone pillars.

The researcher recommends a safety factor of 2 for designing St. Peter Sandstone pillars. Based on this study, it is also possible for any St. Peter Sandstone mine such as Pattison Sand mine to adopt room and pillar dimensions that provide maximum extraction ratio and safe working conditions.

5. CAUSES OF PINCH OUT FAILURE

This Section explores possible causes of pinch out failure in room and pillar mines as observed at the Pattison Sand mine. Possible hypothesis to explain pinch out failures in St. Peter Sandstone mines include but are not limited to beam theory, geometry of mine openings, roof rock properties, and particle size analysis. In this study, this researcher evaluated three hypotheses that could explain the occurrence of pinch out failure. These hypotheses are: (1) roof rock properties; (2) geometry of the mine opening is a contributory factor to pinch out failures; and (3) pinch out failure is due to lower uniaxial compressive strength associated with coarse-grained St. Peter Sandstone samples

5.1. ROOF ROCK PROPERTIES HYPOTHESIS

During field visits, this researcher observed that pinch out failure occurs at the pillar top in some locations, and not in others. The pillar geometry was either in square or rectangular cross-section. Also, this researcher observed that the roof rock was either cemented or uncemented St. Peter Sandstone. The strength of cemented St. Peter Sandstone is about 5 to 8 times that of uncemented St. Peter Sandstone depending on the degree of cementation (Bagherieh, 2015). Similarly, the elastic modulus for cemented St. Peter Sandstone is about 25 times that of the uncemented St. Peter Sandstone. It is unknown whether contrast in roof rock properties influences the occurrence of pinch out failure. It is hypothesized that the roof rock properties is a contributory factor to pinch out failures. This is motivated by the fact that roof failure is influenced by roof rock properties (Molinda and Mark, 2010; Iannachione et al., 2005, Bajpayee et al., 2014). For that reason, this work sought to use numerical modeling techniques to explore whether contrast in roof rock properties influenced pinch out failures at some locations.

To carry out this objective, this researcher developed two separate squared shape pillar models with a w/h ratio of one and an extraction ratio of 68%. In the modeling process, this researcher assigned the strain softening Mohr-Coulomb constitutive law to the pillar rock. However, this researcher used the elastic properties to simulate the roof rock independently, for the cemented and uncemented St. Peter Sandstone. Two separate models result from this analysis: EMUS, which represents the model in which this

researcher used the elastic model to simulate uncemented St. Peter Sandstone roof rock; and EMCS, which represents the model in which this researcher used the elastic model to simulate cemented St. Peter Sandstone roof rock. In both models, the researcher allowed 0.91 meters of uncemented St. Peter Sandstone beneath the pillar.

This researcher compared the horizontal cross-sections of the zones of failure at the pillar top, mid-height, and bottom, as averaged pillar stress increased for EMCS and EMUS models. Figures 5.1 to 5.4 show the zones of failure at the pillar top, mid-height and bottom as the average pillar stress increased. The terms associated with the colors in the legends of Figures 5.1 to 5.4 represent a state of failure. For example, the “none” indicates no failure; “shear-n” indicates shear failure now; “shear-p” indicates shear failure in the past; “tension-n” indicates tensile failure now; “tension-p” indicates tensile failure in the past; “shear-n tension-p” indicates that the zone is in shear failure now but yielded in tension in the past, and so on. For easy comparative analysis, the reader should focus on the blue color, which represents no failure. Figure 5.5 summarizes the percentage of failed zones at the pillar top, mid-height and bottom.

Clearly, the percentages of the failed zones at the pillar top did not change as average pillar stress increased, and remained at about 94% and 27%, respectively, for the EMCS and EMUS models (Figure 5.5a). In other words, at the pillar top, failure is 3.5 times more likely to occur for the cemented St. Peter Sandstone than that of uncemented St. Peter Sandstone. Hence, pinch out failure is bound to be more pronounced when the roof rock is cemented St. Peter Sandstone. It is interesting to note that the percentage of the zones of failure at the pillar bottom is almost the same for both EMCS and EMUS models. This is due to the fact that in both models, this researcher used 0.91 meters of uncemented St. Peter Sandstone as the immediate floor.

While these findings are consistent with field observations at Pattison Sand mine, it is interesting to investigate the reasons why pinch out failure is more pronounced when the roof rock is cemented St. Peter Sandstone. It is possible that pinch out failures is influenced by high stress concentration at the pillar top (Molinda and Mark, 2010; Iannachione et al., 2005, Bajpayee et al., 2014). As a result, this researcher used numerical models to further explore whether relatively high stress concentration at the

pillar top influenced the affinity of pinch out failure when the roof rock was cemented St. Peter Sandstone.

Appendix I shows the differential stress concentrations at the pillar top, midheight and bottom for the squared pillar for EMCS and EMUS models. Figures 5.6 and 5.7 show the influence of differential stresses on average pillar stress at the pillar top, midheight and bottom for EMCS and EMUS models.

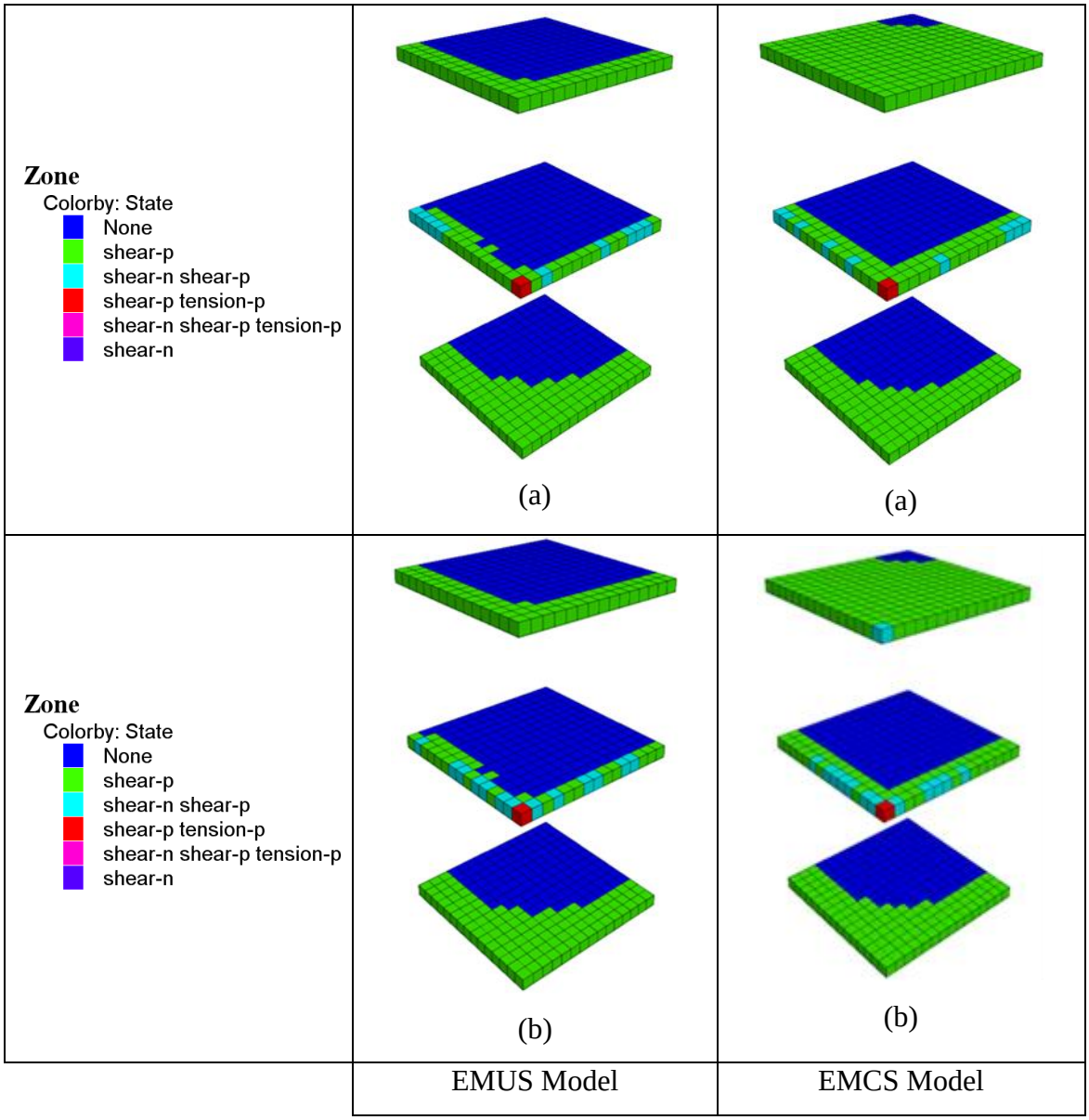

Figure 5.1. Extent of failure at pillar top, middle and bottom for a squared pillar using EMCS and EMUS models for average pillar stresses of: (a) 3 MPa and (b) 4 MPa

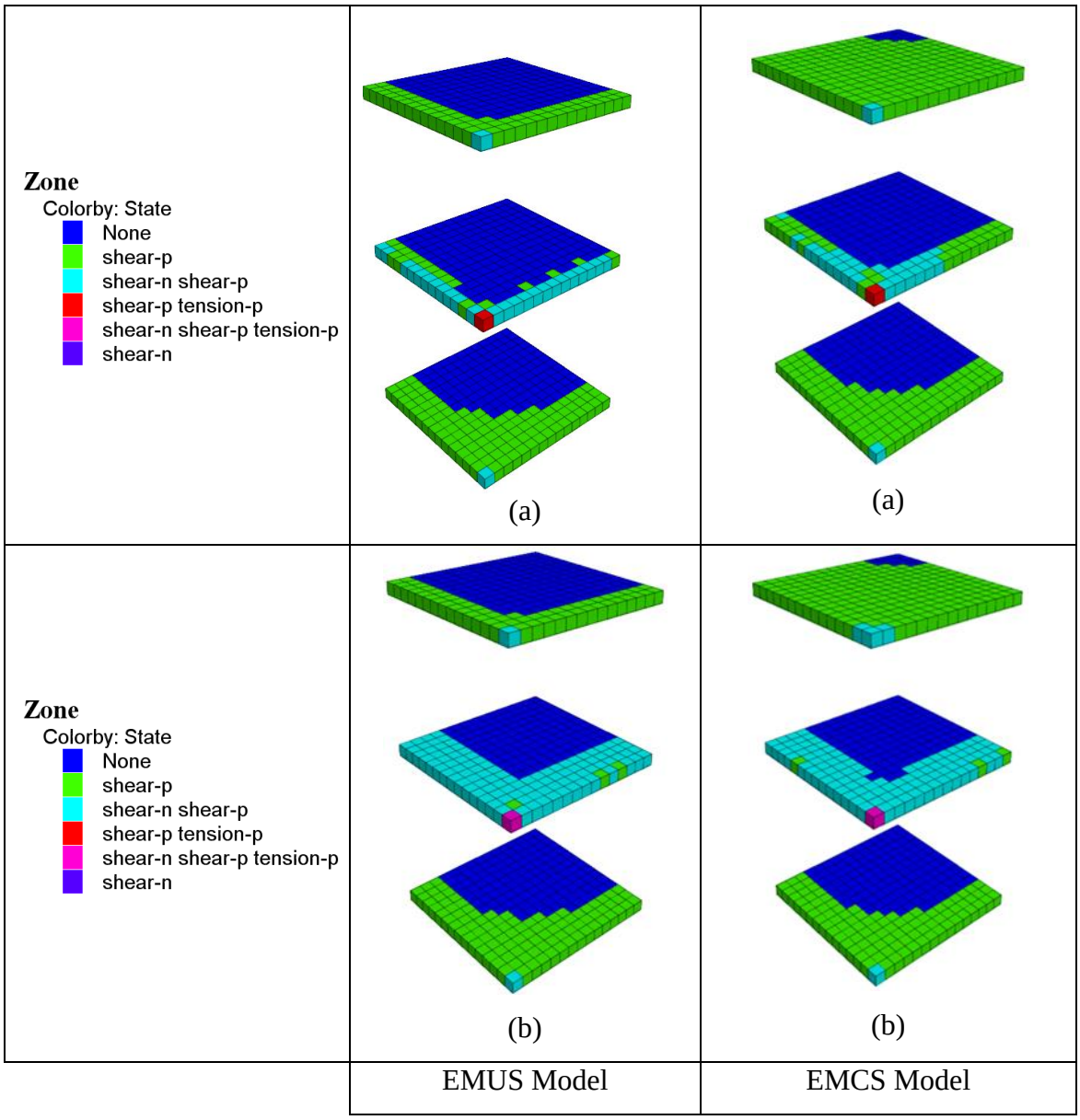

Figure 5.2. Extent of failure at pillar top, middle and bottom for a squared pillar using EMCS and EMUS models for average pillar stresses of: (a) 5 MPa and (b) 6 MPa

It is seen that the differential stress concentrations at the pillar bottom are relatively high compared to the pillar top, for EMCS and EMUS models. The relatively high differential stress concentration at the pillar bottom is for the reason that additional in-situ stresses are imposed at the pillar bottom from the pillar top column. For this reason, one can argue that pinch out failure will more likely occur at the pillar bottom

rather than the pillar top. However, this maybe valid in some instances and not in others. On the one hand, the relatively high differential stress concentrations at the pillar bottom showed that more zones failed at the pillar bottom when the floor and roof rock is uncemented St. Peter Sandstone (see EMUS model in Figures 5.1 to 5.4).

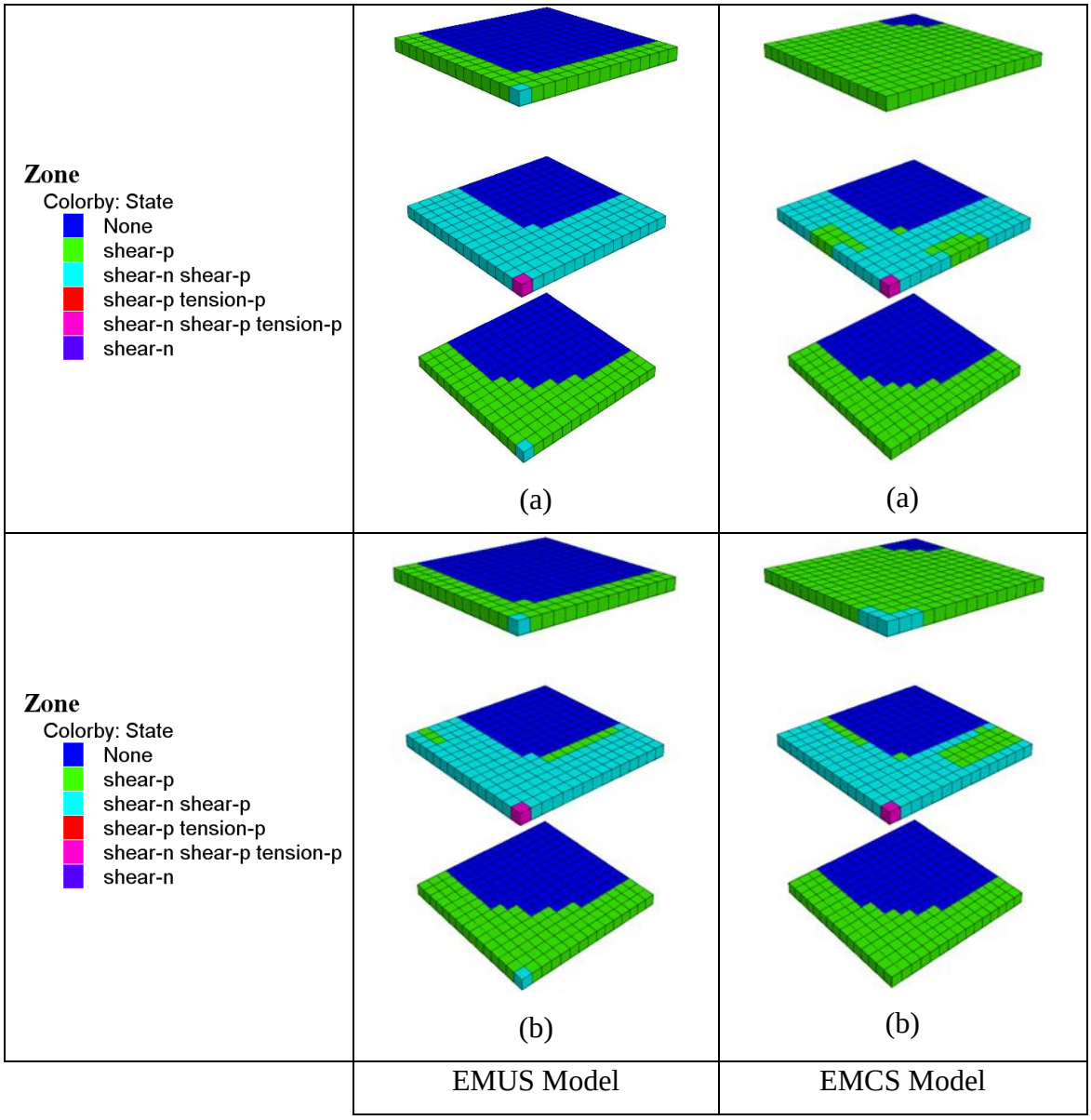

Figure 5.3. Extent of failure at pillar top, middle and bottom for a squared pillar using EMCS and EMUS models for average pillar stresses of: (a) 7 MPa and (b) 8 MPa

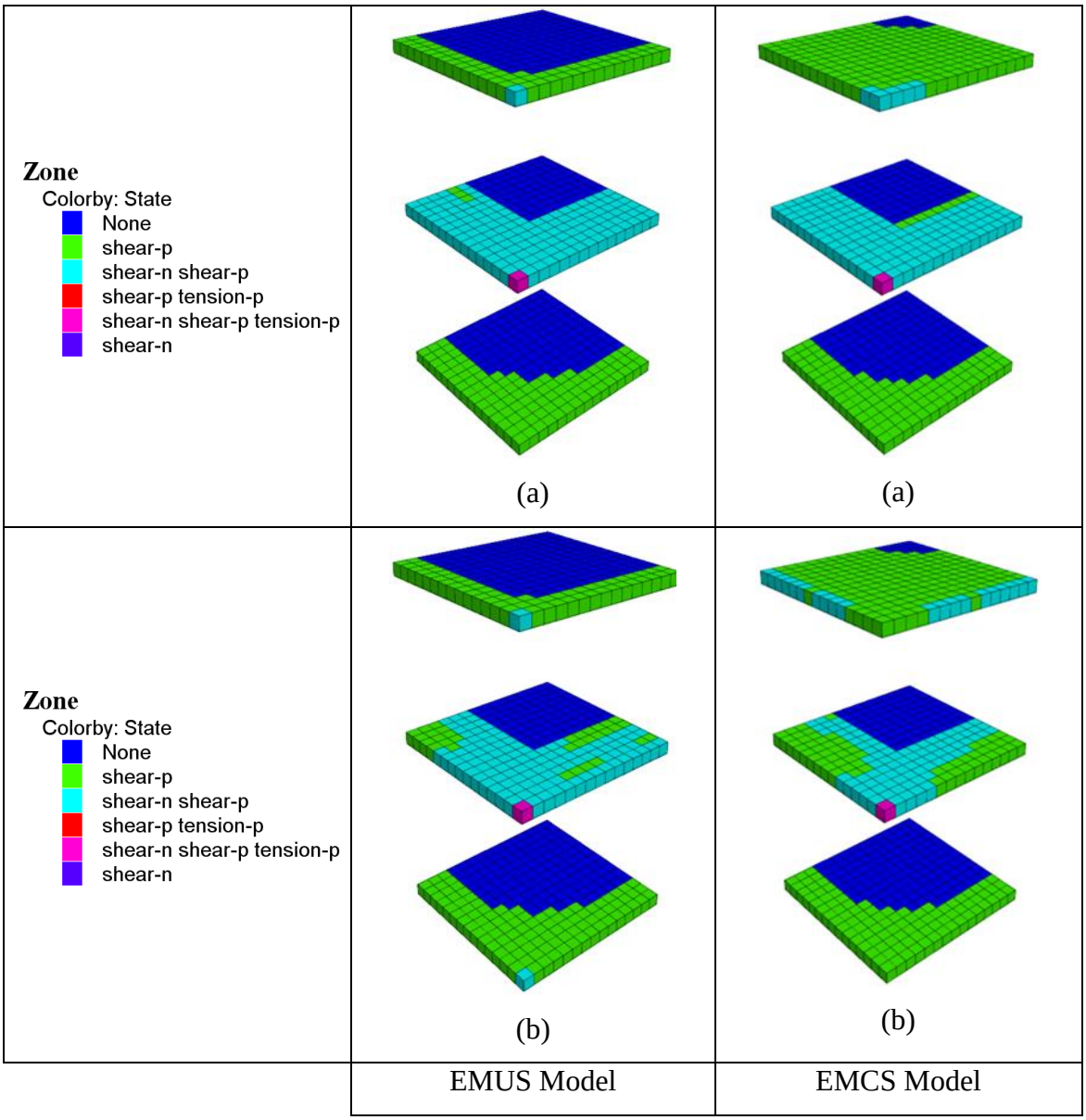

Figure 5.4. Extent of failure at pillar top, middle and bottom for a squared pillar using EMCS and EMUS models for average pillar stresses of: (a) 9 MPa and (b) 10 MPa

On the other hand, the relatively high differential stress concentrations at the pillar bottom showed that more zones failed at the pillar top when the floor was uncemented St. Peter Sandstone and roof rock was cemented St. Peter Sandstone (see EMCS model in Figures 5.1 to 5.4). In both cases, it is evident that, pinch out failure is not due to the relatively high stress concentration at the pillar top when the roof rock was

cemented St. Peter Sandstone, rather, it is the contrast in the pillar-roof rock properties. This further confirms that pinch out failures occur due to the contrast in the rock properties at the pillar-roof interface.

This result (Figure 5.5a) demonstrates that pinch out failure is not as a result of higher overburden stress as MSHA hypothesized and used as a basis to shut down Pattison Sand mine in 2010.

Giles (1930) found that the thickness of St Peter Sandstone is not uniformly distributed as its thickness differed from place to place. In this study, the research team drilled 39 boreholes at different locations at Pattison Sand mine to estimate the thicknesses of uncemented St. Peter Sandstone, for reserve estimation, mine planning, and ground control purposes. Figure 5.8 shows that the thickness of the uncemented St. Peter Sandstone differ from place to place at Pattison Sand mine. This confirms Giles' (1930) assertion. Additionally, the measured pillar heights also varied from place to place. Consequently, one will expect that since the thicknesses of the excavations vary from place to place, it is possible that the intersection of the uncemented and cemented St. Peter Sandstone will not be at the same elevations for all pillars. For this reason, if pinch out failure is controlled by where the cemented St. Peter Sandstone layer occurs in a pillar as hypothesized here, then it will not occur at every location. This is evidence in support of this hypothesis.

5.2. GEOMETRY OF MINE OPENING HYPOTHESIS

Pattison Sand mining excavations leave pillars into square or rectangular cross-sections. Field studies conducted by this researcher also revealed that the roof of the mine openings at Pattison Sand mine was mostly flat, although this researcher saw a few arched shaped roofs. Flat roof openings are usually associated with square or rectangular pillars. Arched shape pillars have arched roof mine openings. Caudle and Clark (1955) showed that excavations of square or rectangular pillars allow high stress concentrations along the sharp corners. High stress concentrations along the sharp corners of square or rectangular pillars are more likely to cause rock fracturing or premature failures (Hustrulid, 2001).

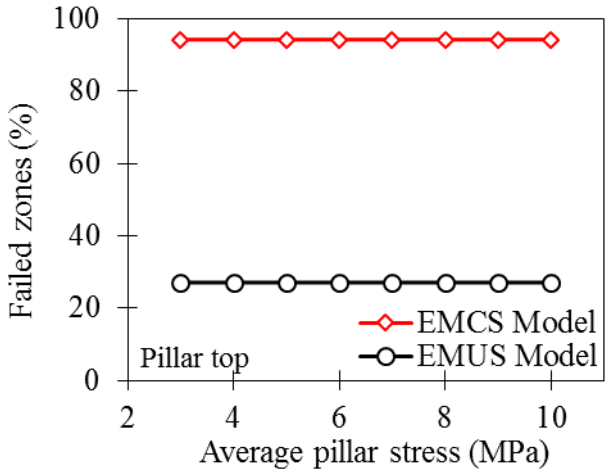

(a)

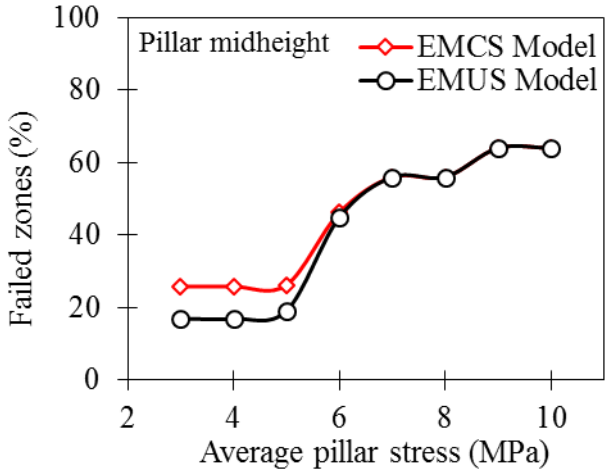

(b)

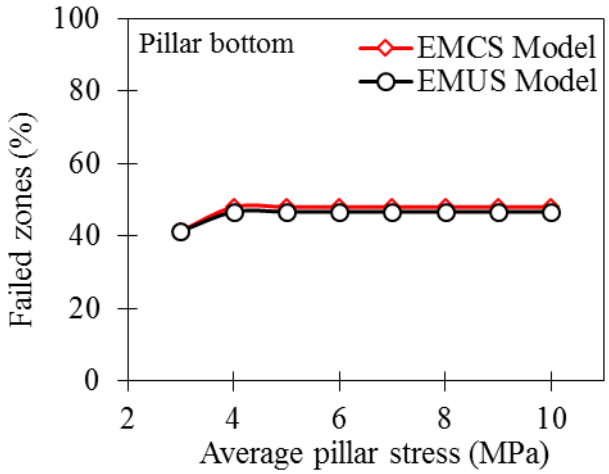

(c)

Figure 5.5. Percent of failed zones on average pillar stress for EMCS and EMUS model at the: (a) pillar top; (b) pillar midnight ;(c) pillar bottom

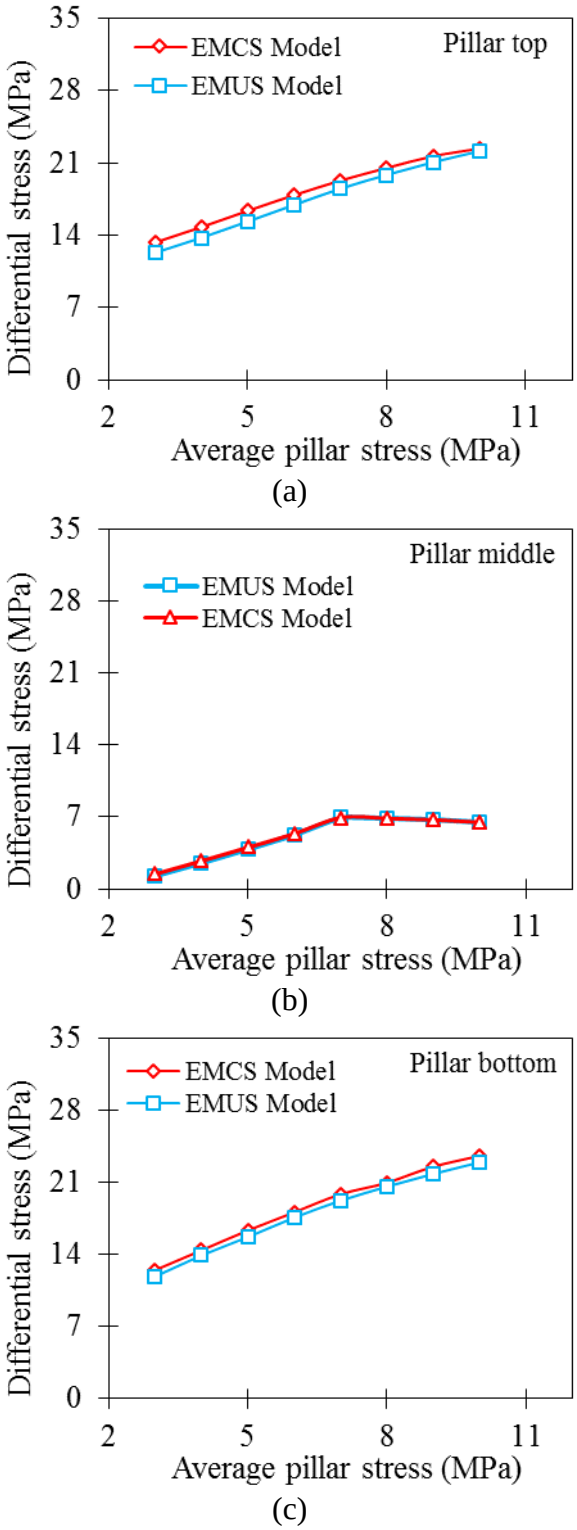

Figure 5.6. Differential stress concentration against average pillar stress for EMUS, and EMCS models at: (a) pillar top; (b) pillar middle; (c) pillar bottom

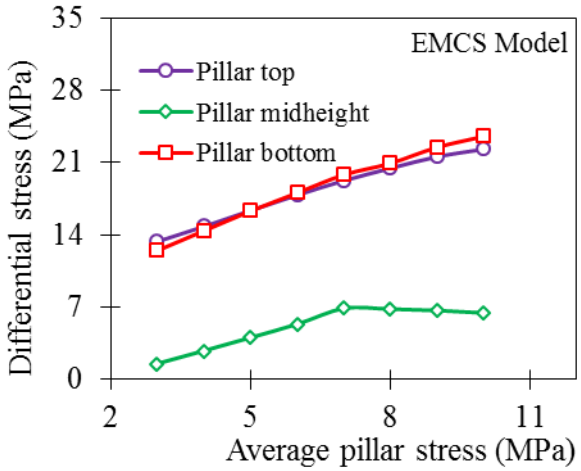

(a)

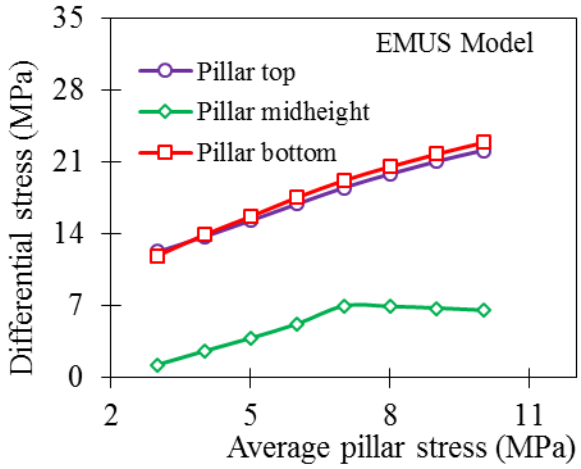

(b)

Figure 5.7. Effect of percent of failed zones on average pillar stress for EMCS and EMUS model at the: (a) EMCS model; (b) EMUS model

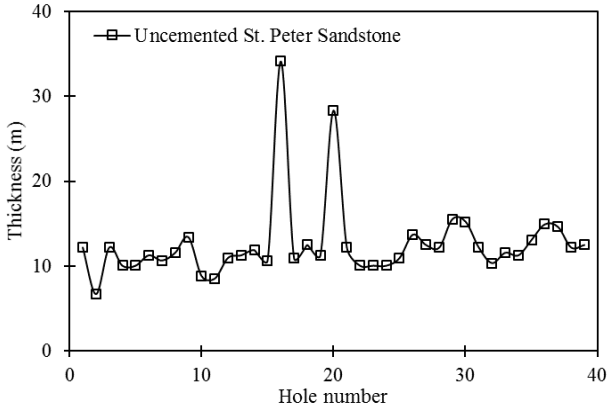

Figure 5.8. Thickness of uncemented St. Peter Sandstone at Pattison Sand Mine

It is unknown whether the shape of mine opening influences the occurrence of pinch out failure. The researcher evaluated the hypothesis by simulating the pillar, roof, and floor to determine whether pinch out failure can be influenced by the shape of the mine opening.

This researcher used numerical modeling to simulate pillar, roof and floor interaction in formation excavations. Particularly, this researcher developed a square and arched shape pillars, having a width to height ratio of unity and extraction ratio of 68%. The researcher calibrated these models in a way that the average pillar stresses were with allowable error limit. For example, the average pillar stress for the square-shaped was 2.34 MPa, which was 1.73% less than the average pillar stress estimated using the tributary area method. Also, the average pillar stress for the arched shaped was 2.35 MPa, which was 1.20% less than the average pillar stress predicted using the tributary area method. Thus, the average pillar stresses predicted for the square and arched shaped models were within an acceptable degree of error.

This researcher also examines if the choice of the constitutive model influence stress concentration. Consequently, in the modeling process, this researcher assigned the strain softening Mohr-Coulomb constitutive law to the pillar rock. However, this researcher used the elastic and strain softening Mohr-Coulomb properties to simulate the roof rock independently, for the cemented and uncemented St. Peter Sandstone. Three separate models result from this analysis: EMUS, which represents the model in which this researcher used the *elastic model* to simulate *uncemented* St. Peter *Sandstone* roof rock; EMCS, which represents the model in which this researcher used the *elastic model* to simulate *cemented* St. Peter *Sandstone* roof rock, and SSMCUS, which represents the model in which this researcher used the *strain softening Mohr-Coulomb model* to simulate *uncemented* St. Peter Sandstone roof rock. The researcher monitored the differential stress concentration along the pillar top, midheight and bottom (Figure 5.9). Appendix J shows the differential stress concentrations for the arched shape pillar model.

Figure 5.10 compares the influence of differential stress concentration with average pillar stress for squared and arched shaped pillar models at the pillar top, midheight and bottom.

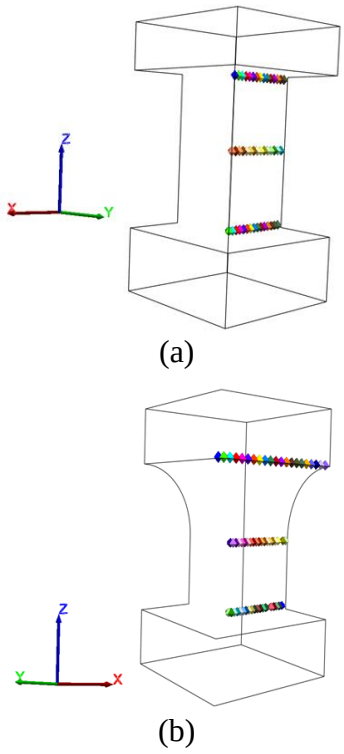

Figure 5.9. Monitoring locations indicated by the diamond shaped colors along the ribs of the: (a) square shaped pillar (b) arched shaped pillar

Figure 5.10a shows relatively high differential stress concentration for the squared pillar compared to the arched shaped pillar, particularly at the pillar top. In addition, as average pillar stress increased the differential stress concentration also increased for the flat roof opening, yet remained fairly uniform for arched roof opening. This indicates that irrespective of the constitutive model used, pinch out failure is more pronounced in the square shaped. Also, this researcher compared the state of pillar failure as average pillar stress increases for the squared and arched shaped pillar models. Figures 5.11 to 5.12 show the influence of the state failure for the squared and arched shaped pillars. Appendix K compares the differential stress concentrations at the pillar top, midheight and bottom, for the arched and squared shape pillar geometries. These results show that pinch out failure was likely in the squared shape pillar than arched shape pillar (Figure 5.11 to 5.12). This agrees with the findings in the literature (Caudle and Clark, 1955; Hustrulid, 2001).

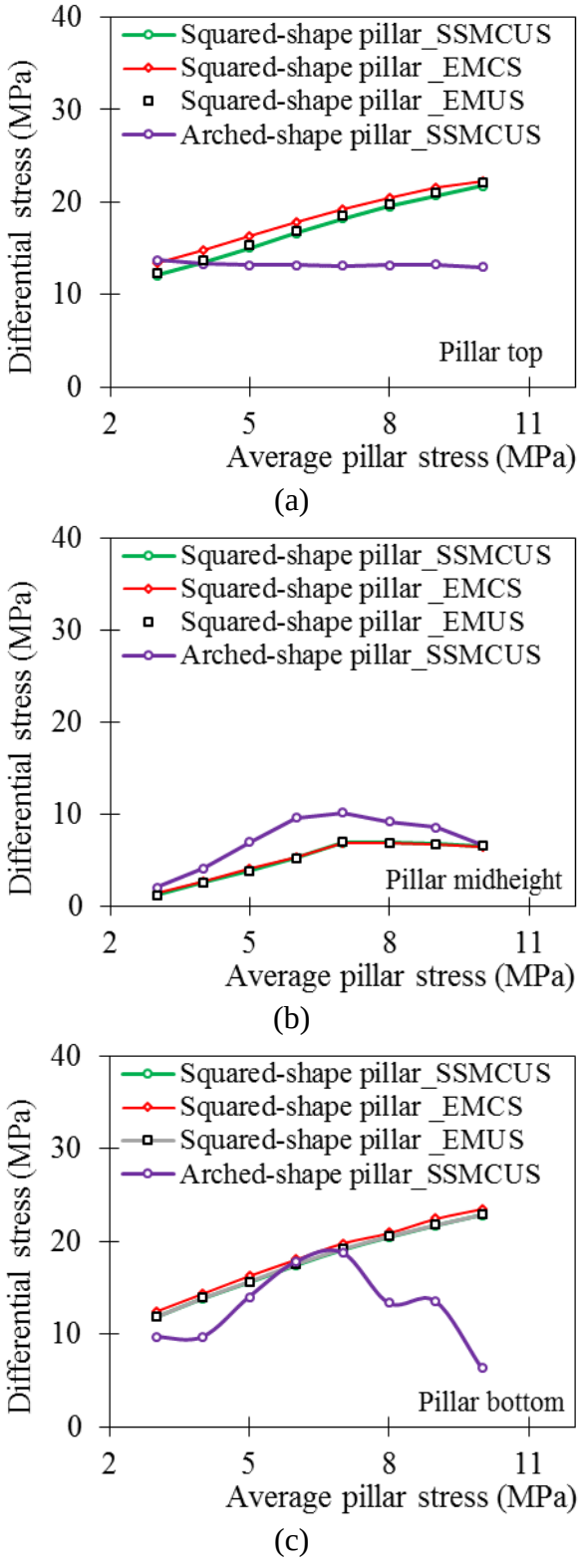

Figure 5.10. Differential stress concentration against average pillar stress for square and arched shape pillar models at: (a) pillar top; (b) pillar middle; (c) pillar bottom

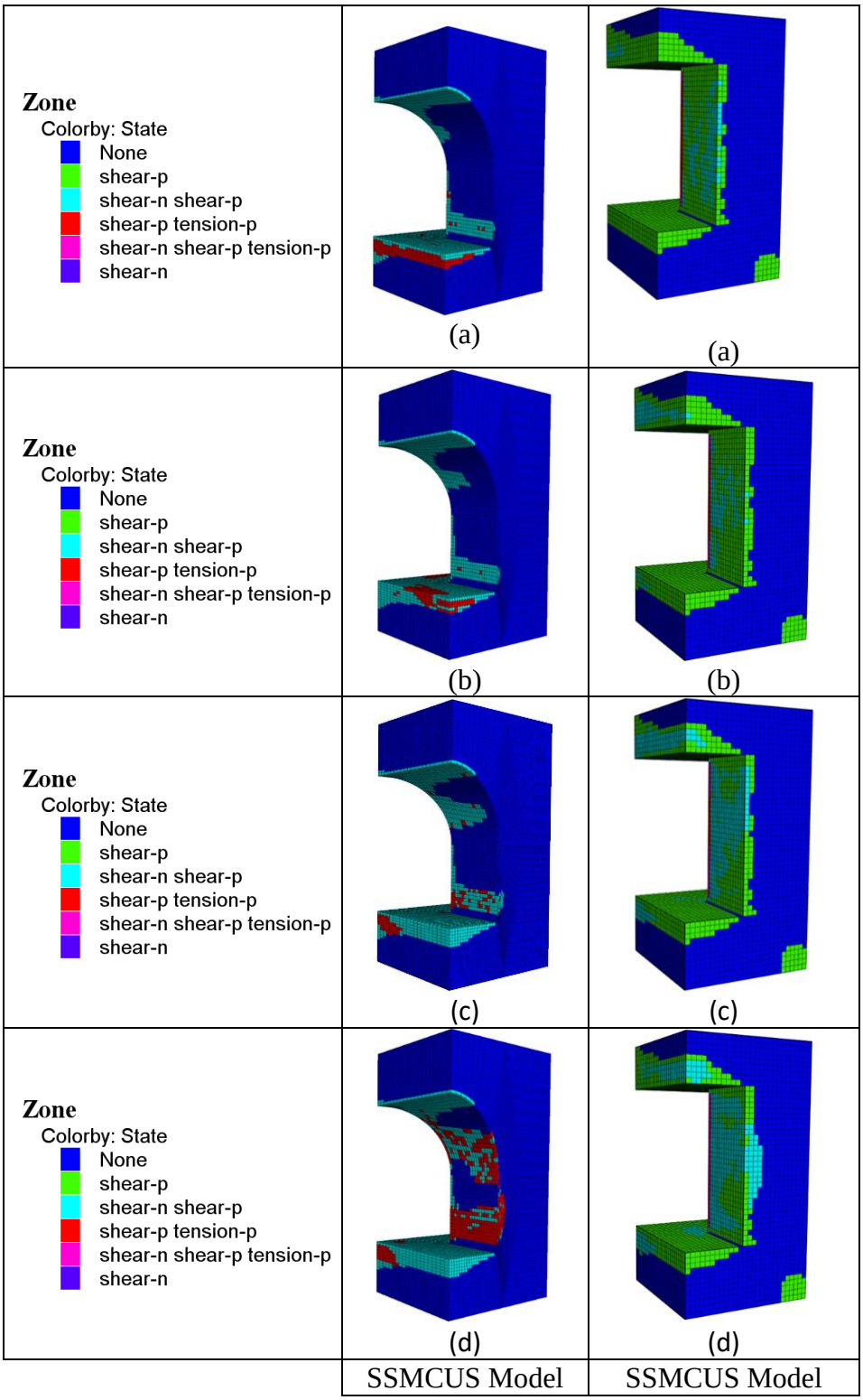

Figure 5.11. Comparison of extent of failure for arched and squared shape pillar using SSMCUS model for average pillar stresses of: (a) 3 MPa; (b) 4 MPa; (c) 5 MPa; (d) 6 MPa (e) 7 MPa; (f) 8 MPa; (g) 9 MPa; and (h) 10 MPa

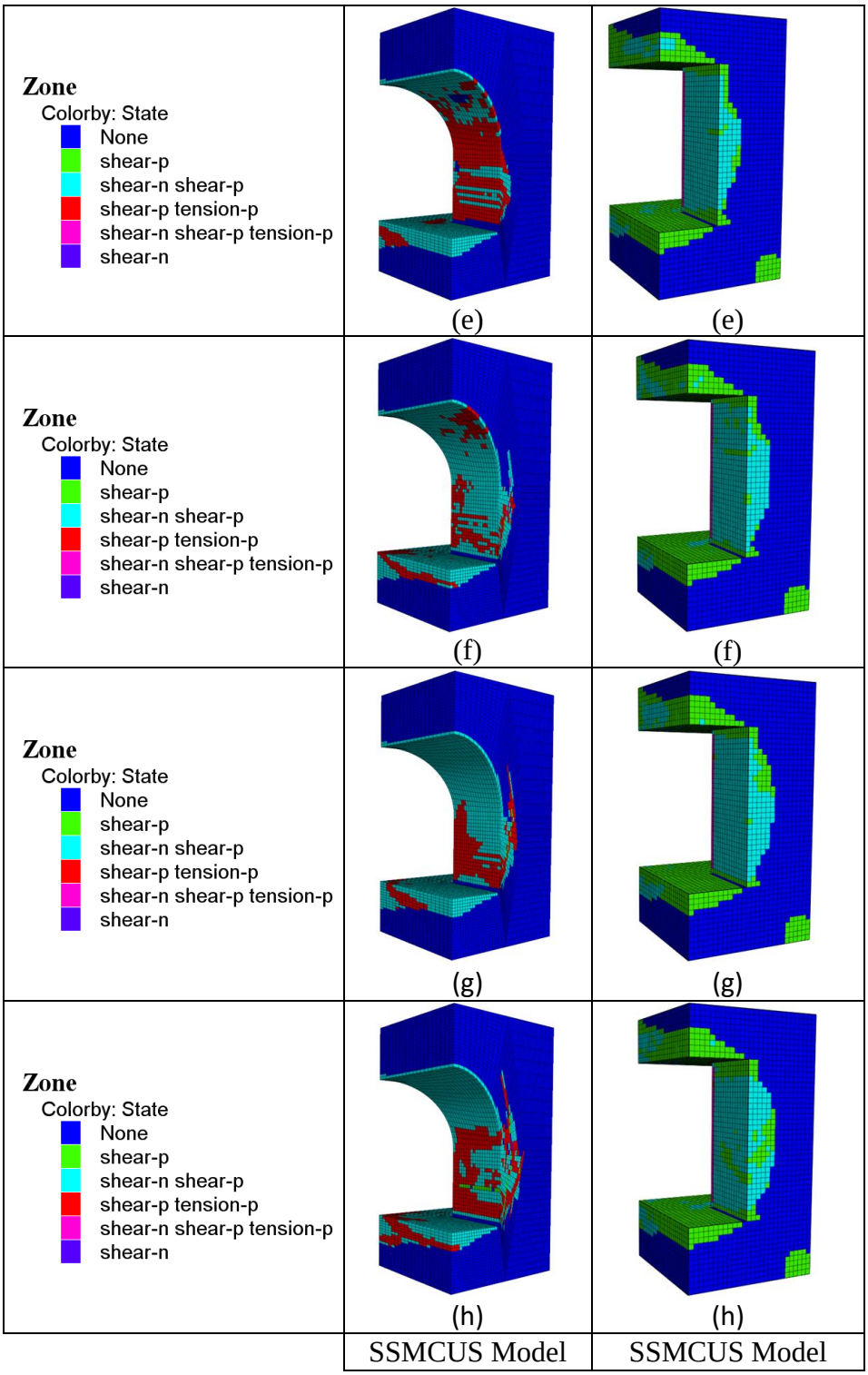

Figure 5.11. Comparison of extent of failure for arched and squared shape pillar using SSMCUS model for average pillar stresses of: (a) 3 MPa; (b) 4 MPa; (c) 5 MPa; (d) 6 MPa (e) 7 MPa; (f) 8 MPa; (g) 9 MPa; and (h) 10 MPa (cont'd)

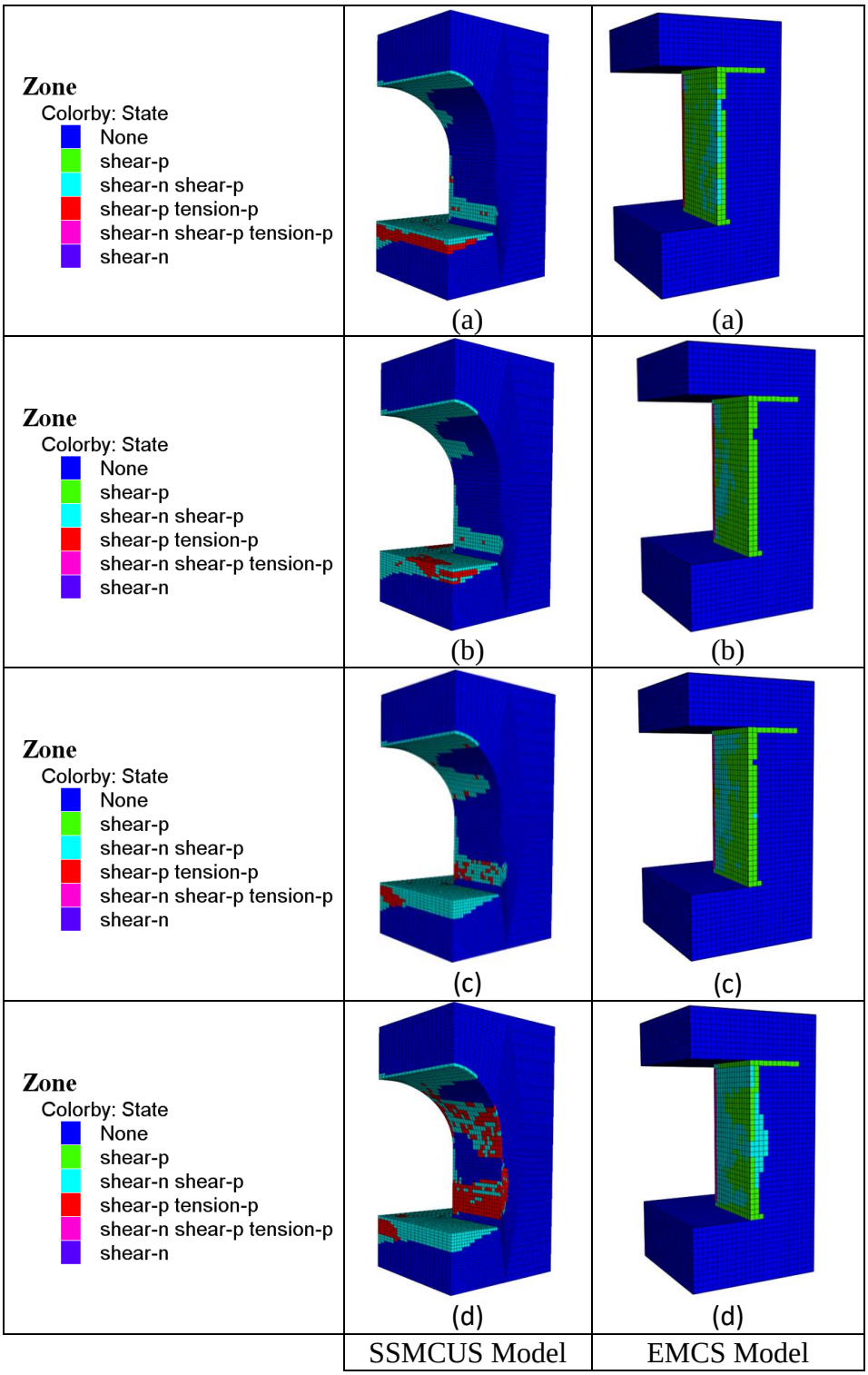

Figure 5.12. Comparison of extent of failure for SSMCUS arched shaped and EMCS squared shape pillar model for average pillar stresses of: (a) 3 MPa; (b) 4 MPa; (c) 5 MPa; (d) 6 MPa; (e) 7 MPa; (f) 8 MPa; (g) 9 MPa; and (h) 10 MPa

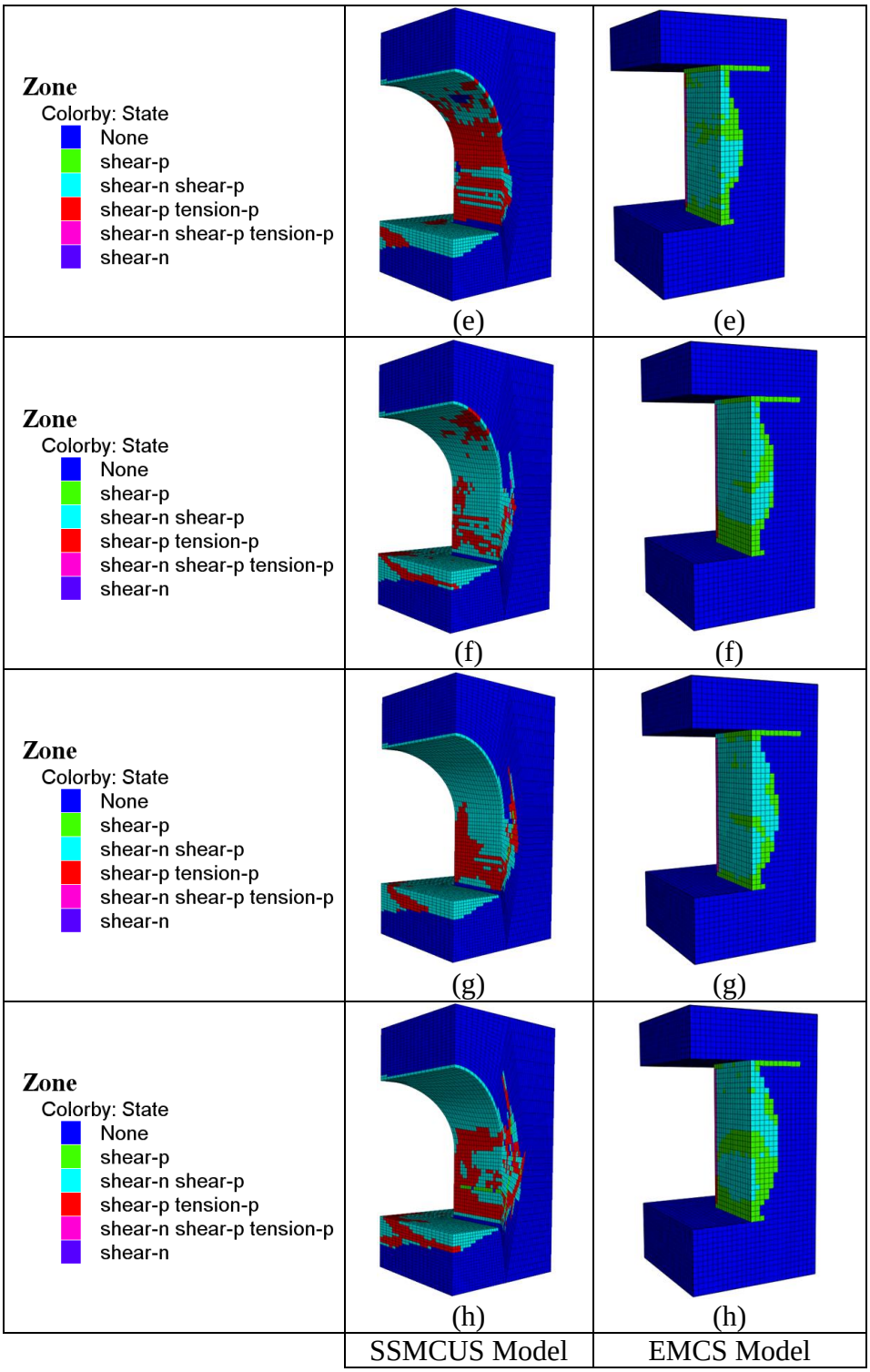

Figure 5.12. Comparison of extent of failure for SSMCUS arched shaped and EMCS squared shape pillar model for average pillar stresses of: (a) 3 MPa; (b) 4 MPa; (c) 5 MPa; (d) 6 MPa; (e) 7 MPa; (f) 8 MPa; (g) 9 MPa; and (h) 10 MPa (cont'd)

5.3. PARTICLE-SIZE ANALYSIS HYPOTHESIS

In this study, this researcher collected over 50 samples from four pillar locations (namely 12H, 2RR, 4NN, and 12C). At these locations, the research team collected samples from the top of the pillar to the pillar bottom at varying distance intervals. At these locations, the research team collected samples from the top of the pillar to the pillar bottom at varying distance intervals.

This researcher conducted extensive particle-size analysis using the laser diffraction technology developed by Microtrac. For each specimen, the researcher repeated the particle size analysis thrice. Microtrac particle-size analyzer can provide accurate, reliable and repeatable particle size distributions within the ranges of 0.02 to 2000 microns (Bagherieh, 2015). The researcher used this equipment to compute the average particle size distribution for each specimen. He then conducted the particle size analysis based on the average particle size distributions.

Several researchers found that grain sizes affect rock strength for: limestone (Lounsbery and West, 1965, and Ballivy, 1984), granite (Brace, 1966; Onodera and Asoka-Kumara, 1980; and Liu et al., 2005), greywacke (Singh, 1988) and mafic rocks (Brattli, 1992). These researchers found that, for the same mineral composition, the finer the grain sizes, the higher the rock strength. Previous studies have established that coarser-grained St. Peter Sandstone samples had relatively lower uniaxial compressive strength than finer-grained samples (Bagherieh, 2015). For this reason, if the particle size at a pinch out failure area is relatively coarse-grained, then it is possible that pinch out failure occurs because of the lower uniaxial compressive strength associated with coarse-grained St. Peter Sandstone samples.

Geotechnical engineers use the uniformity coefficient (the ratio of D_{60} to D_{10}, where D_{60} and D_{10} are the grain diameter in millimeters corresponding to 60% and 10% passing, respectively) to establish whether a soil is relatively coarse or fine grained. In general, the higher the uniformity coefficient the finer the particle sizes and vice versa. Using the average particle size distributions, the researcher computed the uniformity coefficients for each St. Peter Sandstone sample. The study found the uniformity coefficients for 6AR and 1S samples to be 1.7 and 1.6, respectively. Figure 5.13 shows

the uniformity coefficients, from the top to the bottom, of the four pillars (12H, 2RR, 4NN, and 12C).

The fact that this study found no observable pattern in the uniformity coefficients even when the distance from the floor increased, suggests that the particle size distributions for St. Peter Sandstone are heterogeneous (Figure 5.13). This study found the uniformity coefficient at a pinch out failure location (8.5344 m above the floor elevation at pillar 12C) to be 1.44. It is interesting to note that this value is the lowest of all the samples in Figure 5.13 and also low when compared to samples 6AR and 1S. This suggests that the particle sizes at the pinch out failure location are relatively coarse. The researcher concluded that it is possible that pinch out failure occurs at relatively coarse-grained St. Peter Sandstone locations. In addition, the fact that the uniformity coefficients at the pillar top were not necessarily low suggests that pinch out failure is not only bound to occur at the pillar-roof interface. For instance, the pillar top at 12C is about 15.54 m from the floor elevation, yet pinch out failure occurred at the 8.5344 m from the floor elevation.

In general, the higher the uniformity coefficient the higher the strength of the material. The uniaxial compressive strength of 6AR and 1S samples are 4.67 MPa and 3.52 MPa, respectively.

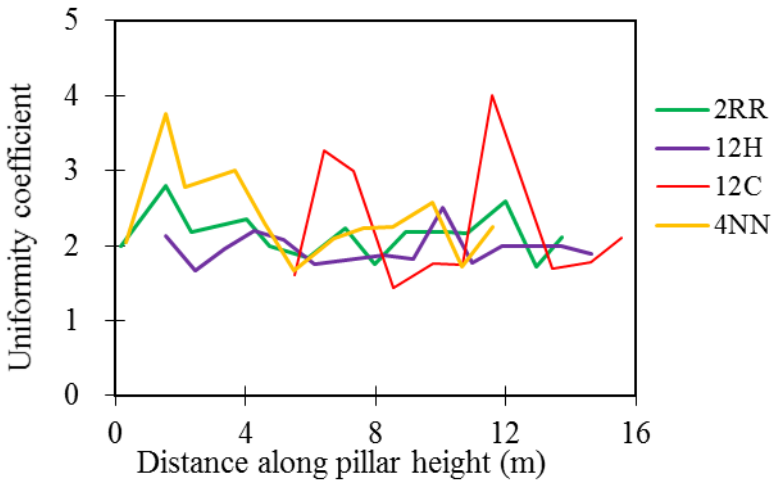

Figure 5.13. Uniformity distribution along the pillar heights

It appears that the higher the uniformity coefficient, the higher the strength and the lower the uniformity coefficient the lower the strength for St. Peter Sandstone. This conclusion confirms the work done by Igwe et al. (2007) on silica sands. From Figure 5.13, it is evident that the uniformity coefficient at the pinch out failure location is the lowest of the samples in this research. This lowest uniformity coefficient suggests relatively lower uniaxial compressive strength. The researcher concludes that pinch out failure may be due to the lower uniaxial compressive strength associated with coarse-grained St. Peter Sandstone samples.

To the best of this researcher's knowledge, there has been no previous attempt to characterize the uniformity coefficient of St. Peter Sandstone samples from the pillar top to bottom. This characterization is vital for effective ground control, mine planning and management of pinch out failure in St. Peter Sandstone room and pillar mines. In addition, another researcher can use this study as a foundation for further research.

5.4. SUMMARY

This Section explores possible causes of pinch out failure in room and pillar mines as observed at the Pattison Sand mine. Particularly, this researcher evaluated three hypotheses that could explain the occurrence of pinch out failure. These hypotheses are: (1) roof rock properties, (2) the geometry of the mine opening is a contributory factor to pinch out failures, and (3) pinch out failure is due to lower uniaxial compressive strength associated with coarse-grained St. Peter Sandstone samples.

This study hypothesized that the immediate roof property is a contributory factor to pinch out failures. Consequently, this researcher developed two separate squared shape pillar models with a width to height ratio of one, extraction ratio of 68% and independently varied the immediate roof rock properties (same properties as the pillar or different properties from pillar). The researcher concluded that contrast in the stiffness of the pillar-roof interface is a significant cause of pinch of failures. Particularly, the researcher found that pinch out failure is bound to be more pronounced when the roof rock is cemented St. Peter Sandstone.

This researcher used numerical models to test the hypothesis that the shape of the mine opening is a contributory factor to pinch out failures. This researcher developed a

square and arched shape pillar geometries, with the same width to height ratio and extraction ratio. In the modeling process, the researcher used different constitutive models (elastic and strain softening Mohr-Coulomb) for the roof rock. The researcher observed relatively high stress concentrations at the pillar top, for the squared pillar compared to the arched shaped pillar. High stress concentrations along the sharp corners of square or rectangular pillars are more likely to cause rock fracturing, premature failures or pinch out failures (Hustrulid, 2001). This suggests that pinch out failure is influenced by the shape of the mine opening.

Finally, the researcher used particle-size analysis to explore the hypothesis that pinch out failure is due to the lower uniaxial compressive strength associated with coarse-grained St. Peter Sandstone samples. This was motivated by the fact that coarse-grained St. Peter Sandstone samples have been found to have a relatively lower uniaxial compressive strength than finer-grained samples. The study found that the higher the uniformity coefficient, the higher the uniaxial compressive strength and vice versa. The study found that the uniformity coefficient for the sole pinch out failure location was the lowest compared of all the samples. The researcher concluded that pinch out failure may be due to lower uniaxial compressive strength associated with coarse-grained St. Peter Sandstone samples. Further research is necessary to fully explore this hypothesis as a possible explanation of pinch out failure.

6. SUMMARY, CONCLUSIONS, AND RECOMMENDATIONS

This Section presents the summary, conclusions, and contributions of this research as well as recommendations for future work.

6.1. SUMMARY OF RESEARCH

The goal of this research was to provide our understanding of the factors affecting pillar strength and a provide means to design safe and economic pillars in St. Peter Sandstone. Pursuant to the overall goal of this study, the primary objectives of this research were to:

1. Elucidate factors contributing to ground control problems in St. Peter Sandstone mines;
2. Derive a pillar design method for St. Peter Sandstone using numerical modeling; and
3. Investigate the mechanics of "pinch out" failure in St. Peter Sandstone.

To achieve objective 1, the researcher conducted an extensive literature review to establish factors that contribute to ground control problems in mines. This research used laboratory testing and investigation to determine the physical and mechanical properties of St. Peter Sandstone, Shale, and limestone. The researcher performed field instrumentation and monitoring to measure the stress and deformation characteristics of the pillar and roof rock materials. Moreover, the work used field investigations to: (i) evaluate the condition of pillars in room and pillar St. Peter Sandstone mines; and (ii) document typical ground control practices and challenges in St. Peter Sandstone mines.

To accomplish objective 2, this research developed three-dimensional (3D) finite difference numerical models of mine pillars. The researcher calibrated and validated the numerical models with field stress change measurements obtained through field instrumentation and monitoring exercise. The study used the calibrated and validated numerical model to estimate pillar strength for St. Peter Sandstone. The researcher used the simulation results to propose a pillar strength equation for St. Peter Sandstone. The study performed sensitivity analysis to reveal factors that affect pillar strength.

To accomplish the third objective, the research investigated possible causes of pinch out failure in St. Peter Sandstone. Specifically, the research explored three possible hypotheses that could explain the occurrence of pinch out failure. These hypotheses are:

(1) contrast in roof rock properties influenced pinch out failure, (2) the geometry of the mine opening is a contributing factor to pinch out failures, and (3) pinch out failure occurs because of the lower uniaxial compressive strength associated with coarse-grained St. Peter Sandstone samples.

6.2. CONCLUSIONS

From the work to elucidate factors contributing to ground control problems in St. Peter Sandstone mines, the following conclusions can be drawn:

1. Stress change monitoring indicate that the studied pillars are stable as indicated by the low stress changes recorded by the biaxial stressmeters. The stress change monitoring at 4BQ/BP recorded a maximum principal stress change of 0.23 MPa and a minimum principal stress change of 0.31 MPa. Similarly, stress change monitoring at 10BY/BZ recorded a maximum principal stress change of 0.10 MPa and 0.14 MPa for biaxial stress meters installed 4.57 and 7.92 meters into the pillar. The corresponding minimum principal stress changes are 0.14 MPa and 0.07 MPa for biaxial stress meters installed 4.57 and 7.92 meters into the pillar. Overall, the maximum and minimum principal stress change increased with time as the excavation continued.
2. Roof displacement monitoring suggests that the mine roof at Pattison Sand mine is stable and, perhaps, observed roof instability (e.g. pinch out failures) was a local phenomenon. The maximum observed roof displacement was 0.96 mm and 1.38 mm, respectively, for 4BO/BP and 10BY/BZ. In general, the maximum roof displacement occurred at the mid-length of the roof. The roof displacement results at 4BO/BP indicate a zone of tension (about 1.524 m from the pillar rib) and compression (between 1.524 to 7.3152 m of the roof length). However, the displacement results show that the entire roof at 10BY/BZ is under compression. The fact that roof displacement profiles obtained at 4BO/BP confirmed qualitatively to theoretical predictions, offers credibility both to the classical beam theory (Timoshenko, 1940; Sochor, 2001) and the displacement measurements.

3. Blasting influenced roof displacement at 4BO/BP site.The results from the roof displacement monitoring study revealed that there is a significant difference between the displacement values recorded prior to and after blasting.
4. There is a significant difference between the displacement profiles prior to and after blasting at 10BY/BZ site. However, there is no significant difference between the daily displacement profiles prior to and after blasting at the 4BO/BP site.
5. The pillar designs (dimensions and roof spans) at the CGB mine are adequate to support the overburden stresses incident on them. The ages of pillars at CGB mine range from 35 to 72 years.
6. Rock reinforcement techniques, pinch out failures, and roof failures are some of the major challenges facing St. Peter Sandstone mines. The study found that pinch out failures occurred in small and large size pillars irrespective of the overburden condition. This study recommends bolting, wire meshing and applying shotcrete to pinch out failures areas. This approach was observed to be very effective in dealing with pinch out failures at Pattison Sand mine.
7. A major ground control problem facing St. Peter Sandstone mines are roof instabilities associated with roof falls. Roof instabilities did not occur in every part of the Pattison Sand mine. Moreover, this research study revealed that roof instabilities were predominant where the immediate roof rock was uncemented St. Peter Sandstone, wet cemented St. Peter Sandstone, and/or wet thinly bedded shale following the cemented St. Peter Sandstone or limestone. The study found that massive roof falls were associated with a wet or moist roof. These wet or moist roof delaminated from the immediate neighboring roof layers, induced swelling, and reduced strength at the roof layer interfaces, consequently, these massive roof falls. The study found that these massive roof falls occurred because of inadequate roof supports. The use of long rock bolts has proved effective in solving these roof instability problem associated with water on mine roof (Bajpayee et al., 2014; Molinda and Mark, 2010).

On objective 2, this study draws the following conclusions:

1. This study proposed a numercial simulation procedure that can estimate stress changes in a pillar during mine developments. The researcher used this numerical simulation procedure to predict a stress change of 0.23 MPa, which satisfactorily compared with with measured stress change of 0.25 MPa.
2. Pillar strength is affected by size effect, shape effect, plastic strain rates, friction angle, cohesion and consitutive behavior of the pillar rock.
3. Pillar strength predicted by numerical model using the Mohr Coulomb constitutive law, compared to that predicted by the Mohr Coulomb strain softening consititutive law, was about one and half times for a width to height (w/h) ratio of 1 and up to almost seven times for a w/h ratio of 3. The study concluded that Mohr Coulomb criteria overestimates the pillar strength for St. Peter Sandstone. Consequently, the study proposed that Mohr Coulomb strain softening consititutive laws should be used for realistic modeling of pillar strength for St. Peter Sandstone.
4. The pillar strength equation for St Peter Sandstone is given by:

$$S_p = 14.360 + 11.720C - 0.903h\left[0.28 + 0.53(w/h)\right] \quad (67)$$

Where, C is the cohesion of the pillar rock in MPa, h is the pillar height in meters and w/h is the pillar width to height ratio.

5. The study proposed a safety factor of 2 for designing St. Peter Sandstone pillars. An attempt has been made to relate the pillar widths, heights and overburden depths to safety factor and extraction ratio. Based on this study, it is possible for any St. Peter Sandstone mine such as Pattison Sand mine to adopt room and pillar dimensions that provide maximum extraction ratio and safe working conditions.

On objective 3, this study explored possible causes of pinch out failure in room and pillar mines as observed at the Pattison Sand mine using three hypotheses. These hypotheses are: (1) contrast in roof rock properties influenced pinch out, (2) The geometry of the mine opening is a contributory factor to pinch out failures, and (3) pinch

out failure is due to lower uniaxial compressive strength associated with coarse-grained St. Peter Sandstone samples. The following conclusions can be drawn from this study.

1. This study has demonstrated that pinch out failure is not as a result of higher overburden stress as MSHA hypothesized and used as a basis to shut down Pattison Sand mine in 2010.
2. Pinch out failure occurs as a result of contrast in the elastic moduli in at the pillar-roof interface. Particularly, the study found that pinch out failure was more pronounced when the roof rock was cemented St. Peter Sandstone. Thus, the study concluded that contrast in the immediate roof and pillar rock properties can influence pinch out failures.
3. The fact that measured pillar heights and the thicknesses of thickness of the underground excavations varied from place to place suggested that the intersection of the uncemented and cemented St. Peter Sandstone will not be at the same elevations for all pillars. This finding reveals the reason why pinch out failure is not bound to occur in every part of Pattison Sand mine.
4. The study found relatively high stress concentration at the pillar top, for the squared pillar shape compared with the arched shape pillar shape. High stress concentrations along the sharp corners of square or rectangular pillars are more likely to cause rock fracturing or premature failures (Hustrulid, 2001). This finding suggests that pinch out failure is influenced by the shape of the mine opening.
5. The study found that the higher the uniformity coefficient, the higher the uniaxial compressive strength and the finer the particle sizes for St. Peter Sandstone soil samples and vice versa.
6. The researcher found that the uniformity coefficient for a pinch out location was the lowest compared to 6AR and 1S samples. This suggests that the particle size at the pinch out failure location is the coarsest compared to 6AR and 1S samples. The researcher concluded that pinch out failure occurs because of the lower uniaxial compressive strength associated with coarse-grained St. Peter Sandstone samples. This research revealed that the uniformity coefficients at the pillar top

were not necessarily low; suggesting that pinch out failure is not only bound to occur at the pillar-roof interface.

6.3. CONTRIBUTIONS OF PHD RESEARCH

The following are the key contributions of this PhD study, which is a maiden attempt to develop a rigorous, scientific and engineering solutions to the pillar design problem for St. Peter Sandstone.

1. This is the first time extensive field investigation together with field instrumentation and monitoring has been undertaken to demonstrate that St. Peter Sandstone pillars are stable.
2. This research study has proposed a criteria for pillar design in St. Peter Sandstone room and pillar mines. Prior to this work, there was no basis for pillar design in St. Peter Sandstone mines.
3. The pillar design method developed in this research may be useful for underground mining of similar geomaterials (e.g. Jordan Sandstone, Oil Creek Sandstone, Hickory Sandstone, Swam River Sandstone, and Athabasca Oil Sands) that have low cohesion and high friction angles. This study should encourage further research to evaluate whether the proposed method is indeed applicable to these geomaterials.
4. This study presents the first attempt towards methodologically calibrated numerical models with field stress change measurements. The proposed numerical calibration procedure will be useful to pillar design modelers.
5. This research should transform engineering practice in St. Peter Sandstone room and pillar mines. The pillar design criteria proposed by this research is expected to assist engineers for effective mine planning and design while improving the productivity of personnel and equipment at St. Peter Sandstone room and pillar mines. Other recommendations regarding ground control techniques and causes of pinch out failures should also help mine managers and engineers provide a safer working environment for room and pillar mines in St. Peter Sandstone.

6.4. RECOMMENDATIONS FOR FUTURE WORK

The following recommendations can be outlined:

1. Site engineers took the readings from the readout box manually. These readings were taken about 3 hours from the time of blasting. It is possible that these engineers missed meaningful displacement data especially in the first hour after each blast. For this reason, the results of the effect of blasting on roof displacement may be limited. This study recommends the use of automatic data acquisition systems (such as data loggers) for field monitoring to further evaluate the effect of blasting on displacements in St. Peter Sandstone.
2. Numerical modeling studies used in this study assumed that the rock layers are homogenous and isotropic. However, Bagherieh (2015) found that the strength characteristics of St. Peter Sandstone is heterogenous. Consequently, for robust and realistic characterization of the strength mechanics of St. Peter Sandstone, the reseracher recommends stochastic and anisotropic numerical modeling of pillar strength and pillar stress distributions.
3. This study observed that maximum measured roof displacements occurred at the center of the roof in some locations, and not in others. Also, the study observed that the state of displacement was entirely under tension. While this finding was consistent with classical beam theory predictions, the study also found that the state of roof displacement was also under compression in some other locations. This roof behaviour should be the subject of future research.
4. Future studies are required to investigate whether the classical beam theory can be used to explain pinch out failures at St. Peter Sandstone mines.
5. This study should encourage further research to evaluate whether the proposed method is indeed applicable to similar geomaterials such as Jordan Sandstone, Oil Creek Sandstone, Hickory Sandstone, Swam River Sandstone, and Athabasca Oil Sands

APPENDIX

Appendices A-K can be found in the supplemental information files. Appendices included are as follows:

Appendix A. STRESS CHANGE MONITORING AT PATTISON SAND MINE.

Appendix B. DISPLACEMENT MONITORING AT PATTISON SAND MINE

Appendix C. ROOM AND PILLAR DIMENSIONS AT CGB MINE

Appendix D. CONDITIONS OF ROOM AND PILLAR CASES AT CGB MINE

Appendix E. PINCH OUT FAILURE AT PATTISON SAND MINE

Appendix F. PILLAR REINFORCEMENT RECOMMENDED BY MSHA

Appendix G. VARIOUS ROOF CONDITIONS AND REINFORCEMENT TECHNIQUES AT ST. PETER SANDSTONE MINES

Appendix H. INFLUENCE OF PILLAR WIDTH, PILLAR HEIGHT, OVERBURDEN DEPTH ON SAFETY FACTOR AND EXTRACTION RATIO

Appendix I. DIFFERENTIAL STRESS DISTRIBUTIONS AT PILLAR TOP, MIDHEIGHT AND BOTTOM FOR A SQUARE PILLAR USING EMCS AND SSMCUS ROOF MODELS

Appendix J. DIFFERENTIAL STRESS DISTRIBUTIONS AT PILLAR TOP, MIDHEIGHT AND BOTTOM FOR ARCHED SHAPED PILLAR

Appendix K. COMPARISON OF DIFFERENTIAL STRESS DISTRIBUTIONS AT PILLAR TOP, MIDHEIGHT AND BOTTOM FOR ARCHED AND SQUARE SHAPED PILLARS

BIBLIOGRAPHY

Abbasi, B., Russell, D., & Taghavi, R. (2013). FLAC 3D mesh and zone quality.

Abdelaziz, T. S., Martin, C. D., & Chalaturnyk, R. J. (2008). Characterization of locked sand from Northeastern Alberta.

Allen, J. R. (1965). A review of the origin and characteristics of recent alluvial sediments. *Sedimentology, 5*(2), 89-191.

Alostaz, M. d., Biggar, K., Donahue, R., & Hall, G. (2008). Soil type effects on petroleum contamination characterization using ultraviolet induced fluorescence excitation-emission matrices (EEMs) and parallel factor analysis (PARAFAC). *Journal of Environmental Engineering and Science, 7*(6), 661-675.

Amadei, B., & Stephansson, O. (1997). *Rock stress and its measurement*: Springer Science & Business Media.

Amaral, E., & Pryor, W. (1977). Depositional environment of the St. Peter sandstone deduced by textural analysis. *Journal of Sedimentary Research, 47*(1).

Arthur, F., Hyder, Z., Tiile, R., & Ge, M. C. (2016). *Pillar Stability Analysis at Missouri S&T Dolomitic Limestone Experimental Mine.* Paper presented at the 50th US Rock Mechanics/Geomechanics Symposium.

Bagherieh, A. (2015). *Microstructure and geotechnical properties of St. Peter Sandstone.* (Unpublished Doctoral Dissertation), Missouri University of Science and Technology, Rolla, Missouri,USA.

Ballivy, G., & Dayre, M. (1984). The mechanical behaviour of aggregates related to physicomechanical properties of rocks. *Int Assoc Eng Geol Bull, 29*, 339-342.

Barrell, J. (1914). The strength of the Earth's crust. *The Journal of Geology, 22*(7), 655-683.

Barton, M., Palmer, S., & Wong, Y. (1986). A geotechnical investigation of two Hampshire Tertiary Sand Beds: are they locked sands? *Quarterly Journal of Engineering Geology and Hydrogeology, 19*(4), 399-412.

Beuselinck, L., Govers, G., Poesen, J., Degraer, G., & Froyen, L. (1998). Grain-size analysis by laser diffractometry: comparison with the sieve-pipette method. *Catena, 32*(3), 193-208.

Bevan, A. C. (1926). The Glenwood beds as a horizon marker at the base of the Platteville formation. *Report of investigations no. 009*.

Bieniawski, Z. (1968). *The effect of specimen size on compressive strength of coal.* Paper presented at the International Journal of Rock Mechanics and Mining Sciences & Geomechanics Abstracts.

Blejwas, T. E. (1987). *Planning a program in experimental rock mechanics for the Nevada Nuclear Waste Storage Investigations Project.* Paper presented at the The 28th US Symposium on Rock Mechanics (USRMS).

Bolton, M. (1986). The strength and dilatancy of sands. *Geotechnique, 36*(1), 65-78.

Brady, B., & Brown, E. (1985). 2004 "Rock Mechanics for Underground Mining" George Allen & Unwin–London.

Brattli, B. (1992). The influence of geological factors on the mechanical properties of basic igneous rocks used as road surface aggregates. *Engineering Geology, 33*(1), 31-44.

Brown, E. T. (1981). Rock characterization, testing & monitoring: ISRM suggested methods.

Catacosinos, P., Harrison III, W., Reynolds, R., Westjohn, D., & Wollensack, M. (2001). Stratigraphic lexicon for Michigan: Michigan Geological Survey Bulletin, v. 8. *Department of Environmental Quality and Michigan Basin Geological Society, 56*.

Caudle, R. D., & Clark, G. B. (1955). Stresses around mine openings in some simple geologic structures: University of Illinois at Urbana Champaign, College of Engineering. Engineering Experiment Station.

Celauro, C., Ziccarelli, M., Parla, G., & Valore, C. (2014). An automated procedure for computing the packing properties of dense and locked sands by image analysis of thin sections. *Granular Matter, 16*(6), 867-880.

Cole, V. B. (1975). Subsurface Ordovician-Cambrian Rocks in Kansas. *Reprinted 1981ed.) Lawrence, Kansas: Kansas Geological Survey, 2*.

Cresswell, A., & Barton, M. (2003). Direct shear tests on an uncemented, and a very slightly cemented, locked sand. *Quarterly Journal of Engineering Geology and Hydrogeology, 36*(2), 119-132.

Cresswell, A., & Powrie, W. (2004). Triaxial tests on an unbonded locked sand. *Geotechnique, 54*(2), 107-115.

Dake, C. L. (1921). *The problem of the St. Peter sandstone* (Vol. 6): Columbia University.

Dapples, E. C. (1955). General lithofacies relationship of St. Peter Sandstone and Simpson Group. *AAPG Bulletin, 39*(4), 444-467.

Davis, J. (2011). Generalized isochore map of St. Peter Sandstone mineral resource in Missouri, Map: Rolla, Missouri, Missouri Department of Natural Resources, Division of Geology and Land Survey. *Industrial Minerals Unit, scale, 1*(2,560,000).

Dittes, M., & Labuz, J. (2002). Field and laboratory testing of St. Peter sandstone. *Journal of geotechnical and geoenvironmental engineering, 128*(5), 372-380.

Dittes, M. E. (2015). *Mechanical properties of St. Peter sandstone a comparison of field and laboratory results.* University of Minnesota.

Dunnicliff, J. (1993). *Geotechnical instrumentation for monitoring field performance*: John Wiley & Sons.

Dusseault, M. (1977). *The geotechnical characteristics of the Athabasca oil sands; unpublished Ph. D.* thesis. University of Alberta, Edmonton.

Dusseault, M., & Morgenstern, N. (1979). Locked sands. *Quarterly Journal of Engineering Geology and Hydrogeology, 12*(2), 117-131.

Dutta, P. (1985). *Some recent developments in vibrating wire rock mechanics instrumentation.* Paper presented at the Proceedings of the 26th US symposium rock mechanics, Rapid City, SD. Rotterdam: Balkema.

Dutta, P., & Hatfield, R. (1987). *Calibration measurements of rock stress by vibrating wire stressmeter at high temperatures.* Paper presented at the Proc. 2nd Int. Symp. on Field Measurements in Geomechanics.

Dutta, P. K., Hatfield, R. W., & Runstadler Jr, P. (1981). Calibration characteristics of IRAD GAGE vibrating wire stressmeter at normal and high temperature. Volume 2: Creare Products, Inc., Lebanon, NH (United States).

Elder, S. (1936). The contact between the Glenwood and Platteville formations: Illinois Academy of Science Transactions, v. 29.

Erdoğan, S., Forster, A. M., Stutzman, P. E., & Garboczi, E. (2017). Particle-based characterization of Ottawa sand: Shape, size, mineralogy, and elastic moduli. *Cement and Concrete Composites, 83*, 36-44.

Esterhuizen, G. (2007). Evaluation of the strength of slender pillars. *Transactions-society for mining metallurgy and exploration incorporated, 320*, 69.

Esterhuizen, G., Dolinar, D., & Ellenberger, J. (2011). Pillar strength in underground stone mines in the United States. *International Journal of Rock Mechanics and Mining Sciences, 48*(1), 42-50.

Fahrman, B. P. (2016). Numerical Modeling of Room-and-Pillar Coal Mine Ground Response.

Fiore, J., Der, V. and Montenyohl, V. (1984). *An Overview of the OCRM program efforts.* Paper presented at the US Symposium Rock Mechanics Evanston.

Folk, R. (1968). *Bimodal supermature sandstones: product of the desert floor.* Paper presented at the Proceedings of the 23rd International Geological Congress.

Fossum, A., Russell, J., & Hansen, F. (1977). Analysis of vibrating-wire stress gage in soft rock. *Experimental Mechanics, 17*(7), 261-264.

Fraser, G. S. (1976). Sedimentology of a Middle Ordovician quartz arenite–carbonate transition in the Upper Mississippi Valley. *GSA Bulletin, 87*(6), 833-845.

Giles, A. W., & Bonewits, E. E. (1930). *St. Peter and older Ordovician sandstones of northern Arkansas* (Vol. 4).

Glick, E. E., & Frezon, S. E. (1953). Lithologic character of the St. Peter sandstone and the Everton formation in the Buffalo River valley, Newton County, Arkansas: US Geological Survey.

Goldring, R. (1966). Sandstones of sublittoral (neritic) facies. *Nature, 210*, 1248-1249.

Goldring, R., & Bridges, P. (1973). Sublittoral sheet sandstones. *Journal of Sedimentary Research, 43*(3).

Gregory, C., Cramer, M., Ames, R., & McHenry, J. (1983). *Applicability Of Borehole Stress Meaurement Instrumentation To Closely Jointed Rock.* Paper presented at the The 24th US Symposium on Rock Mechanics (USRMS).

Gregory, E. C., & Kim, K. (1981). *Preliminary results from the full-scale heater tests at the near-surface test facility.* Paper presented at the The 22nd US Symposium on Rock Mechanics (USRMS).

Haimson, B. (1978). *The hydrofracturing stress measuring method and recent field results.* Paper presented at the International Journal of Rock Mechanics and Mining Sciences & Geomechanics Abstracts.

Harrison, R. W. (1997). *Bedrock geologic map of the St. Louis 30'x 60'Quadrangle, Missouri and Illinois*.

Hawkes, I., & Hooker, V. (1976). *The vibrating wire stressmeter: 6F, 3R. Proc. 3rd Congress ISRM, Denver. 1974, vol 2 part A, P439–444.* Paper presented at the International Journal of Rock Mechanics and Mining Sciences & Geomechanics Abstracts.

Hawkins, A. (1998). Aspects of rock strength. *Bulletin of engineering geology and the environment, 57*(1), 17-30.

Hedley, D., & Grant, F. (1972). Stope-and-pillar design for Elliot Lake Uranium Mines. *Canadian Mining and Metallurgical Bulletin, 65*(723), 37-&.

Heuze, F., Patrick, W., De la Cruz, R., & Voss, C. (1981). In situ geomechanics: Climax granite, Nevada Test Site: Lawrence Livermore National Lab., CA (United States).

Heuze, F. E. (1981). *Geomechanics Of The Climax" Mine-By" Nevada Test Site.* Paper presented at the The 22nd US Symposium on Rock Mechanics (USRMS).

Hoek, E., & Brown, E. (1980). Underground Exavations in Rock: Institution of Mining and Metallurgy, London, 527 p. *Google Scholar*.

Hoek, E., Grabinsky, M., & Diederichs, M. (1991). Numerical modelling for underground excavation design. *Institution of Mining and Metallurgy Transactions. Section A. Mining Industry, 100*.

Holland, C. T., & Gaddy, F. L. (1956). Some aspects of permanent support of overburden on coal beds. *Proceedings of West Virginia Coal Mining Institute*, 43-65.

Holtz, R. D., & Kovacs, W. D. (1981). *An introduction to geotechnical engineering*.

Hosseini, B. K. (2015). *Use of Streamline Simulation in Large Scale Reservoir-geomechanical Modeling of Reservoirs.* University of Alberta.

Hunsche, U. E. (1992). True triaxial failure tests on cubic rock salt samples. experimental methods and results *Finite Inelastic Deformations—Theory and Applications* (pp. 525-536): Springer.

Hustrulid, W. (1976). A review of coal pillar strength formulas. *Rock Mechanics, 8*(2), 115-145.

Hustrulid, W. A., Hustrulid, W. A., & Bullock, R. C. (2001). *Underground mining methods: Engineering fundamentals and international case studies*: SME.

Hustrulid, W. A., & McClain, W. C. (1984). *Policy Questions Related To The Role Of Field Testing In The Establishment Of A Radioactive Waste Repository.* Paper presented at the The 25th US Symposium on Rock Mechanics (USRMS).

Iannacchione, A., Esterhuizen, G., Bajpayee, T., Swanson, P., & Chapman, M. (2005). *Characteristics of mining-induced seismicity associated with roof falls and roof caving events.* Paper presented at the Alaska Rocks 2005, The 40th US Symposium on Rock Mechanics (USRMS).

Ishida, T., Labuz, J. F., Manthei, G., Meredith, P., H. B. Nasseri, M., Shin, K., . . . Zang, A. (2017). *ISRM Suggested Method for Laboratory Acoustic Emission Monitoring* (Vol. 50).

Itasca, F. D. (2008). Fast Lagrangian Analysis of Continua in 3 Dimensions, Version 4.0. *Minneapolis, Minnesota, Itasca Consulting Group, 438*.

Jahns, H. (1966). *Measuring the strength of rock in situ at an increasing scale.* Paper presented at the 1st ISRM Congress.

Jaiswal, A., & Shrivastva, B. (2009). Numerical simulation of coal pillar strength. *International Journal of Rock Mechanics and Mining Sciences, 46*(4), 779-788.

Jaworski, G., Dorwart, B., White, W., & Beloff, W. (1982). *Behavior of a rigid inclusion stressmeter in an anisotropic stress field.* Paper presented at the The 23rd US Symposium on Rock Mechanics (USRMS).

Jeremic, M. (1985). *Strata mechanics in coal mining*: CRC Press.

John, M. (1972). The influence of length to diameter ratio on rock properties in uniaxial compression: a contribution to standardisation in rock mechanics testing. *Rep S Afr CSIR No ME1083/5*.

Jones, R. (2009). The middle-upper Ordovician Simpson Group of the Permian Basin—Deposition, diagenesis, and reservoir development. *Integrated synthesis of the Permian Basin—Data and models for recovering existing and undiscovered oil resources from the largest oil-bearing basin in the US: Texas Bureau of Economic Geology, Final Technical Report, DOE Award DE-FC26-04NT15509*, 107-147.

Kaiser, P., & Maloney, S. (1992). *The role of stress change in underground construction.* Paper presented at the Rock Characterization: ISRM Symposium, Eurock'92, Chester, UK, 14–17 September 1992.

Klaber, M., & Munro, D. (1978). Alopecia areata: immunofluorescence and other studies. *British Journal of Dermatology, 99*(4), 383-386.

Knupp, P. (2007). Remarks on mesh quality, in '45th AIAA Aerospace Sciences Meeting and Exhibit'. *Sandia National Laboratories, New Mexico, USA*.

Krauland, N., & Soder, P. (1987). DETERMINING PILLAR STRENGTH-FROM PILLAR FAILURE OBSERVATION. *E&MJ-Engineering and Mining Journal, 188*(8), 34-40.

Krinsley, D., & Doornkamp, J. C. (1973). Atlas of Sand Grain Surface Textures: Cambridge, UK, Cambridge University Press.

Lamar, J. E. (1928). Geology and economic resources of the St. Peter Sandstone of Illinois. *Bulletin no. 053*.

Leatherock, C. (1945). The correlation of rocks of Simpson age in north-central Kansas with the St. Peter sandstone and associated rocks in northwestern Missouri. *Kansas Geol. Survey Bull, 60*, 1-16.

Lee, F. T., Abel Jr, J. F., & Nichols Jr, T. C. (1976). The relation of geology to stress changes caused by underground excavation in crystalline rocks at Idaho Springs, Colorado: US Govt. Print. Off.

Lemcoe, M., Pratt, H., & Grams, W. (1980). *State-Of-The-Art Review, Of Rock Mechanics Techniques For Measurement Of Stress, Displacement And Strain.* Paper presented at the ISRM International Symposium-Rockstore 80.

Leonard, A. (1906). Geology of Clayton County. *Iowa Geological Survey Annual Report, 16*(1), 213-318.

Lingle, R., Davidson, A., & Clayton, R. (1981). Summary report on the development of stress and deformation measurement techniques: Terra Tek, Inc., Salt Lake City, UT (USA).

Lingle, R., & Nelson, P. H. (1982). *In situ measurements of stress change induced by thermal load: a case history in granitic rock.* Paper presented at the The 23rd US Symposium on Rock Mechanics (USRMS).

Lounsbery, R., & West, T. (1965). Petrography of some Indiana aggregates in relation to their engineering properties. *Univ Kentucky Eng Exp Station Bull Ser, 20*(2), 24-41.

Lunder, P., & Pakalnis, R. (1997). Determination of the strength of hard-rock mine pillars. *CIM bulletin, 90*(1013), 51-55.

Mai, H., & Dott, R. H. (1985). *A subsurface study of the St. Peter Sandstone in southern and eastern Wisconsin*: Wisconsin Geological & Natural History Survey.

Maleki, H. (1990). *Development of modeling procedures for coal mine stability evaluation.* Paper presented at the Rock Mechanics Contributions and Challenges: Proceedings of the 31st US Symposium. Balkema.

Manger, G. E. (1963). Porosity and bulk density of sedimentary rocks.

Mao, N.-H. (1986). *A new approach for calibration and interpretation of IRAD GAGE vibrating-wire stressmeters.* Paper presented at the ISRM International Symposium.

Mark, C. (1987). Analysis of longwall pillar stability: Pennsylvania State Univ., University Park (USA).

Mark, C. (1987). Analysis of longwall pillar stability [Dissertation]. *University Park, PA: The Pennsylvania State University, Department of Mining Engineering*.

Mark, C. (1999). *Empirical methods for coal pillar design.* Paper presented at the Proceedings of the 2nd international on workshop coal pillar mechanics and design, National Institute for Occupational Safety and Health, Report IC.

Marti, J., & Cundall, P. (1982). Mixed discretization procedure for accurate modelling of plastic collapse. *International Journal for Numerical and Analytical Methods in Geomechanics, 6*(1), 129-139.

Martin, C., & Maybee, W. (2000). The strength of hard-rock pillars. *International Journal of Rock Mechanics and Mining Sciences, 37*(8), 1239-1246.

Martin, C., & Simmons, G. (1993). The atomic energy of Canada limited underground research laboratory: an overview of geomechanics characterization. *Comprehensive rock engineering, 5*, 915-950.

Mavis, F. T., & Wilsey, E. F. (1936). A study of the permeability of sand.

Mazzullo, J. M., & Ehrlich, R. (1983). Grain-shape variation in the St. Peter sandstone: a record of eolian and fluvial sedimentation of an early Paleozoic cratonic sheet sand. *Journal of Sedimentary Research, 53*(1).

McKEE, E. D. (1966). Structures of dunes at White Sands National Monument, New Mexico (and a comparison with structures of dunes from other selected areas). *Sedimentology, 7*(1), 3-69.

Minaeian, V. (2014). *True triaxial testing of sandstones and shales.* Curtin University.

Mishra, D. A., & Janeček, I. (2017). Laboratory triaxial testing–From historical outlooks to technical aspects. *Procedia engineering, 191*, 342-351.

Mohan, G. M., Sheorey, P., & Kushwaha, A. (2001). Numerical estimation of pillar strength in coal mines. *International Journal of Rock Mechanics and Mining Sciences, 38*(8), 1185-1192.

Molinda, G., & Mark, C. (2010). Ground failures in coal mines with weak roof. *Electron J Geotech Eng, 15*(F), 547-588.

Mortazavi, A., Hassani, F., & Shabani, M. (2009). A numerical investigation of rock pillar failure mechanism in underground openings. *Computers and Geotechnics, 36*(5), 691-697.

Mossler, J. H. (2008). RI-65 Paleozoic Stratigraphic Nomenclature for Minnesota.

Mudrey, M. (1987). *Bedrock Geology of Wisconsin: Northwest Sheet*: University of Wisconsin-Extension, Geological and Natural History Survey.

Noorany, I., & Seed, H. B. (1965). In-situ strength characteristics of soft clays. *Journal of Soil Mechanics & Foundations Div, 91*(Proc. Paper 4274).

Obert, L., & Duvall, W. I. (1967). Rock mechanics and the design of structures in rock.

Obert, L., Windes, S. L., & Duvall, W. I. (1946). Standardized tests for determining the physical properties of mine rock. *REPORT OF INVESTIGATIONS 3891, 1946. 51 P, 25 TAB.*

Onodera, T., & Asoka Kumara, H. (1980). Relation between texture and mechanical properties of crystalline rocks. *Bull Int Assoc Eng Geol, 22*, 173-177.

Owen, D. (1847). Preliminary report of the geological survey of Wisconsin and Iowa: US General Land Office Rept.

Ozbay, U., Rozgonyi, T. G., & FIEAust, C. (2003). *Numerical modeling of stress and deformations encountered in deep longwall coal mines usig strain softening failure criterion.* Paper presented at the International Conference on Safety and Environmental Aspects of Mining. University of Miskolc Series A. Mining.

Palais, R. S., & Palais, R. A. (2009). *Differential equations, mechanics, and computation* (Vol. 51): American Mathematical Soc.

Pariseau, W. G. (1985). Linearization of in situ stress change formulae for gauges at arbitrary down-hole orientation. *International Journal for Numerical and Analytical Methods in Geomechanics, 9*(3), 277-283.

Patrick, W., & Rector, N. (1983). Reliability of instrumentation in a simulated nuclear-waste repository environment: Lawrence Livermore National Lab., CA (United States).

Payne, C. M. (1967). Engineering aspects of the St. Peter sandstone in the Minneapolis-St. Paul area of Minnesota.

Petersen, D. L. (1978). *Estimating the strength of St. Peter sandstone pillars.* University of Minnesota.

Pittman, E. D. (1972). Diagenesis of quartz in sandstones as revealed by scanning electron microscopy. *Journal of Sedimentary Research, 42*(3).

Potter, P. E. (1967). Sand bodies and sedimentary environments: a review. *AAPG Bulletin, 51*(3), 337-365.

Potvin, Y., Hudyma, M., & Miller, H. (1988). *Design guidelines for open stope support.* Paper presented at the CIM bulletin.

Pratt, H., Black, A., Brown, W., & Brace, W. (1972). *The effect of speciment size on the mechanical properties of unjointed diorite.* Paper presented at the International Journal of Rock Mechanics and Mining Sciences & Geomechanics Abstracts.

Pritchard, C., & Hedley, D. (1993). *Progressive pillar failure and rockbursting at Denison Mine.* Paper presented at the Proceedings of 3rd International Symposium on Rockbursts and Seismicity in Mines, Kingston. Rotterdam: AA Balkema.

Prowse, D. (1983). *Some physical properties of bitumen and oil sand*: Alberta Research Council.

Read, R., & Martin, C. (1992). *Monitoring the excavation-induced response of granite.* Paper presented at the The 33th US Symposium on Rock Mechanics (USRMS).

Richards, N., & Barton, M. (1999). The Folkestone Bed sands: microfabric and strength. *Quarterly Journal of Engineering Geology and Hydrogeology, 32*(1), 21-44.

Roberts, D., Van der Merwe, J., Canbulat, I., Sellers, E., & Coetzer, S. (2002). Development of a method to estimate coal pillar loading.

Ryaben'kii, V. S., & Tsynkov, S. V. (2006). *A theoretical introduction to numerical analysis*: CRC Press.

Salamon, M. (1970). *Stability, instability and design of pillar workings.* Paper presented at the International journal of rock mechanics and mining sciences & geomechanics abstracts.

Salamon, M., & Munro, A. (1967). A study of the strength of coal pillars. *Journal of the South African Institute of Mining and Metallurgy, 68*(2), 55-67.

Schrauf, T. (1980). *Review of Current Capabilities for the Measurement of Stress, Displacement and in Situ Deformation Modulus* (Vol. 95): Battelle Memorial Institute, Office of Nuclear Waste Isolation.

Schwartz, G. (1939). Foundation conditions at the sites of the prnposed St. *Anthony Falls locks Minneaplis, Minnesota. Rep.(o the US, Arrny Corps of Engineers, St, Paul DistIict.*

Sellers, J. (1977). The measurement of stress changes in rock using the vibrating wire stressmeter. *Proceedings of the international field measurements in rock mechanics, Zurich*, 275-288.

Siever, R. (1959). Petrology and geochemistry of silica cementation in some Pennsylvanian sandstones.

Sjoberg, J. (1992). *Failure modes and pillar behaviour in the Zinkgruvan mine.* Paper presented at the The 33th US Symposium on Rock Mechanics (USRMS).

Skempton, A., & Sowa, V. (1963). The behaviour of saturated clays during sampling and testing. *Geotechnique, 13*(4), 269-290.

St John, C. M., & Hardy, M. P. (1982). *Geotechnical monitoring of high-level nuclear waste repository performance.* Paper presented at the The 23rd US Symposium on Rock Mechanics (USRMS).

Suhm, R., & Ethington, R. (1975). Stratigraphy and conodonts of Simpson Group (middle Ordovician), Beach and Baylor mountains, West Texas. *AAPG Bulletin, 59*(7), 1126-1135.

Swett, K., Klein, G. D., & Smit, D. E. (1971). A Cambrian Tidal Sand Body: The Eriboll Sandstone of Northwest Scotland: An Ancient-Recent Analog. *The Journal of Geology, 79*(4), 400-415.

Technology, A. O. S., Authority, R., Hepler, L. G., & Hsi, C. (1989). *AOSTRA technical handbook on oil sands, bitumens and heavy oils*: Alberta Oil Sands Technology and Research Authority.

Teufel, L. W., & Farrell, H. E. (1990). In situ stress and natural fracture distribution in the Ekofisk field, North Sea: Sandia National Labs., Albuquerque, NM (USA).

Thiel, G. A. (1935). Sedimentary and petrographic analysis of the St. Peter sandstone. *GSA Bulletin, 46*(4), 559-614.

Timoshenko, S. (1940). *Strength of materials Part 1*: D. Van Nostrand Co., Inc.

Tunbridge, L., & Oien, K. (1988). *The advantages of vibrating wire instruments in geomechanics.* Paper presented at the 2nd Proc. International Symposium on Field Measurements in Geomechanics.

Tuncay, E., & Hasancebi, N. (2009). The effect of length to diameter ratio of test specimens on the uniaxial compressive strength of rock. *Bulletin of engineering geology and the environment, 68*(4), 491.

Visher, G. S. (1972). Physical characteristics of fluvial deposits.

Visocky, A. P., Sherrill, M. G., & Cartwright, K. (1985). Geology, hydrology, and water quality of the Cambrian and Ordovician systems in northern Illinois: Illinois State Water Survey and the Illinois State Geological Survey.

Von Kimmelmann, M., Hyde, B., & Madgwick, R. (1984). *7 The use of computer applications at BCL Limited in planning pillar extraction and the design of mining layouts.* Paper presented at the Design and Performance of Underground Excavations: ISRM Symposium—Cambridge, UK, 3–6 September 1984.

Wang, H., Jiang, Y., Zhao, Y., Zhu, J., & Liu, S. (2013). Numerical investigation of the dynamic mechanical state of a coal pillar during longwall mining panel extraction. *Rock mechanics and rock engineering, 46*(5), 1211-1221.

Wang, H., Poulsen, B. A., Shen, B., Xue, S., & Jiang, Y. (2011). The influence of roadway backfill on the coal pillar strength by numericalinvestigation. *International Journal of Rock Mechanics and Mining Sciences, 48*(3), 443-450.

Watson, J. D. (1938). 'Triaxial compression tests on St. Peter sandstone. *Rep. to the US Army Corps of Engineers, St. Paul District*.

Whitten, D. W., & Brooks, J. R. V. (1972). The Penguin dictionary of geology.

Wilson, A. (1972). An hypothesis concerning pillar stability. *Min Eng (London), 131*(141), 409-417.

Winfree, K. E. (1983). *Depositional environments of the St. Peter Sandstone of the upper Midwest*: University of Wisconsin--Madison.

Zimmerman, R. (1982). *Issues related to field testing in tuff.* Paper presented at the The 23rd US Symposium on Rock Mechanics (USRMS).

VITA

Francis Anohomah Arthur obtained his Bachelor of Science degree in Mining Engineering from the University of Mines and Technology, Tarkwa, Ghana in 2010. He has worked as an Open Pit Mining Engineer Intern at Golden Star Resources (Bogoso/Prestea) Limited, Ghana. He worked as a Mining Engineer at AngloGold Ashanti Limited (Obuasi Gold Mine) from 2010 to 2011 before pursuing graduate studies at the Missouri University of Science and Technology (Missouri S&T) in Rolla, MO in June 2011. In 2012, Francis worked as Underground Mining Engineer Intern at Pattison Sand Company, LLC, Clayton, Iowa, USA. Since 2011, Francis has been engaged in rock mechanics and ground control research involving extensive field investigations and characterizations, laboratory testing and characterizations, comprehensive three-dimensional geomechanical modeling, and geotechnical field instrumentation and monitoring. He has been a Graduate Teaching Assistant in soil mechanics, rock mechanics, advanced rock mechanics and underground mine design courses at Missouri S&T from 2012 to 2017. Francis holds a Master of Science degree in Geological Engineering and a Master of Engineering degree in Mining Engineering, all from Missouri S&T (2015–2016). He began his graduate studies under the guidance of Dr. Ge, an Associate Professor Emeritus in Mining Engineering. Francis has over 5 years of experience in rock mechanics and ground control in soft and hard rocks, deterministic and stochastic geomechanical modeling, geotechnical instrumentation and monitoring, underground mine planning and design, among others. He received his PhD in Mining Engineering from Missouri S&T in December 2017.